

METHODS AND PROBES OF VORTEX GENERATION AND  
CONTROL IN DILUTE-GAS BOSE-EINSTEIN CONDENSATES

by

Andrew John Schaffer

---

Copyright © Andrew John Schaffer 2021

A Dissertation Submitted to the Faculty of the  
JAMES C. WYANT COLLEGE OF OPTICAL SCIENCES

In Partial Fulfillment of the Requirements  
For the Degree of

DOCTOR OF PHILOSOPHY  
WITH A MAJOR IN OPTICAL SCIENCES


In the Graduate College

THE UNIVERSITY OF ARIZONA

2021

THE UNIVERSITY OF ARIZONA  
GRADUATE COLLEGE

As members of the Dissertation Committee, we certify that we have read the dissertation prepared by **Andrew Schaffer**, titled *Methods and Probes of Vortex Generation and Control in Dilute-Gas Bose-Einstein Condensates* and recommend that it be accepted as fulfilling the dissertation requirement for the Degree of Doctor of Philosophy.

  
\_\_\_\_\_  
Professor Brian P. Anderson

Date: 4/21/2021

  
\_\_\_\_\_  
Professor R. Jason Jones


Date: 4/21/2021

  
\_\_\_\_\_  
Professor Ewan M. Wright

Date: 4/21/2021

Final approval and acceptance of this dissertation is contingent upon the candidate's submission of the final copies of the dissertation to the Graduate College.

I hereby certify that I have read this dissertation prepared under my direction and recommend that it be accepted as fulfilling the dissertation requirement.

  
\_\_\_\_\_  
Professor Brian P. Anderson  
Dissertation Committee Chair  
Wyant College of Optical Sciences

Date: 8/12/2021

ARIZONA

## ACKNOWLEDGEMENTS

I would like to say a special thanks to some of the many people who have impacted my life and supported me on this journey.

First, I would like to thank my advisor, Brian Anderson, for his guidance, patience and support. I will forever be grateful for his commitment to both my academic success and personal wellness. I also want to thank the rest of my dissertation committee, Ewan Wright and Jason Jones, for the many hours of discussion, guidance and feedback they provided me over the years.

I would be amiss to not also acknowledge the members of the various communities that deeply impacted my life over these years. First, I would like to thank my previous labmates Zachary Newman and Jessica Myers for welcoming me into the lab and for all they taught me in my early years of graduate school. I am deeply thankful to Sam Nerenberg for all these years of friendship, support and laughs, especially when grad school was getting the best of us. Thanks to Van Butcher for his company in an otherwise lonely lab. Thank you to David Melchior for all the much-needed breaks, chats, coffee, and cheese. And a final thank you to Kevin Kuper for being a reliable and supportive colleague and roommate.

I am grateful to the donors of the Willis E. Lamb Jr. Endowed Scholarship for their contributions to my PhD journey.

Thanks to my many wonderful friends in the Graduate Christian Fellowship that made my years of grad school some of the best of my life. Thanks to David Somnitz for his years of support and encouragement. Thank you to Colton Bigler, Ben Chrysler, and Ben Cromey for the years of friendship and adventures. Thank you to Nathan Harkema and all the other wallyball, frisbee and Bible study friends that walked with me through the best and worst of times.

Thank you to Pastor Kai and Annette and my CCA family for being a home away from home.

Thank you to my parents, sisters and family who have been with me both in person and in spirit through my entire education. I am especially grateful for my parents, Barry and Julie Schaffer, for teaching me the values of diligence and perseverance and believing in me even when I didn't. Thank you to my wonderful girlfriend, Carissa Raymond, for her support throughout my education and for joining me in Minnesota on the next step of our journey together. Whether playing disc golf on breaks or working together remotely, her company made finishing a dissertation during a pandemic not so bad.

Finally, I am thankful to my Lord Jesus Christ. All glory and praise to Him.

## Dedication

*To all those who have guided, supported and helped me become the scientist and person I am today.*

## Contents

List of Figures . . . . .	7
List of Tables . . . . .	10
ABSTRACT . . . . .	11
Chapter 1 Introduction . . . . .	12
1.1 Background of Bose-Einstein condensates and quantum fluid dynamics	12
1.2 Previous studies performed in BEC Labs I and II . . . . .	15
1.3 Organization of the dissertation . . . . .	23
Chapter 2 Methods of BEC Creation, Trapping and Imaging . . . . .	24
2.1 Evaporation to BEC . . . . .	24
2.2 Blue-detuned optical trap designs . . . . .	26
2.3 Trapping configuration for <i>in situ</i> imaging of solitons and vortices . .	32
2.4 Improved imaging pulses for 2D clouds . . . . .	38
Chapter 3 2D Soliton Formation and Decay through BEC Merging . . . . .	44
3.1 Introduction . . . . .	44
3.2 Experimental design . . . . .	45
3.3 Experimental results for short time scales: 40 ms barrier ramp . . . .	48
3.4 Experimental results for short time scales: 13 ms barrier ramp . . . .	52
3.5 Experimental results for long time scales . . . . .	56
3.6 Single-shot measurements of vortex-handedness . . . . .	60
3.7 Conclusion . . . . .	64
Chapter 4 Forced Damping of a Superfluid Gas with a 1D Optical Lattice . .	66
4.1 Introduction . . . . .	66
4.2 Experimental set-up . . . . .	67
4.3 Lattice Properties . . . . .	68
4.4 Experimental procedure: Collecting baseline data . . . . .	73
4.5 Experimental procedure: Testing the vortex comb . . . . .	76
4.6 Experimental procedure: Counting the data . . . . .	80
4.7 Conclusion . . . . .	83

Contents – *Continued*

Chapter 5 Various Vortex Generation and Measurement Studies: Preliminary	
Results . . . . .	85
5.1 Vortex cluster/dipole creation via two-pulse poking procedure . . . . .	85
5.2 Vortex dipole pumping through magnetic field cycling . . . . .	91
5.3 Single-shot vortex measurements with 1D Shack-Hartmann wavefront sensor . . . . .	98
5.4 BKT transition near 2D limit of BEC . . . . .	100
Chapter 6 Apparatus Hardware Upgrades . . . . .	113
6.1 Magnetic bias polarity flipping electronics . . . . .	113
6.2 Reconfiguration of analog computer output source power . . . . .	117
Chapter 7 Conclusion . . . . .	120
Bibliography . . . . .	121

## List of Figures

1.1	Vortices from merging BECs from Scherer paper . . . . .	16
1.2	Spontaneous vortices from Weiler paper . . . . .	18
1.3	Vortex dipole study from Neely paper . . . . .	19
1.4	Dipole pair from vortex tweezers method . . . . .	19
1.5	<i>In situ</i> vortices from Wilson thesis . . . . .	20
1.6	Numerical study of BEC poking experiment by Lowney . . . . .	21
1.7	BEC science cell enclosure in BEC Lab II . . . . .	22
2.1	Side-profile image of blue-detuned dark trap. . . . .	27
2.2	Partial beam profile of dark trap laser beam after phase shifting glass slide. . . . .	28
2.3	Optical design of blue-detuned dark trap. . . . .	29
2.4	Comparison of the effect of initial BEC aspect ratio at loading on BEC heating. . . . .	31
2.5	Single-lobe dark trap periodic structure on BEC. . . . .	33
2.6	<i>In situ</i> image of solitons and vortices. . . . .	35
2.7	<i>In situ</i> vortices that are difficult to reliably identify. . . . .	37
2.8	Original optical design of vertical Faraday imaging system. . . . .	39
2.9	Momentum kicks to atoms in BEC during imaging. . . . .	40
2.10	BEC imaged with too little pump light. . . . .	41
2.11	New pump imaging light path. . . . .	43
3.1	Example image of soliton lines formed during BEC merging. . . . .	45
3.2	BECs separated by potential barrier before merging. . . . .	46
3.3	Soliton formation immediately after BEC merging: 40 ms ramp. . . . .	49

3.4	Initial soliton dynamics after formation: 40 ms ramp. . . . .	49
3.5	First signs of decay of solitons: 40 ms ramp. . . . .	50
3.6	Solitons showing no decay. . . . .	51
3.7	Significant soliton decay with vortex formation: 40 ms ramp. . . . .	52
3.8	Soliton formation immediately after BEC merging: 13 ms ramp. . . . .	53
3.9	Initial soliton dynamics after formation: 13 ms ramp. . . . .	54
3.10	First signs of decay of solitons: 13 ms ramp. . . . .	54
3.11	Significant soliton decay with vortex formation: 13 ms ramp. . . . .	55
3.12	Dissipation of most solitons with some visible vortices: 13 ms ramp. . . . .	56
3.13	Vortices after complete decay of solitons: 13 ms ramp. . . . .	57
3.14	Vortices after complete decay of solitons: 40 ms ramp. . . . .	58
3.15	Comparison of soliton bending near a vortex vs with no vortex present. . . . .	61
3.16	Numerically probing soliton bending near a vortex. . . . .	62
3.17	Bending of solitons dependent on vortex handedness. . . . .	63
3.18	Cases of vortices not significantly bending solitons. . . . .	63
3.19	Dramatic snaking of soliton. . . . .	65
4.1	Optical design of 532 nm optical lattice. . . . .	69
4.2	Intensity side-profile of optical lattice. . . . .	71
4.3	Optical lattice at different powers over BEC. . . . .	72
4.4	Vortices at various hold times after stirring. . . . .	75
4.5	Plot of the fraction of trials with a given number of observed vortices separated by optical lattice power. . . . .	77
4.6	Side-by-side comparison of BEC with and without vortex broom pro- cedure. . . . .	78
4.7	Plot of the fraction of trials with a given number of observed vortices separated by hold time with and without optical lattice. . . . .	81
4.8	Example of vortex counting procedure and classification. . . . .	82



5.1	Laser pulse waveforms and approximate locations on BEC. . . . .	87
5.2	Poking lasers at steady state interacting with BEC. . . . .	87
5.3	Procession of two-vortex cluster around BEC. . . . .	89
5.4	Other vortex distributions created via poking procedure. . . . .	90
5.5	Approximated laser pulse positions on BEC in forming vortices of Figure 5.3. . . . .	91
5.6	Illustration of magnetic pumping cycle. . . . .	93
5.7	Holes in BEC from interaction with zero-point of the magnetic field. .	95
5.8	Vortices produced from several magnetic pumping cycles. . . . .	96
5.9	Breathing modes of BEC excited after magnetic pumping cycles. . . .	97
5.10	Diffraction pattern of BEC after optical lattice pulse during expansion.	99
5.11	Images of vortices with the lattice pulse vortex measurement procedure.	101
5.12	Comparison of soliton bending and possible bending of diffraction lines from lattice pulse procedure. . . . .	102
5.13	Ramp time comparison of BKT vortices. . . . .	104
5.14	Possible vortex dipoles formed due to BKT mechanism. . . . .	105
5.15	Vortices formed at various trapping geometries approaching 2D limit.	107
5.16	Periodic structure on BECs while approaching 2D limit . . . . .	108
5.17	BE structure obscuring potential vortices even in expansion imaging.	109
5.18	Approaching 2D limit by reducing atom number in BEC. . . . .	111
6.1	Background images at camera positions of various atom cloud locations.	114
6.2	Circuit diagram for magnetic polarity flipping electronics. . . . .	117
6.3	Home-built power supply in BEC Lab II. . . . .	118
6.4	Commercial power supplies for powering computer output analog con- trol voltages. . . . .	119

## List of Tables

4.1	Contrast of the lines formed in the BEC due to the optical lattice at varying powers. . . . .	73
4.2	Table of the average number of vortices counted after varying hold times upon completing the “stirring” and barrier removal steps to generate vortices. 18 vortices represents a typical number of vortices counted for the 5 images taken at this hold time. . . . .	74
4.3	Average number of vortices counted per trial for each optical power data set. . . . .	79
6.1	Truth table for ADG436 Dual SPDT Switch used for current-flipping electronic circuit in bias magnetic coil systems. . . . .	116

## ABSTRACT

The transition from laminar to turbulent flow in a quantum fluid is marked by the formation of quantized vortices in a Bose-Einstein Condensate (BEC). Several studies were conducted investigating both the controlled formation of such vortices as well as the efficient removal of vortices from a BEC. By using specially designed optical fields and/or lattices, optical interactions with our BEC could be engineered to either create topological defects of interest in a BEC (such as vortices, dark solitons, and diffraction patterns) or remove vortices, restoring a turbulent BEC to a laminar state. These methods are new tools for probing the transition of a BEC between laminar and turbulent states, a transition of great interest in both quantum turbulence studies and in classical fluid mechanics.

## Chapter 1

## Introduction

### 1.1 Background of Bose-Einstein condensates and quantum fluid dynamics

A Bose-Einstein condensate (BEC) is formed when a gas of bosonic atoms is cooled to temperatures nearing absolute zero at which point another state of matter emerges exhibiting a unique set of physical properties. First hypothesized by Einstein in 1925 based upon a new proposal from Bose on how to statistically consider electromagnetic radiation [1, 2], a dilute-gas BEC was first physically realized in 1995 by the University of Colorado research team led by Cornell and Weiman [3].

Since the first experimental realization of a BEC, many of its properties have been the subject of much rigorous study. One such aspect of considerable interest has been the superfluid properties exhibited by BECs reminiscent of the well-known, viscosity-free superfluid helium-4 discovered much earlier in 1938 by Allen and Misener [4]. Some of these superfluid properties include phenomena such as second sound, frictionless fluid flow and quantized vortices, the last of which which will be discussed extensively in this dissertation [5].

Another aspect of significant interest was the macroscopic quantum wave nature of the BEC. As bosonic atoms are cooled to near absolute zero, many of them will occupy the ground state of the external confining potential. A single particle of mass  $m$  in a confining potential,  $V(\mathbf{r})$ , can be described with a single-particle wavefunction,  $\Psi(\mathbf{r}, t)$ , that evolves according to the Schrodinger equation,

$$i\hbar\frac{\partial\Psi(\mathbf{r}, t)}{\partial t} = \left(-\frac{\hbar^2}{2m}\nabla^2 + V(\mathbf{r})\right)\Psi(\mathbf{r}, t). \quad (1.1.1)$$

With many particles occupying the same quantum state in a confining potential, interactions between the bosonic atoms contribute significantly to the evolution of the system. The evolution of the many-body wavefunction corresponding to a BEC in a confining potential can then be described by the non-linear Schrodinger equation known as the Gross–Pitaevskii equation (GPE) [5],

$$i\hbar \frac{\partial \Psi(\mathbf{r}, t)}{\partial t} = \left( -\frac{\hbar^2}{2m} \nabla^2 + V(\mathbf{r}) + g|\Psi(\mathbf{r}, t)|^2 \right) \Psi(\mathbf{r}, t), \quad (1.1.2)$$

where the additional term,  $g|\Psi(\mathbf{r}, t)|^2$ , describes the contributions of the atom-atom interactions on the dynamics of the system. Here,  $g = 4\pi\hbar^2 a_s/m$ , where  $a_s$  is the s-wave inter-atomic scattering length.

Further investigations into BECs and the GPE have resulted in analytic solutions to the differential equation under specific parameters. Important to BEC research, the Thomas-Fermi solution is the result of solving the GPE while assuming large atom numbers as well as repulsive atomic interactions. These assumptions allow the kinetic energy term of the GPE,  $-\frac{\hbar^2}{2m} \nabla^2 \Psi(\mathbf{r}, t)$ , to be safely neglected. In one dimension, the simplified wavefunction then takes on the form

$$\begin{cases} \psi_{TF}(x, t) = \sqrt{\frac{\mu - V(x)}{Ng}} & V \leq \mu \\ \psi_{TF}(x, t) = 0 & V > \mu, \end{cases} \quad (1.1.3)$$

where  $\mu$  is the chemical potential and  $N$  is the number of atoms in the BEC. The chemical potential is the energy required to add one additional atom to the BEC and is used to define the healing length,  $\xi$ , of the BEC,

$$\xi = \sqrt{\frac{\hbar^2}{2m\mu}}. \quad (1.1.4)$$

Vitally important to the study of vortex dynamics in BECs, the healing length defines the length scale for the size of defects in the BEC, like vortices.

Additionally, the Thomas-Fermi approximation for a BEC in a harmonic confining potential is solved by an inverted parabolic function. In practice, this function

can be fit to the density profile of a BEC providing a measurement of the Thomas-Fermi radii of the BEC. Knowing only the trapping frequencies of the harmonic confining potential and atomic parameters, these Thomas-Fermi radii can readily be used to calculate atom number, healing length, and other parameters of interest for the BEC.

While BECs of all dimensions have intriguing fluid flow characteristics, interest in the fluid flow properties of 2D BECs became of particular interest in part due to the 2D point vortex model introduced by Onsager [6], a statistical description of point vortex behaviour as it relates to turbulent fluid flows. BECs have proved exceptionally useful platforms for studies of this point vortex model for a variety reasons. First, the confining potential traps for BECs can be engineered to approach the 2D regimes needed to produce and study 2D vortices. Second, the small healing lengths associated with these 2D dilute-gas BECs assures the vortices to be small and “point-like.” Finally, in the context of fluid dynamic studies, BECs provide a highly controlled platform for producing and observing the dynamics of vortices with a well-defined expected behaviour governed by the GPE.

Amazingly, Onsager’s insights allowed him to also predict that the extension of his theory into quantum fluids, such as BECs, would necessitate the quantization of the vortices themselves.

A BEC containing a disorganized number of such quantized vortices will begin to show signs of chaotic fluid flow, a signature characteristic of turbulent fluid states. In classical studies of turbulence, Onsager’s statistical point vortex model has been difficult to observe. However, the study of quantized vortices in BECs provides the promise of unifying a statistical description of turbulence in the context of well-defined quantum mechanical first principles. It is hoped that such a union will bring new insights into the dynamics of 2D quantum turbulence and, by extension, a better understanding of turbulence universally.

## 1.2 Previous studies performed in BEC Labs I and II

At the University of Arizona under the advisement of Brian Anderson, BEC Labs I and II have made efforts to contribute to a better understanding of 2D quantum turbulence through experiments probing the formation and dynamics of quantized vortices in BECs. The first such experiment was led by David Scherer in which the group studied the formation of vortices through the merging of 3 trapped BECs [7]. The results of this experiment found two major conclusions. First, the merging of three condensates with indeterminate phases produced vortices in the single resulting condensate correlating to the merge rate of the three-condensate system. This was a generally expected result as the non-uniform merging of the condensates imparted excess energy into the resulting BEC along with regions of non-zero angular momentum, conditions amenable to vortex formation. Secondly, in about 10% of the trials when the BEC was not split into three distinct condensates, vortices were observed. This second result was especially surprising as it challenged “the notion that a BEC *necessarily* forms with no angular momentum in the lowest energy state of a trapping potential.” Images of the initial three condensate set-up and the vortices produced after merging can be seen in Figure 1.1.

The second result from this experiment became the basis of an experiment performed in BEC Lab I, led by Chad Weiler, probing the cause of these spontaneous vortices [8]. Through a set of experiments at the University of Arizona and simulations performed by Ashton Bradley and Matthew Davis at the University of Queensland, a relationship was established between the growth rate of a BEC in its formation and the density of these spontaneously formed vortices. Specifically, the probability of observation of spontaneously formed vortices increased as the growth rate of the condensate also increased, qualitatively similar to the Kibble-Zurek mechanism [9, 10]. Thus, a condensate that is formed more quickly is more likely to contain spontaneously formed vortices. Figure 1.2 shows some of the vor-

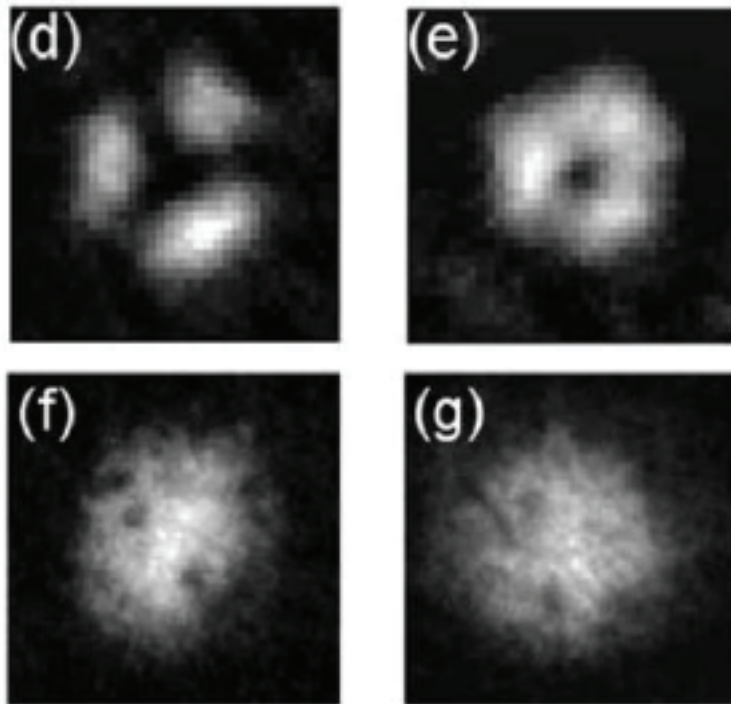


Figure 1.1: Select images taken from Figures 1 and 3 on pages 1 and 3 from Reference [7] showing the BECs before merging in (d), during the merge in (e) and populated with vortices after the completion of the merging step and subsequent ballistic expansion from the top in (f) and (g).



tices observed beside simulation data from [8].

An original goal of the Scherer experiment was the controllable nucleation of a vortex within a BEC. Further development of this idea was accomplished by later experiments in the lab. In one experiment led by Tyler Neely [11], instead of one singly-charged vortex, the group was able to demonstrate the reproducible nucleation of a vortex dipole pair by forcing superfluid flow around a potential barrier, within a BEC, moving above a critical velocity. These experiments were in good agreement with simulation studies which can be seen alongside the vortex dipole pair dynamics in Figure 1.3.

Following Neely, Edward Carlo Samson led an experiment showing controllable vortex dipole creation in conjunction with vortex pinning by laser tweezers. To create a vortex dipole pair, he utilized a localized beam swiping procedure called the “vortex tweezers” which produced a vortex pair in their wake after being swept through the condensate. Vortices produced by this method can be seen in Figure 1.4.

Another aspect of the Scherer experiment that remained of interest was the existence of fringes and solitons formed during BEC merging, as seen in numerical simulations, that led to vortex formation. Because of their highly nonlinear dynamics, the dynamics of solitons could not be adequately studied in BECs imaged with ballistic expansion. To allow for future study of the *in situ* dynamics of vortices and solitons, Kali Wilson led new imaging techniques and designs to realize *in situ* imaging of vortices and other defects. This effort resulted in the *in situ* vortex images shown in Figure 1.5. Additionally, the imaging research pursued by Wilson in [13] proved invaluable in future *in situ* vortex and soliton imaging procedures implemented in BEC Lab II.

In addition to working on vortex generation and detection, Joe Lowney contributed significant numerical studies to the research group. A significant portion of his numerical research centered upon a new technique for vortex dipole generation

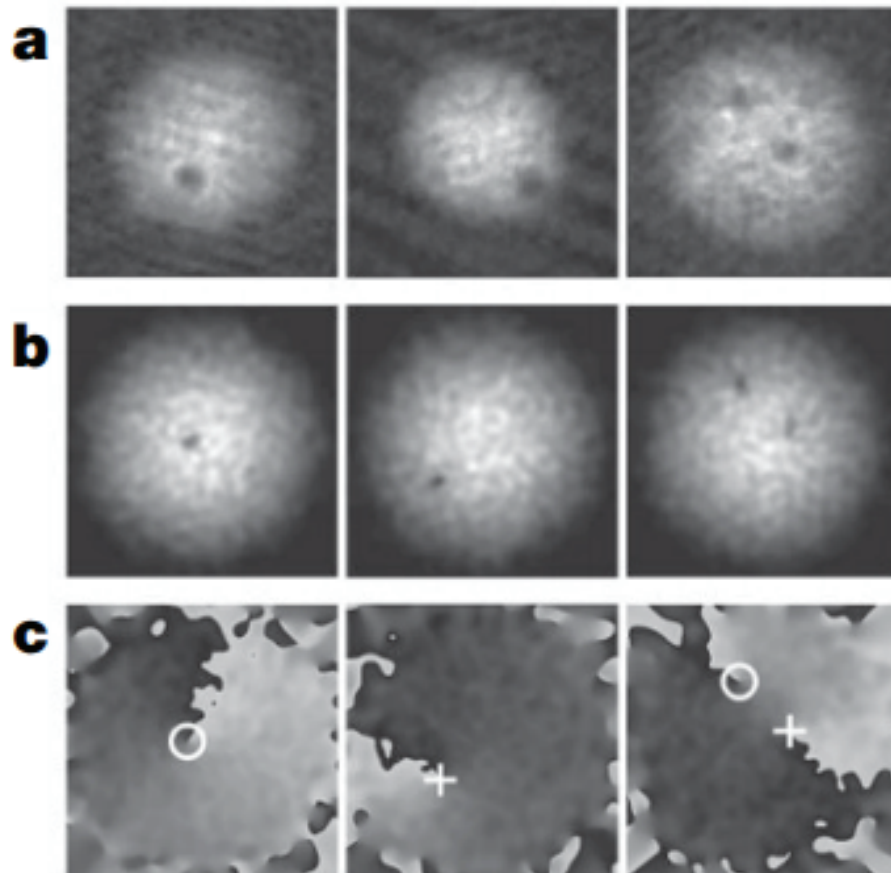


Figure 1.2: **a**, Images of vortices within BECs produced with fast BEC growth rate. **b**, Images of simulations performed by modeling the experimental parameters of the images in **a**. **c**, Images showing the phase profile of the simulation images with vortex positions marked by plus or minus signs. From Reference [8] Figure 3.

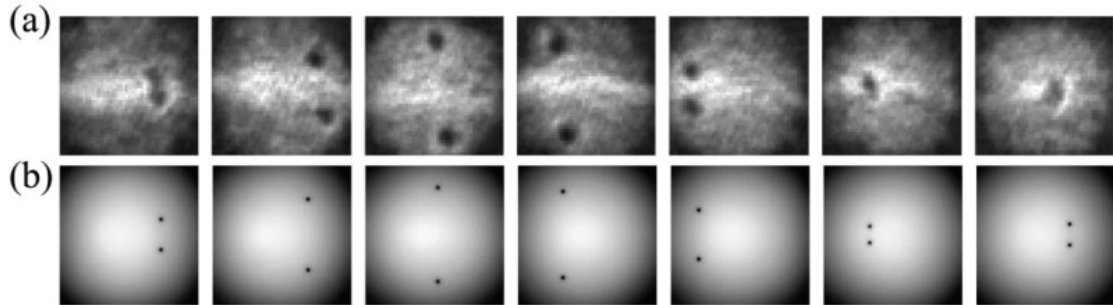


Figure 1.3: The images in row (a) show the experimental observation of vortex dipole dynamics along with showing the repeatable ability to inject a vortex dipole into a BEC at a predictable position. The images of row (b) show simulation data in agreement with the experimental data of row (a). For each row, time increases to the right, indicating motion of the vortices. Figure taken from Reference [11] Figure 3.

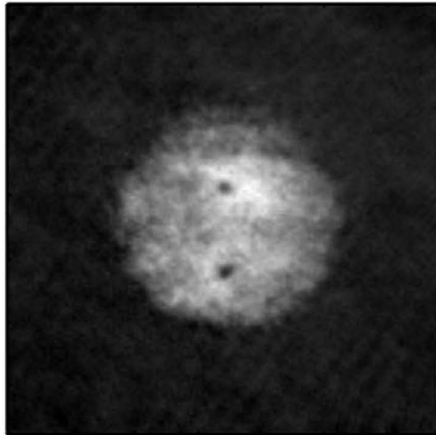


Figure 1.4: Images of a vortex dipole created after the vortex tweezers technique taken from and described in Reference [12] Figure 6.3.

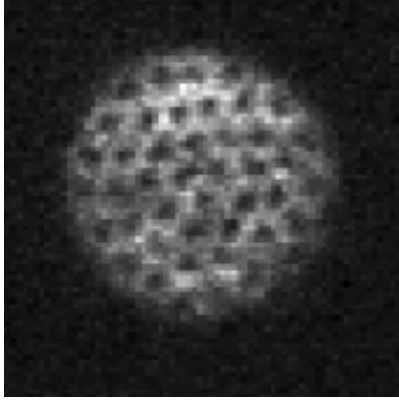


Figure 1.5: Among the first images of a BEC demonstrating *in situ* imaging of vortices using the BEC Lab I apparatus as described in Reference [14] Figure 8.20.

using two pulsed laser beams on a 2D BEC [15]. This numerical study demonstrated a technique capable of injecting a vortex dipole pair into a BEC with short, minimal and local perturbations allowing the majority of the BEC to evolve mostly unperturbed by the laser pulses. Figure 1.6 shows sample figures from the simulations of the two beam poking study.

Around this time, Zachary Newman and Jessica Myers began building BEC Lab II, the lab in which the experiments described in this dissertation were performed. In his dissertation, Newman described the many technical advancements made to the BEC Lab II BEC apparatus to enable better and more consistent BEC creation and imaging resolution [16]. One important design objective centered around his compact design of the science cell and the surrounding magnetic coils and coil mounts. The chosen design allowed for the use of a high NA commercial microscope objectives for more advanced *in situ* imaging capabilities than possible in BEC Lab I. Additionally, the compact magnetic coil design allowed for more flexible atomic trapping geometries and procedures due to the lower currents needed for cooling and trapping the condensates. Figure 1.7 shows several key aspects of the BEC apparatus designed and installed in BEC Lab II.

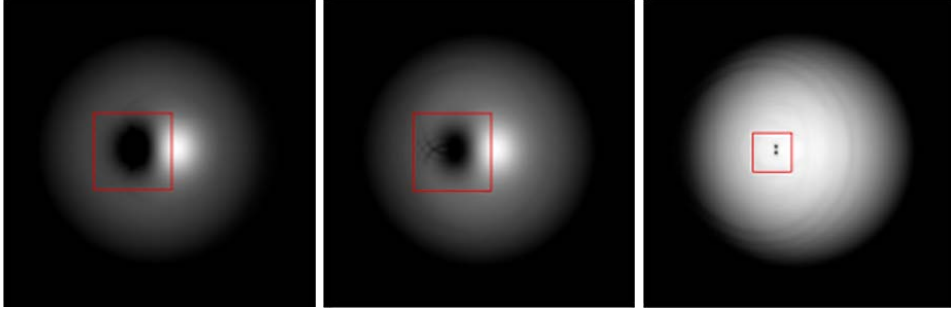


Figure 1.6: Sample figures from a numerical study of vortex dipole creation through a two beam poking procedure. The three images occur sequentially. First, the leftmost image shows two lasers focused on the BEC, one repulsive (dark spot) and one attractive (bright spot). The middle image shows the atoms leaving the brighter spot and filling the darker spot shortly after the lasers are turned off. Finally, the rightmost image shows the resulting vortices of this flow configuration in a BEC after a short hold time. These images are taken from Reference [15] Figure 4.12.

Jessica Myers contributed extensively to the construction of BEC Lab II. She also conducted the first 2D quantum turbulence study using the apparatus [17]. In her work, Myers explored the flexible trapping geometries offered by the new hybrid optical/magnetic BEC trap. In addition to accomplishing an experiment probing the effects of thermal counter flow in BECs, the work of Myers resulted much of the groundwork for future use of the apparatus. For this apparatus, she demonstrated the first vortex imaging, the first efforts towards *in situ* vortex imaging, the first splitting of a BEC with an optical barrier, and the development of the current Faraday imaging system used for vortex observation.

Finally, Samuel Nerenberg proposed and simulated a novel vortex measurement technique using an “atom-optic Shack-Hartmann wavefront sensor” [18]. The design of his wavefront sensor and the simulations showing its potential in extracting phase data from a BEC show promise in future 2D quantum turbulence studies in BECs.

The experiments discussed in this PhD dissertation, the tenth of the University of Arizona BEC research group, are direct or indirect extensions of previous efforts

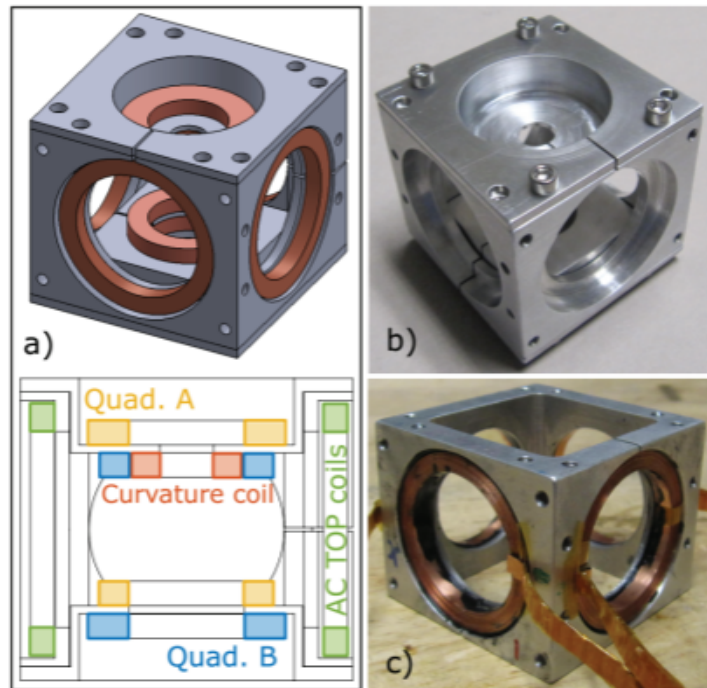


Figure 1.7: Images of the enclosure holding the magnetic coils for the BEC trap in BEC Lab II designed especially for enabling the use of a high NA commercial microscope objectives. This shuttle (roughly a 2" cube) was also constructed to slide around the glass science cell where BEC experiments could be performed at the center of the magnetic coil arrangement. Close proximity of the coils to the atoms also enabled the use of stronger magnetic fields at with lower currents. Pictures and Figures taken from Reference [16, 17].

from these past research group members.

### 1.3 Organization of the dissertation

This dissertation has the following organizational structure.

Chapter 2 contains the methodology of BEC creation, trapping, and imaging. Much of the original procedure of BEC making remains almost identical to the procedure described in detail in [17]. However, a summary of this process is described in Section 2.1. The remainder of Chapter 2 addresses several of the design changes needed to realize *in situ* imaging.

Chapters 3, 4, and 5 detail the various experiments of my dissertation. Chapters 3 and 4 each contain experimental studies carried out to completion. On the other hand, Chapter 5 describes four different experiments for which preliminary data were taken, but more work will be necessary to reach satisfying conclusions.

Finally, Chapter 6 describes a few of the technical hardware upgrades to the BEC apparatus in BEC Lab II.

## Chapter 2

### Methods of BEC Creation, Trapping and Imaging

#### 2.1 Evaporation to BEC

The process of evaporation to a BEC in BEC Lab II is well-documented in [16, 17]. This section is a short summary of the current generalized steps in the creation of  $^{87}\text{Rb}$  BECs.

$^{87}\text{Rb}$  atoms are first evaporated to a gaseous state by running 3.15 A of current through a Rb dispenser (SAES) in the apparatus. The atoms are then pre-cooled by a 2D magneto-optical trap (MOT) which serves as a loading tool for a 3D MOT. The atoms are given momentum kicks along the untrapped dimension of the 2D MOT by a beam of 400  $\mu\text{W}$  near-resonant light through a pinhole toward the 3D MOT. Atoms are slowly collected at the 3D MOT over about 10 to 30 seconds until the 3D MOT is fully loaded with roughly  $10^9$  atoms. Finally, after being fully loaded, the atoms are magnetically trapped and transferred to a magnetic quadrupole trap in the science cell.

Further cooling in the science cell is accomplished through several different techniques of evaporative cooling. The first technique used is radio-frequency (RF) cooling. Once in the magnetic quadrupole trap, the spacial dependency of the Zeeman shifts experienced by the magnetically trapped atoms allow for RF magnetic fields to selectively remove the most energetic atoms that sample the edges of the trap allowing atoms closer to the center to adiabatically rethermalize to a colder temperature. At RF fields of about 10 MHz, an optical barrier potential, or plug beam, is required at the center of the quadruple trap to avoid significant atom losses to Majorana spin flips.



With RF-evaporation cuts down to 4.5 MHz, the atoms are transferred to a red-detuned optical trap which provides a strong optical confinement in the vertical direction ( $\mathbf{z}$ ), weak optical confinement across the beam's horizontal profile ( $\mathbf{y}$ ), and negligible confinement along the beam's optical axis ( $\mathbf{x}$ ). Atoms remain trapped along the x-direction in the configuration due to the magnetic quadrupole field still present. Reasonable optical trapping of the thermal atoms requires about 5 W of power in the optical trapping laser with beam radii of  $29.5 \mu\text{m}$  and  $273 \mu\text{m}$  in the vertical and horizontal dimensions. Full transfer to the magnetic-optical hybrid trap occurs after the magnetic quadrupole trap has been displaced in the vertical direction by a vertical bias magnetic coil.

Once the hybrid trap is fully loaded, the final optical evaporation sequence slowly decreases the magnetic field gradient and the laser power in alternating steps. The change of magnitude and duration of each step varies among the different desired trapping geometries for different experiments. For example, trapping geometries in low magnetic field gradients require high optical powers resulting in elongated 2D BECs. By evaporating to BEC with gradients near 30 G/cm, the resulting BEC approaches a radially circular geometry. Generally, these steps occur over 2 to 5 seconds and change the magnitude of the gradient or optical power by no more than a factor of 5 in a given step. A typical BEC created in this manner has about  $10^6$  atoms with a vertical to radial aspect ratio of about 1:6.5 in their widths. At such aspect ratios, the fluid flow of the BEC is largely confined to the 2D radial plane. These condensates are thus referred to as 2D BECs.

Finally, diagnostic imaging of the thermal clouds and BECs was accomplished with absorption imaging of the side-profile of the atomic sample. This side-profile imaging samples the integrated absorption profile of the x-z plane along the y-direction. Side-profile expansion images utilized a 6.5 ms free fall time step before taking images.

To view vortices and other defects in 2D condensates, vertical Faraday imaging

sampled the density profile of the x-y plane integrated along the z-direction. Details regarding the imaging system layout and Faraday imaging procedure can be found in Reference [17]. To keep the BEC in focus during expansion for vertical imaging, a combination of magnetic fields was required to hold the BEC stationary against gravity for 8 to 10 ms before imaging.

## 2.2 Blue-detuned optical trap designs

For various experiments, including the Berezinskii–Kosterlitz–Thouless (BKT) transition experiment from Section 5.4, harmonic traps that are very 2D and/or circular provide a platform for probing questions pertaining to 2D quantum turbulence. For this reason, we designed and built a blue-detuned optical dark trap to provide a strong trapping force in the vertical direction with almost no trapping potential in its horizontal directions. A limitation of our red-detuned optical trap was the significant trapping force it provided across its beam width in addition to the trapping potential it provided vertically against gravity. Because of its coupling of the vertical and horizontal trapping forces, it was not possible to approach the 2D limit of a BEC with this set-up, the limit at which atomic motion in the tightly confined direction of the BEC is frozen in the ground state. This 2D limit will be further discussed in Section 5.4. Further details of the design choices regarding the 1064-nm trap can be found on page 66 of the thesis of Jessica Myers [17]. A new trap was needed to provide the necessary trapping geometries for the study of 2D BECs.

To create the blue-detuned trap, a glass slide was placed over the bottom half of the profile of a 532-nm beam and angle-tuned to cause an odd-integer multiple of  $\pi$  phase shift on the bottom half of that elliptical, Gaussian 532-nm beam. The result of this after some propagation and diffraction was approximately a  $\text{TEM}_{01}$  beam with the dark band in the center of the beam’s vertical profile. Some diffraction effects were present in the beam, but the beam’s profile, especially when focused, closely resembles the expected beam separation and width predicted by Gaussian

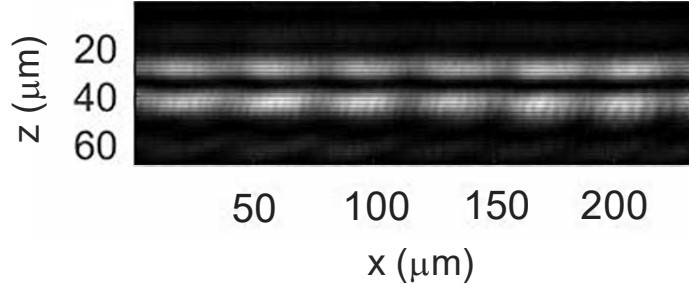


Figure 2.1: Image of the side-profile of an approximate  $\text{TEM}_{01}$  mode, 532-nm beam focused in the vertical direction at the atom location.

equations. Small diffraction effects, some horizontal periodicity and the dark trapping region can be seen in the images of the in-focus beam and the collimated beam found respectively in Figures 2.1 and 2.2.

The  $1/e^2$  horizontal and vertical beam radii at the BEC were  $570 \mu\text{m}$  and  $17 \mu\text{m}$  respectively. Vertical trapping was dominated by the blue-detuned trap as expected. With a wide beam and a long Rayleigh range relative to the size of the BEC, transverse optical forces were small relative to the magnetic trapping forces which in turn dominated the horizontal trapping strengths. Additionally, with a wide trapping beam, there was little variation across the radial dimensions of the BEC in vertical trapping strengths. This was advantageous in preventing unwanted leaking of the atoms out of the trap in the presence of small positional fluctuations of the horizontal position of the BEC.

To load the dark trap, a BEC of about  $6 \times 10^5$  atoms was prepared in an red-detuned optical dipole-plus-magnetic field trap with trapping frequencies of approximately  $(\omega_x, \omega_y, \omega_z) = 2\pi \times (6.8, 10, 70)$  Hz. The trap was formed by a 82 mW 1064 nm laser beam focused tightly in the z-direction and weakly in the y-direction. The z-direction trapping was dominated by this laser. The atoms were also in a vertically offset magnetic quadrupole field with a magnetic field gradient of about 27

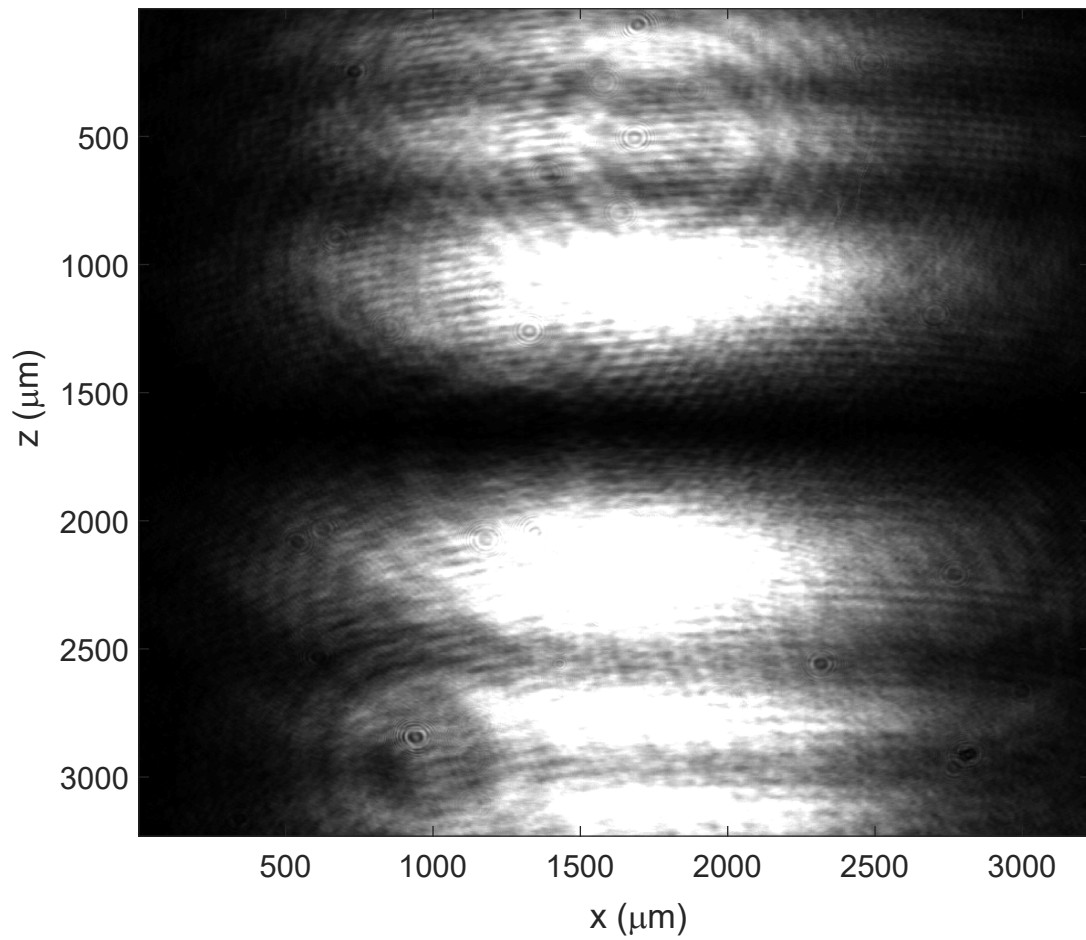


Figure 2.2: Side-profile image of the collimated, approximately  $\text{TEM}_{01}$  mode, 532-nm beam after 1 m of propagation after the phase shifting plate.

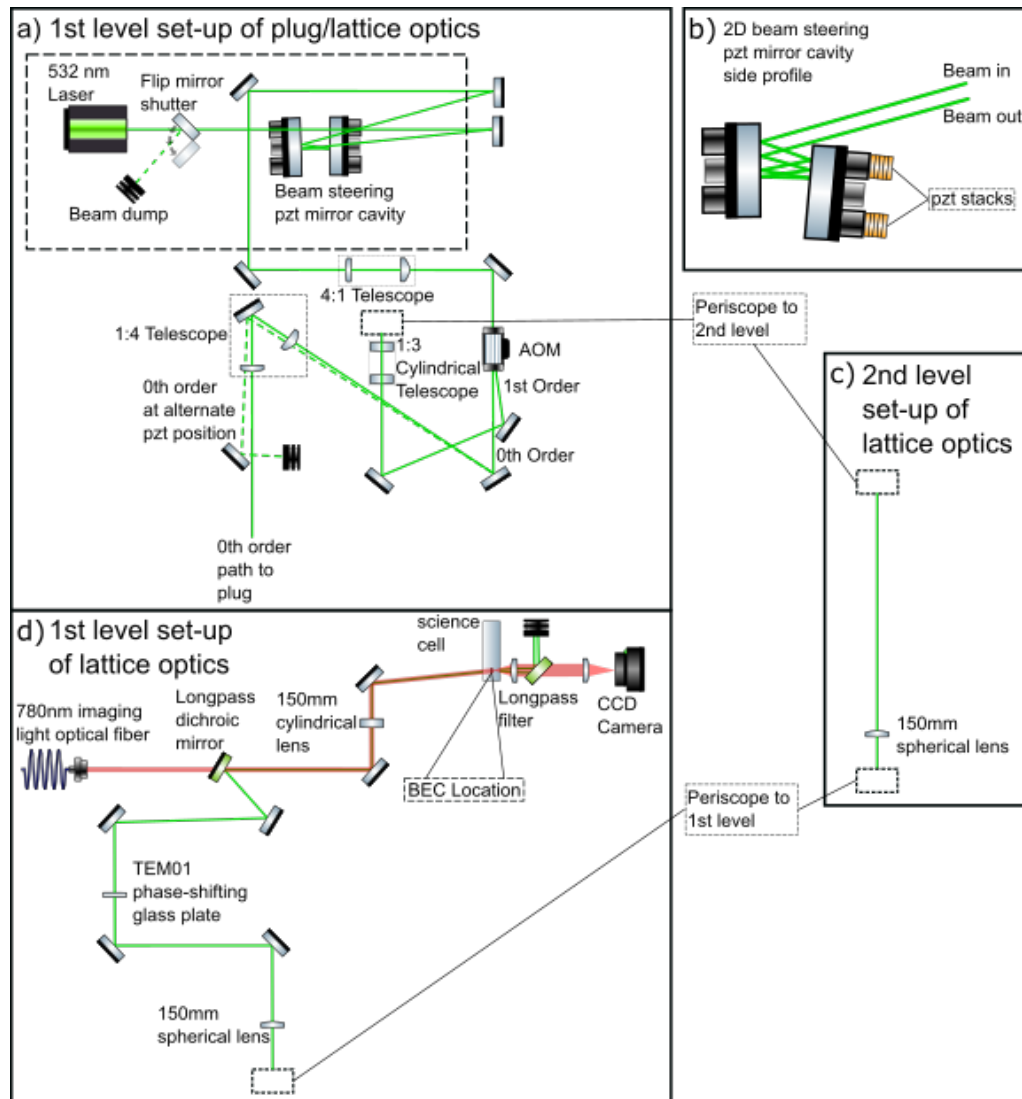


Figure 2.3: Optical set-up of blue-detuned trap. The trap was sourced from the 1<sup>st</sup> order deflection of the plug light off an acousto-optic modulator (AOM) as seen in a). The PZT beam-steering cavity in b) allowed for computer positional control of both the optical plug and the blue-detuned trap. The trap was then recollimated to the ideal beam parameters, phase shifted at the glass plate to approximate a TEM<sub>01</sub> mode, and focused in the vertical direction at the BEC to produce a tightly confined dark trap in c) and d).

G/cm. The atoms were displaced by about 0.13 cm below the magnetic field center and provided a trapping potential in the x and y-directions as well as partially balanced gravity allowing optical trapping at lower optical intensities. Trapping in the x-direction was then dominated by the magnetic field while trapping in the y-direction was a combination of magnetic and optical dipole forces.

Other more elliptical traps have been found to produce BECs with more atoms ( $\sim 10^6$ ) as seen in the vortex broom experiment from Chapter 4, but this more circular initial trap allowed for more efficient transfer into the circular, 532 nm blue-detuned optical dipole trap. Examples of the BEC after transfer into the blue trap are shown in Figure 2.4. Figure 2.4b shows a significant thermal component due to heating of the BEC experienced after transferring a very elliptical BEC with a transverse aspect ratio of 1:5.3 into a circular trap. Figure 2.4a shows a much less significant thermal cloud after transferring a much less elliptical BEC with a transverse aspect ratio of 1:1.5 into the same circular trap. These images of the BEC were taken after 7 ms of free fall after the BEC transfer to the circular trap from each of the two initial trapping configurations discussed above.

As will be described further in Section 5.4, the approximated (and simulated) trapping strengths of this set-up immediately after transfer were  $(\omega_x, \omega_y, \omega_z) = 2\pi \times (6.8, 6.8, 230)$  Hz. Due to heating during transfer from exciting breathing modes in the BEC, increase of 3-body recombination losses and continued background collisions, it was assumed there was about a 30% loss of atoms over the 3 s transfer process. The 3 s ramp was comprised of the 532 nm laser being linearly ramped up to about 350 mW over the first two seconds. The 1064 nm laser ramp was delayed by one second and then linearly ramped off from 100 mW over the final 2 s. Horizontal bias fields ramps were set to keep the clouds position unchanging as the lasers were ramped slowly. This was vitally important because the dark trap was found to have significant structure which would greatly exasperate heating associated with any slosh of the BEC. After completing the transfer to the new trap and applying a hold

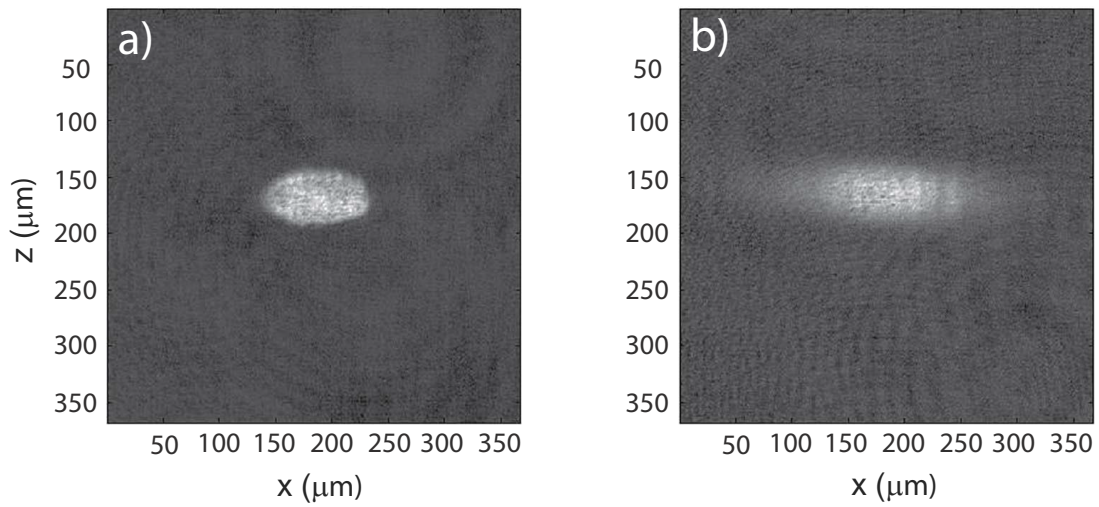


Figure 2.4: a) Image of the side-profile of a BEC after expansion upon transfer from an 82 mW 1064 nm elliptical trap with an aspect ratio of 1:1.5 to the circular 532 nm trap. Very little thermal component shows evidence of little heating during transfer. b) Image of the side-profile of a BEC after expansion upon transfer from an 450 mW 1064 nm elliptical trap with an aspect ratio of 1:5.3 to the circular 532 nm trap. A significant thermal component shows evidence of significant heating during transfer.

time long enough to allow the BEC to come to its ground state equilibrium, the condensate fraction remained at roughly 0.85.

As shown later in Section 5.4, the structure on the beam of the dark trap became significant as the trapping geometry became more 2 dimensional. Because of the known diffraction of the light from the phase shifting glass plate, it was hypothesized that this plate may be the cause of the periodic structure. To test this, a new dark trap was built by removing the glass plate. The result was a wide Gaussian beam focused tightly, vertically just below the BEC. Because a second, repulsive potential above the atoms was no longer present, this trap did not have the range of vertical trapping strengths as did the other set-up. The trap instead worked by using gravity to hold the atoms against the single-lobed blue-detuned laser barrier trap while magnetic trapping still defined the horizontal BEC position. Images of the vertical profiles of the BEC at the 3.5 G and 6.7 G magnetic bias configurations described in Section 5.4 can be seen in 2.5a and 2.5b, respectively.

However, as shown in Figure 2.5, periodic structure on the BEC can clearly be seen providing strong evidence that the new trap did not solve the beam structure problem. The likely culprit of this structure was then thought to be the result of the science cell. With known structure on the 1064-nm trapping laser through a different science cell window, it is not unexpected that the science cell is to blame for the structure found in both optical traps. Replacement of the science cell seems to be necessary for solving this issue of beam structure. Because of the experimental build-up and optimization of magnetic and optical systems around this science cell, replacement would be a difficult and time consuming ordeal for a future student.

### **2.3 Trapping configuration for *in situ* imaging of solitons and vortices**

The 1064-nm optical dipole trap is an important component in each of the experiments discussed in this dissertation. After an initial RF-evaporative cooling step, it provides the trapping force necessary to hold atoms while evaporating the atomic



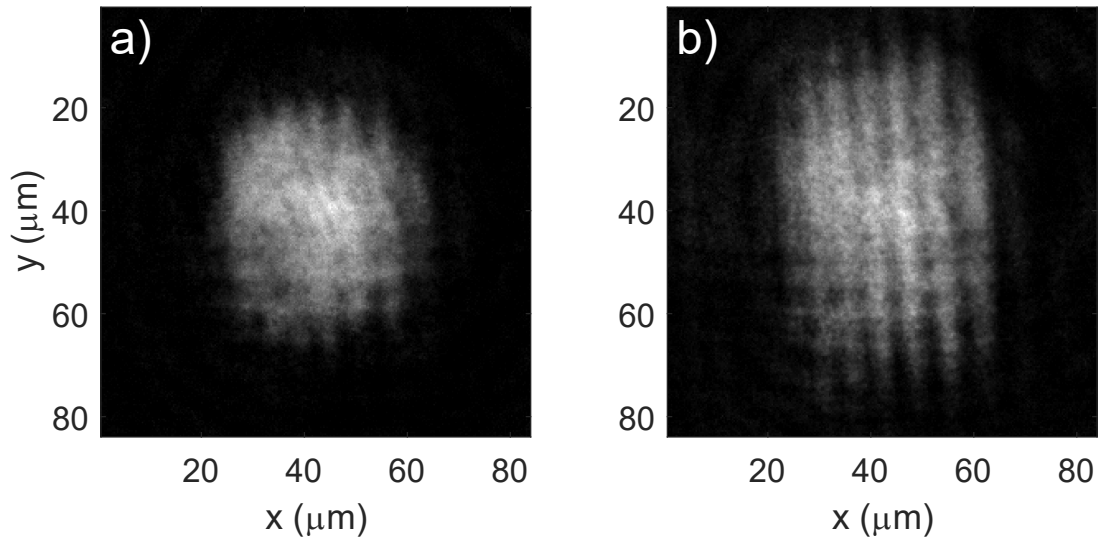


Figure 2.5: Vertical *in situ* BEC images at the a) 3.5 G and b) 6.7 G, respectively, magnetic bias configurations described in Section 5.4. The BECs are held in the single-lobe blue-detuned hybrid optical and magnetic trap.

sample condensation. Depending on the experiment, the atoms were held in this trap for 20 to 50 seconds during evaporation and experimentation. For this reason, power stabilization in the laser was important to ensure that noise in the laser power over these long time scales did not significantly contribute to heating of the atom cloud.

The design and installation details of the optical trap and the power stabilization can be found in the dissertation of Jessica Myers [17]. When calibrating the power stabilization circuit, it became apparent that the circuit worked optimally for powers above 80 mW when properly aligned. For this reason, the efficacy of trapping configurations using powers lower than this threshold were not initially explored. However, after successfully trapping and holding atoms for several seconds in the various dark traps described in 2.2 which did not have any power stabilization circuit, it was deemed worthwhile to further explore the trapping limits of the power-stabilized 1064-nm trapping laser.

The BEC healing length,  $\xi$ , is the length scale defining the size of topological and other defects in BECs such as vortices and solitons and is defined by

$$\xi = \frac{1}{\sqrt{8\pi a_s n_0}} \quad (2.3.1)$$

where  $a_s$  is the scattering cross section of the atom and  $n_0$  is the density of atoms. It is evident then that the length scales of the defects important to studies of quantum turbulence are then inversely proportional to the square root of the atomic density of the BEC. Given this and the importance of *in situ* observation of solitons and vortices for experiments such as the merging experiment described later in Chapter 3 or probing vortex dynamics in a single BEC with non-destructive imaging [14], it was highly desirable to achieve a trapping configuration in which density was reduced enough to resolve and observe *in situ* topological defects.

Experimentally, the two ways density of a BEC can be reduced are through reducing the number of atoms or relaxing the trapping forces on the atoms. For

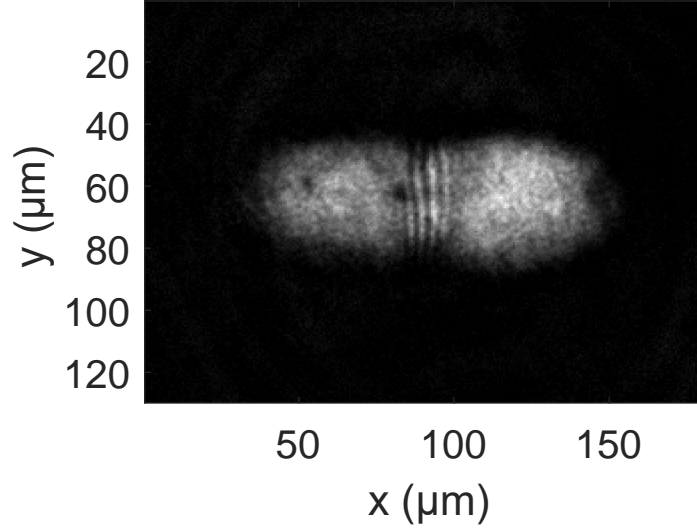


Figure 2.6: *In situ* image of BEC with visible soliton lines and vortices. Some curvature of the solitons can also be seen in the solitons nearest the vortex near the center of the BEC.

our purposes, atom numbers between  $5 \times 10^5$  and  $10^6$  were found to provide a large enough platform to conduct 2D quantum turbulent studies. However, at typical trapping frequencies of  $(\omega_x, \omega_y, \omega_z) = 2\pi \times (6.3, 9.8, 67.7)$  Hz, such atom numbers led to healing lengths of  $\xi \approx 0.40 \mu\text{m}$  which was too small to be resolved reliably with our imaging system. These conditions corresponded to 1064-nm optical trapping powers of about 80 mW.

By decreasing the optical power of the 1064-nm beam to as little as 19 mW, trapping frequencies were reduced greatly while still maintaining a roughly 2D trapping geometry with  $(\omega_x, \omega_y, \omega_z) = 2\pi \times (3.0, 6.9, 31.5)$  Hz. The healing length in this trap with a BEC of  $3 \times 10^5$  atoms was about  $\xi = 0.61 \mu\text{m}$ . This significantly longer healing length allowed for *in situ* vortex and soliton detection as seen in the example images in Figure 2.6. This step was also instrumental to accomplish the BEC merging experiments in Chapter 3.

To achieve condensation at these much reduced optical powers, the net force of the magnetic gradient and gravity needed to be close to zero. Magnetic gradients of about 30.5 G were utilized for the conditions above. One effect of this configuration was that atoms evaporated out of the optical trap took longer to fall away from the trapped atoms. Because of this, much longer final evaporation time steps needed to be implemented to achieve a BEC repeatably and efficiently. For the merging experiment of Chapter 3, the last two time evaporation time steps were increased from 2.4 s and 1.4 s to 5.0 s each. Additionally, because the optical trapping field was much weaker, drifts in the magnetic gradient strength over the day became much more significant and could shift the BEC's vertical position by up to 10  $\mu\text{m}$ .

A second trap with slightly larger trapping frequencies was also found to allow for some *in situ* vortex detection as shown in Figure 2.7. This trap operated at about 35 mW of power in the 1064-nm beam and resulted in trapping frequencies of  $(\omega_x, \omega_y, \omega_z) = 2\pi \times (2.8, 8.5, 38.5)$  Hz. However, this trap created BECs with defects at the edge of the imaging system's resolution. This was found to be problematic because any drift in the BEC's vertical position would quickly cause vortices to become obscured. While *in situ* imaging of vortices was possible in this set-up used in the vortex comb experiment described in Chapter 4, imaging vortices after some expansion proved to be the more reliable method of vortex detection.

Side note: while the magnetic field drift needed to be accounted for to keep the BEC in focus of the imaging system over the course of an experiment, this ability to shift the vertical position using small changes to the magnetic gradient allowed for a convenient way to shake the atoms vertically to measure the vertical trapping frequency. This could be done simply by slowly ramping the gradient to even more closely match the force of gravity. Then, by snapping the gradient back to its initial trapping value before the ramp, the cloud could be seen oscillating about a center position on the side profile imaging camera.

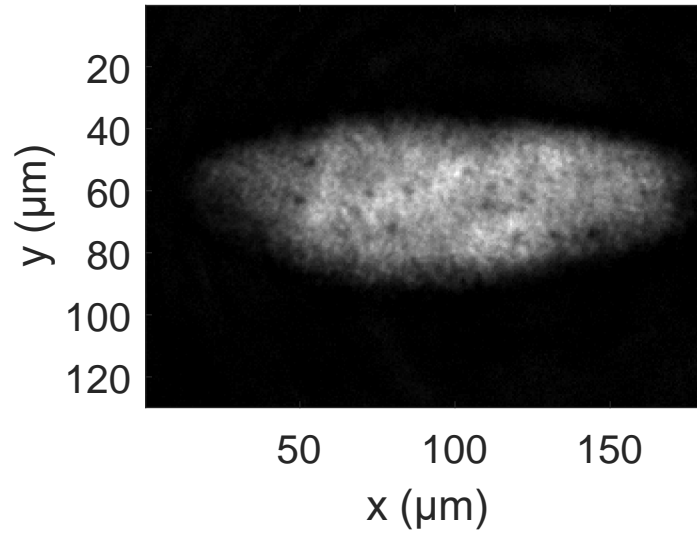


Figure 2.7: *In situ* image of BEC with vortices. Some vortices are fairly well resolved while most of the potential vortices are quite blurry. For these trapping parameters, expansion images provided much better reliability when counting vortices in a BEC.

## 2.4 Improved imaging pulses for 2D clouds

Optimizing image quality was a vital step towards successfully imaging *in situ* vortices. Experiments prior to the BEC merging experiment of Chapter 3 and the vortex comb experiment of Chapter 4 used a two-pulse imaging scheme as depicted in Figure 2.8.

Both our side-profile absorption imaging and top-down Faraday imaging systems imaged the atoms using the  $F = 2$  transition. Because the BEC was formed in the  $F = 1$  state, a pumping laser was needed to empty the  $F = 1$  state and place the atoms of the BEC in the  $F = 2$  state for imaging. The scheme shown in Figure 2.8 was adopted because of the convenience of being able to use the optical imaging path not being used for imaging as the pathway for inserting the pump light. This was particularly easy because both light pulses were fiber coupled and at nearly the same frequency. The only change in optics necessary to flip between the vertical and side-profile imaging systems was to swap the optical fibers. In this original schematic, the imaging and pump pulses were executed over two  $75\text{-}\mu\text{s}$  time steps.

It eventually became apparent that the BEC being imaged *in situ* was much thicker in the vertical, tightly trapped direction than was expected and was slightly asymmetric in the same direction. It was then deduced that the pump light was the likely culprit as the direction of the BEC distortions were correlated directly with the pump beam direction. Examples of this thickening and bending of the BEC relative to the pump light direction and pulse length can be seen in the images in Figure 2.9 along with the result of having fixed the pump pulse shutter timings.

In order to correct this, we found that shortening the durations of the two pulses made a significant improvement. Upon checking the numbers, a single absorption event of a photon with a wavelength of 780 nm would apply a significant momentum kick to a  $^{87}\text{Rb}$  atom. The velocity of the atom after such a kick was about  $5.9\ \mu\text{m}/\text{ms}$ . For a two-pulse scheme applied over  $150\ \mu\text{s}$ , an atom could travel al-

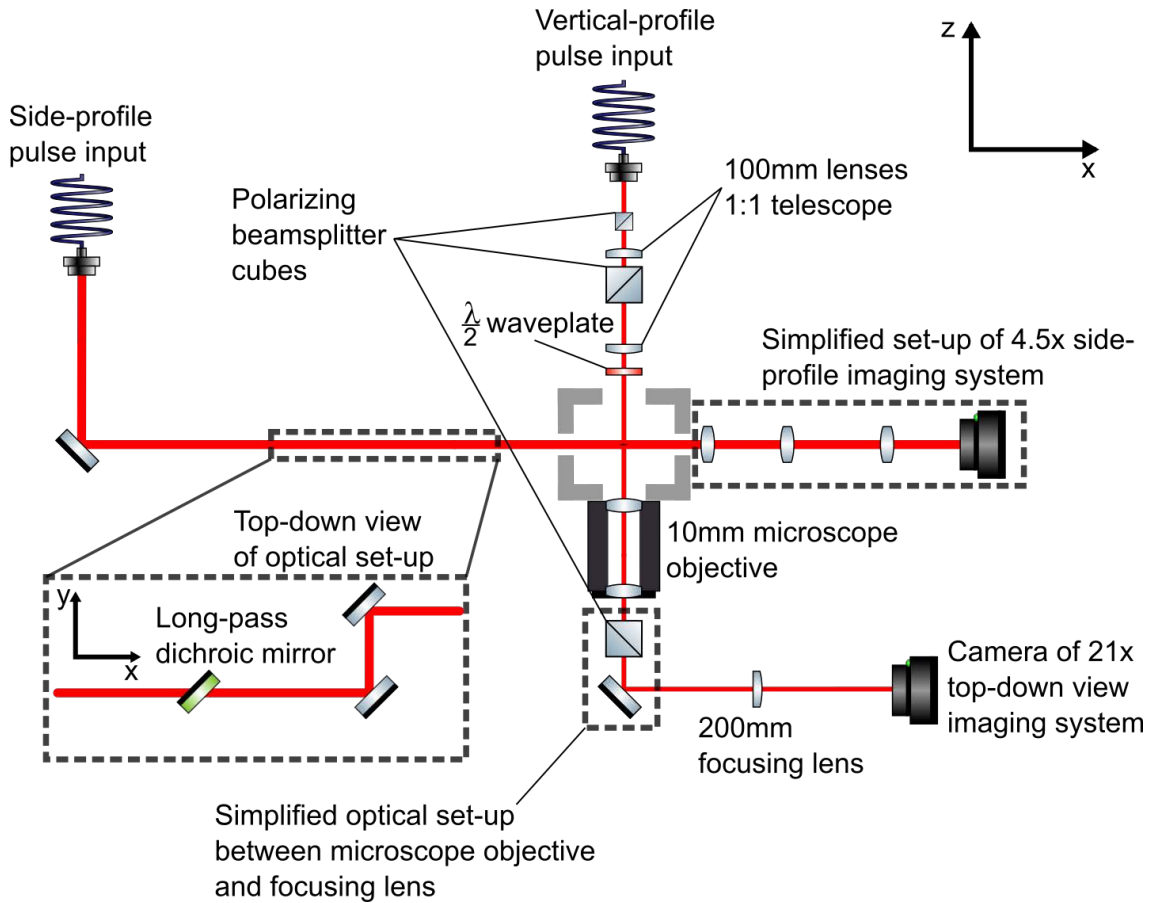


Figure 2.8: Original set-up of imaging pulse paths with some minor simplifications. For side-profile absorption imaging, pumping light was inserted into the vertical-profile pulse path to pump the atoms out of the  $F = 1$  state and into the  $F = 2$  state. The  $F = 2$  imaging light was inserted into the side-profile pulse path. For top-down Faraday imaging on the  $F = 2$  transition, pump light was inserted into the side-profile pulse path while the  $F = 2$  imaging light was inserted into the vertical-profile pulse path.

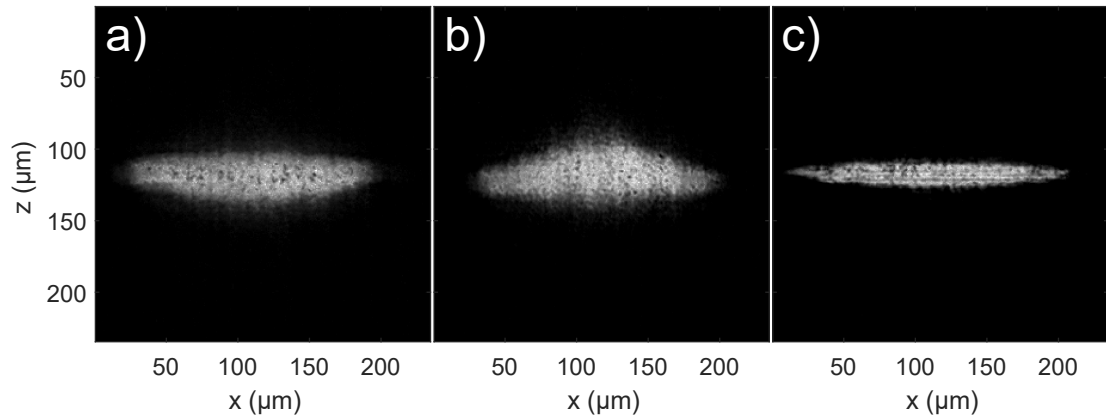


Figure 2.9: a) and b) show side-profile images of the optical density of the BEC with pump and imaging pulse timings of  $75 \mu\text{s}$ . For image a) the pump light is propagating from the top towards the bottom of the image. In b) the pump light is reversed propagating across the image from the bottom to the top. In image c) the pump and imaging pulse time steps have been reduced to  $30 \mu\text{s}$  each. The pump light is propagating from the bottom to the top of the image, but the BEC is not nearly as distorted as in a) or b) due the shorter pulse timings and the faster pump light shutter added which is depicted in Figure 2.11.



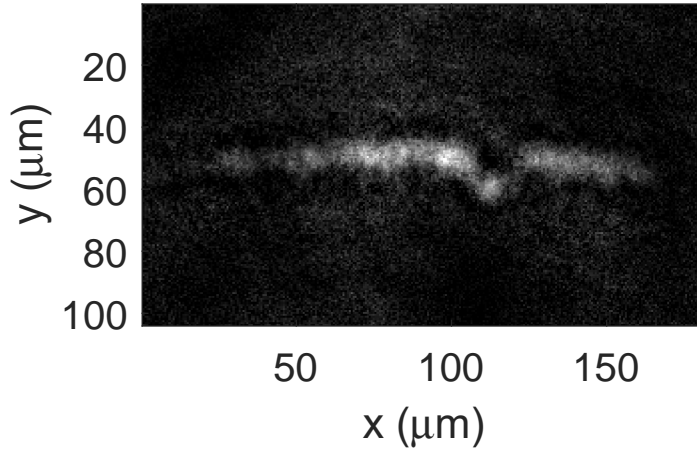


Figure 2.10: Vertical profile of BEC where pump light has been greatly reduced. Pump light direction is from the top to the bottom of the image. With too dense of an optical density from the side, the pump light only pumps the atoms at the edge of the BEC which are then the only atoms visible in the Faraday image taken.

most  $1 \mu\text{m}$ . Additionally, because the pump light pulsed before the imaging light and was propagating through the science cell horizontally across the BEC when set up for vortex detection imaging, momentum kicks were most significantly in the plane of the BEC. With healing lengths on the order of about  $0.5 \mu\text{m}$ , this was likely blurring out any vortices during imaging.

To correct this problem, we first attempted to simply decrease the pulse durations of both the imaging and pump light. While this seemed to work for the side-imaging system, it became apparent in the vertical imaging system that aligning the pump light parallel with the 2D BEC was far from optimal and resulted in only pumping atoms along the edge of the BEC in a crescent-like shape as shown in Figure 2.10.

To more efficiently pump the atoms for imaging, a new optical path was devised to insert the pump light in a counter propagating path to the imaging light. This had several advantages. First, due to being oppositely aligned, the absorption

events from the imaging and pump pulses would result in momentum kicks that would nearly cancel each other out. Additionally, because the optical depth of the atomic cloud was much more shallow in the perpendicular direction compared to the parallel direction, much shorter and less powerful pump pulses could be utilized to successfully pump atoms to the  $F = 2$  state for imaging. The new schematic took advantage of an already existent beam dump in our Faraday imaging system to insert the pump light in this new direction. Finally, the new path also allowed for a high-speed, high-performance shutter and beam shaping optics to be inserted into the pump light path for better control of the shutter open and close times. The schematic of the current pump and imaging pulse pathways are detailed in Figure 2.11.

It should also be noted that the new set-up will be hugely advantageous for any future efforts in making a vortex dynamics movie as very weak pump pulses that are uniform over the BEC in the 2D plane are necessary for the multi-shot sampling of the BEC. Too strong of a pump beam will over-sample the BEC destroying the BEC. A non-uniform beam over the BEC will result in a non-uniform sampling of the BEC. The crescent shaped BEC image in Figure 2.10 is an extreme example of non-uniform BEC sampling due to a poorly aligned pump beam.

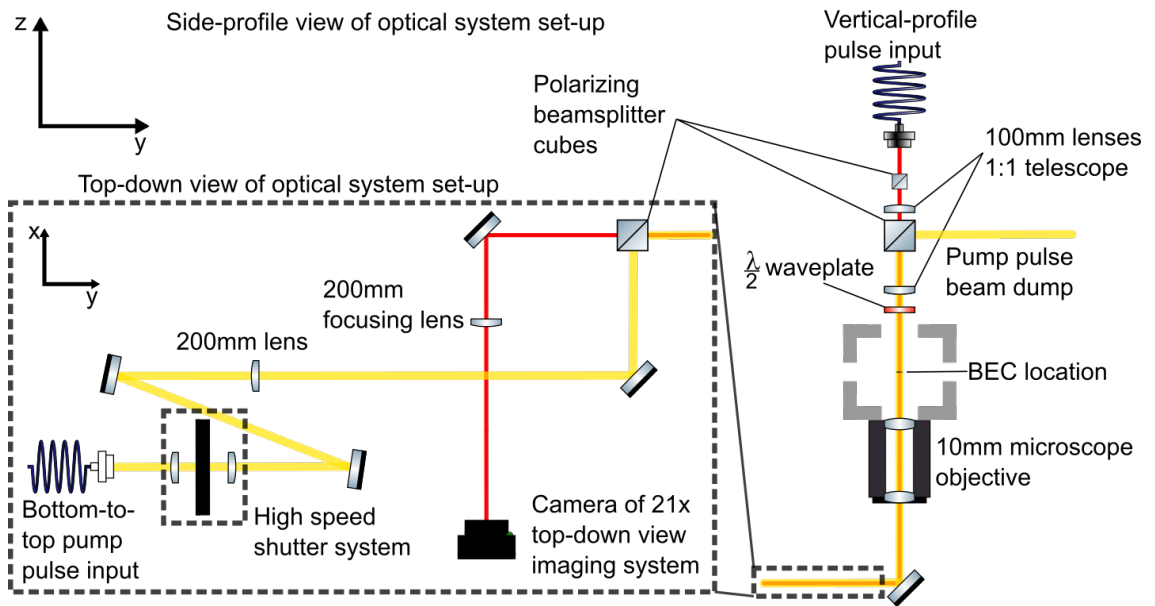


Figure 2.11: New optical set-up of pump pulse path for both imaging systems. pump light is shown here as a wider, yellow beam of laser light. It follows a path that combines with the  $F = 2$  light traveling in the opposite direction at the Faraday imaging light dump next to the microscope objective. Pump light is focused to a spot just before the microscope objective so that pump light exiting the objective is nearly collimated. Because of the polarization of pump light combined at the Faraday light dump, the pump light is expelled at the next polarizing beam splitter.

## Chapter 3

### 2D Soliton Formation and Decay through BEC Merging

#### 3.1 Introduction

Soliton waves, much like vortices, are ubiquitous throughout nature. The study of solitons and their dynamics has an especially long history in the field of fluid dynamics and wave propagation. In more recent years, dark solitons have been observed in nonlinear media such as self-defocused light [19, 20] and have been of interest for both mathematical nonlinear dynamical modelling [21] and for 2D turbulence studies in dilute-gas Bose-Einstein condensates [22]. Additionally, simulations and preliminary experiments were performed in our group by Wilson probing soliton line dynamics after the merging of two BECs [13]. The motivations for conducting the experiment discussed in this chapter were (1) to provide experimental data to compare with the nonlinear numerical models proposed for 1D soliton line arrays in [21], and (2) to probe the experimental efficacy of generating turbulence in a BEC through a 1D soliton line array akin to the 2D lattice used in [22] and more generally when two fluids collide and mix.

A soliton or solitary wave is a traveling, non-dissipative and shape-maintaining wave packet propagating through some media. This experiment specifically addresses the stability of a 1D array of dark-soliton lines in a 2D dilute-gas BEC. In a BEC, a dark soliton is seen as a single dark line of zero atomic density across the BEC. The wavefunction phase of the BEC across the soliton has a difference of  $\pi$  (black soliton) or less than  $\pi$  (gray soliton). An example of several of these dark soliton lines can be seen in Figure 3.1. These dark soliton lines are also known to be unstable in two dimensions and will decay into vortices through a mechanism called

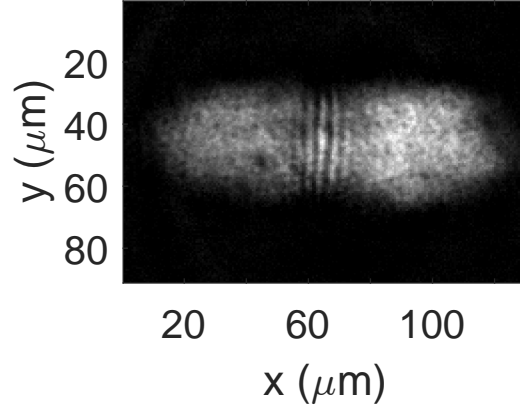


Figure 3.1: *In situ* vertical image of a BEC with several soliton lines across its center. These solitons were formed using the 40 ms barrier removal procedure described in Section 3.2.

the snake instability as discussed for the case of optical solitons and vortices found in [19], and for BECs in [23].

### 3.2 Experimental design

To reliably generate an array of dark solitons, a BEC of about  $3 \times 10^5$  atoms of  $^{87}\text{Rb}$  was produced over a 40-second cooling, loading and evaporation sequence described in the methods Section 2.1. The final trap in which experiments were conducted was a magnetic quadrupole/optical dipole hybrid trap with trapping frequencies of  $(\omega_x, \omega_y, \omega_z) = 2\pi \times (3.0, 6.9, 31.5)$  Hz. The  $\omega_z$  and  $\omega_x$  directions were dominated by the optical dipole forces and the magnetic quadrupole forces respectively. The  $\omega_y$  direction was trapped by a contribution of both the optical and magnetic trapping potentials. More detail on the trapping configuration used for this experiment is provided in Section 2.3. The choice of this trap was to intentionally achieve the lowest trapping frequencies realizable by the apparatus in order to enable *in situ* imaging of solitons and vortices in order to directly observe soliton decay without

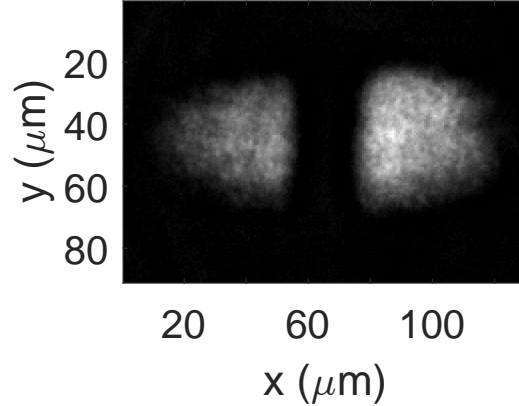


Figure 3.2: *In situ* vertical image of a pair of BECs with approximately equal atom numbers formed on either side of a potential barrier created from a 660 nm laser. The laser was focused tightly in the  $x$ -direction to a  $1/e^2$  beam waist radius of  $w_x = 14 \mu\text{m}$ .

first ballistically expanding the BEC.

To generate dark soliton lines in the BEC, an elliptically shaped blue-detuned 660-nm laser beam propagating vertically (along  $\mathbf{z}$ ) was focused tightly in the  $\mathbf{x}$ -direction of the BEC. This beam served as a repulsive barrier that separated the BEC into two clouds as seen in 3.2. Because of technical issues related to slosh and heating of the condensate when the beam was ramped on after production of the condensate, the final stage of evaporation to the BEC was performed with the repulsive barrier already on. Evaporation remained efficient in this trap and the barrier produced an anharmonic potential in the  $x$ -direction that allowed for the successful damping of any slosh imparted to the BEC during evaporation.

The barrier was measured to have a  $1/e^2$  beam waist radius of  $w_x = 14 \mu\text{m}$  and had a maximum potential of about  $2.0 \mu$  where  $\mu$  is the chemical potential of the BEC in the absence of the laser beam. After successfully producing BECs on either side of the barrier, the barrier was removed in a linear ramp allowing the two

atomic clouds to merge. The merging time was dependent on both the  $\omega_x$  trapping frequency and the time over which the barrier was removed. As the BECs began to overlap and merge, atomic fringes in the density profile were observed, as in Figure 3.1. This soliton train is similar to atom wave interference where each fringe is the result of constructive and destructive interference with one period corresponding to a  $2\pi$  relative phase shift [24].

After some short amount of time on the order of milliseconds, the fringes were expected to show evidence of soliton instability such as decaying into vortices through the snake instability mentioned earlier and as numerically observed in [21]. Although the slow merging of BECs was already known to create flow or even quantized vortices [7], the dynamics of the decay of a soliton train to vortices remained to be rigorously examined.

Finally, the number of solitons in the BEC could be controlled by adjusting the merging parameters. For BECs, the gradient of the phase profile is proportional to the local velocity of flow within the condensate. Thus, if the condensates merged at a faster velocity, the greater phase gradient associated with the condensates would result in more closely spaced interference fringes as the BECs began to merge. For a fixed region of space in the BEC in which fringes could appear, the greater frequency of fringes would correspond to a greater number of solitons excited as the interference fringes became dark solitons due to the BECs nonlinear dynamics. For this reason, two different barrier ramp down times of 13 ms and 40 ms were used in this experiment.

Additionally, the dynamics of the two merging time scales were analyzed for both short and long hold time scales after merging. Short time scales of 0 to 50 ms after the barrier removal rigorously probed soliton formation and decay immediately after merging. Long time scales of 50 ms to 2200 ms after the barrier removal probed the formation and persistence of vortices in the nominally turbulent BEC upon the decay of the solitons.

### 3.3 Experimental results for short time scales: 40 ms barrier ramp

For both the 13 ms and 40 ms barrier removal ramp times, the initial condition of the experiment was two separated BECs as shown in Figure 3.2.

For the 40 ms barrier removal condition, the atoms began merging and showing evidence of interference as the barrier reached its “off” condition. Images were then classified by their hold, or interaction, time after this point in the timing sequence. Over this hold time, the clouds were allowed to continue to merge in an unchanging trap.

Over the first 6 ms of hold times, the appearance of the atomic interference fringes can be clearly seen in the images in Figure 3.3. Vertical fringes first appeared at the center of the overlap point of the two condensates as seen in the 0 ms hold time image of Figure 3.3. As the clouds continued to merge over the first 6 ms, additional fringes started to appear periodically and parallel to the first fringes as the area of overlap of the BECs increased. Each image from Figure 3.3 is from a different run of the experiment, as is the case for subsequent figures in this chapter.

For slightly longer hold times of 7 ms to 12 ms, the fringes started to show soliton-like instabilities. First, as seen in Figure 3.4, the solitons lines began to show significant curvature. Additionally, the soliton depth became less well defined. Both of these phenomena are consistent with simulations of the decay of a 2D soliton into vortices via the snake instability [21]. Starting around hold times of 10 ms to 12 ms, the first evidence of vortex formation began to appear as circular density dips in the lines began to form at points along the snaking solitons. For the case of no preexisting vortices before merging, curvature in the solitons was most evident in the center soliton as the outer solitons regularly became much less defined with these hold times.

Finally, by 16 ms hold times, the snaking of the center soliton resulted in fracturing of the soliton as shown in Figure 3.5. This fragmenting is the expected result



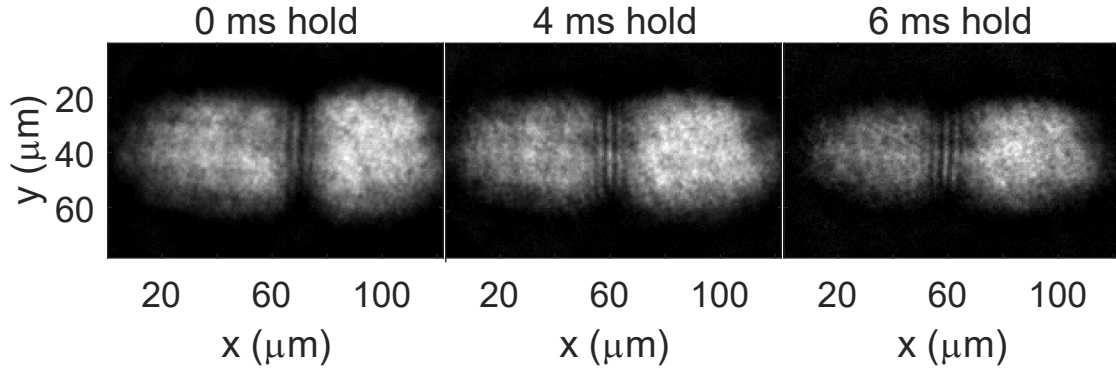


Figure 3.3: *In situ* vertical images of the BEC after 0 ms, 4 ms and 6 ms hold times following a 40 ms barrier ramp off time. Interference fringes, which eventually became soliton lines, began to form as the barrier ramp was completed at the 0 ms hold time. More fringes appeared as the BECs continued to merge over the 6 ms period following the barrier removal step.

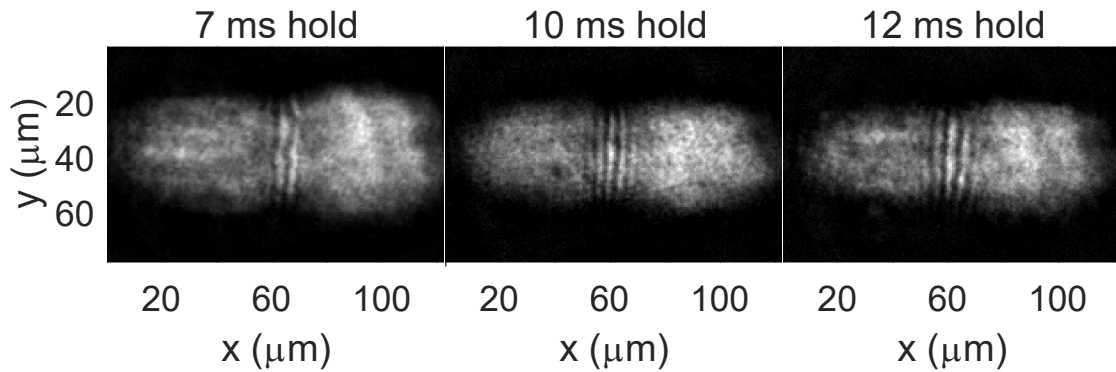


Figure 3.4: *In situ* vertical images of the BEC after 7 ms, 10 ms and 12 ms hold times following a 40 ms barrier ramp off time. Lines began to show the first signs of instability through snaking 7 ms after the removal of the barrier. Snaking of the solitons continued to be observed in this way for hold times up to 12 ms.

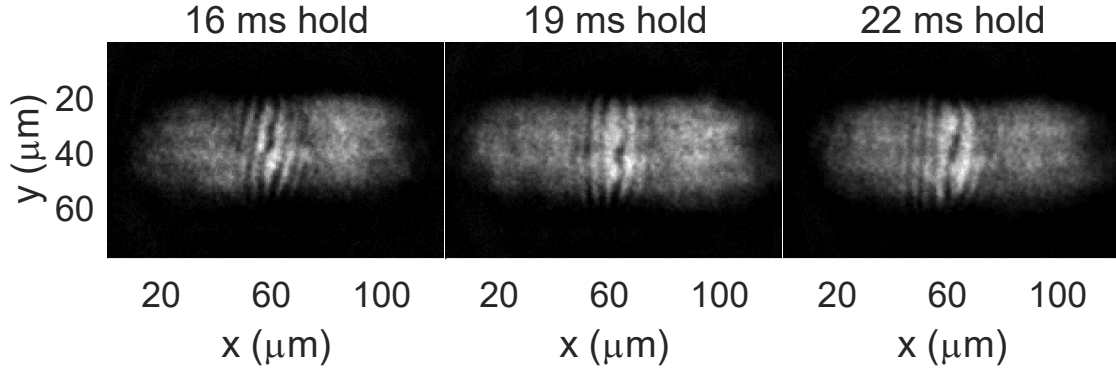


Figure 3.5: *In situ* vertical images of the BEC after 16 ms, 19 ms and 22 ms hold times following a 40 ms barrier ramp off time. Center solitons showed even more dramatic snaking with well-defined circular deformities resembling vortices appearing as the soliton decayed.

of soliton decay into vortices and sound waves via the snake instability. For hold times from this point to 22 ms, lines became increasingly less defined while localized deformities in the density profile resembling vortices began to appear in place of the decaying center soliton. This observation was usually only seen in the center soliton as the outer solitons became much less defined for these hold times.

However, the solitons observed for some experimental runs in this window showed solitons with almost no signs of decay as seen in Figure 3.6. The reasons for this were largely unclear. One of the commonalities of the experimental runs which showed these straight solitons was that atom number was significantly reduced. Exact atom numbers were not reliably extracted for these runs. However, the areas of the clouds imaged, as shown in Figure 3.6, were about 20% smaller than the areas of the clouds from Figure 3.5 suggesting a smaller atom number, and a corresponding reduction in atomic nonlinearity and tendency of the solitons to decay.

Soliton decay became increasingly evident for hold times of 30 ms to 50 ms hold times. By 30 ms hold times, solitons were still visible but had continued to dissipate

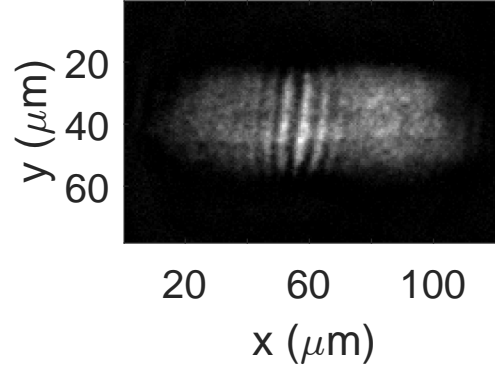


Figure 3.6: *In situ* vertical image of the BEC after 22 ms hold times following a 40 ms barrier ramp off time. Soliton lines in this run show relatively straight lines without strong evidence of the snake instability.

as both the center and outer solitons had become increasingly difficult to observe. In place of the decayed solitons were some defects resembling vortices. These point-like defects can be seen in each of the images of Figure 3.7. However, it is difficult to reliably say these defects are vortices because the *in situ* imaging resolution of these defects is particularly poor. After 45 ms to 50 ms hold times, solitons had almost completely decayed with only a couple soliton line fragments still observable in the images of Figure 3.7. However, it is unclear why more vortices are not visible for these hold times since each decayed line would be expected to produce a number of vortices similar to the simulations of [21]. Our hypothesis is that these BECs are both turbulent and not especially 2D. This combination of factors would allow vortices in the condensate to be imperfectly aligned perpendicular to the imaging plane in the third, z-dimension of the condensate. Because of the small margin of error required for *in situ* vortex imaging, it is easy to believe that bent or misaligned, non-perpendicular vortex lines would not be resolvable in our experiments.

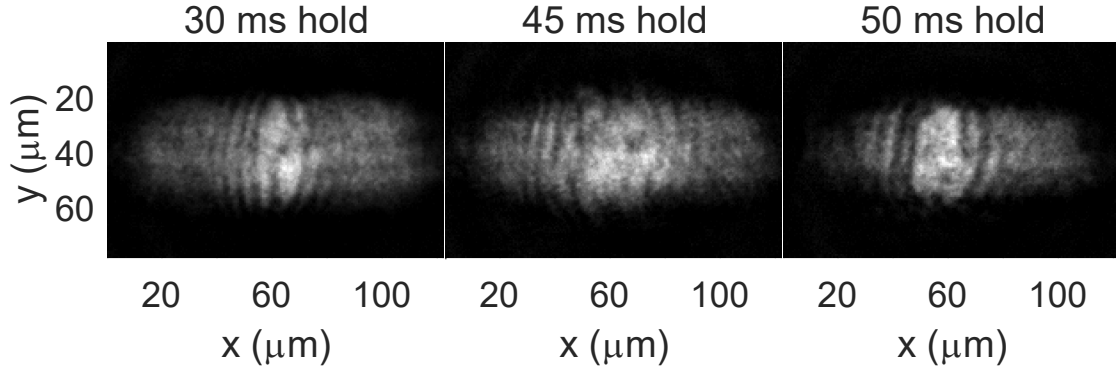


Figure 3.7: Vertical images of the BEC after 30 ms, 45 ms and 50 ms hold times following a 40 ms barrier ramp off time. Lines showed a continuation of decaying until nearly all the lines had decayed into line fragments or vortices.

### 3.4 Experimental results for short time scales: 13 ms barrier ramp

For the 13 ms barrier removal condition, the atoms had not yet started merging immediately after the barrier was removed. Instead, the merging of the clouds began to show signs of interference as they began to overlap after a 7 ms hold time. The number of fringes grew as the clouds continued to merge over 7 ms to 10 ms hold times as can be seen in Figures 3.8. Finally, around the 13 ms hold time, the average number of fringes observed stopped increasing and plateaued around an average number of 7.2.

From about 15 ms to 19 ms hold times, the lines began to show evidence of soliton-like behaviour and the first signs of decay through the snake instability similar to the 7 ms to 15 ms hold time window of the 40 ms ramp experiment above. Around hold times of 15 ms, lines in the BEC began to show some curvature as seen in Figure 3.9. While it is difficult to see if vortices were formed due to this initial snaking of the solitons, tracing the curving line shows significant variations in its soliton depth. Finally, by hold times of around 20 ms, the snaking of the center

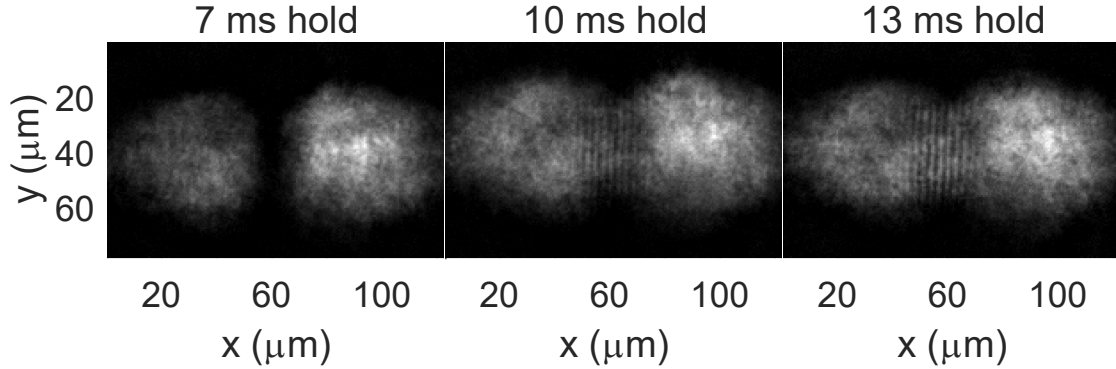


Figure 3.8: *In situ* vertical images of the BEC after 7 ms, 10 ms and 13 ms hold times following a 13 ms barrier ramp off time. Hold times of 7 ms captured the two clouds right before clear interference lines began to form. By 10 ms holds, lines had clearly formed at the intersection of the two clouds. 13 ms holds marked the point at which the system reached its maximum number of fringes which was typically between 7 and 9 lines.

lines had resulted in entirely fragmenting them with some of the remains looking somewhat like vortices.

For hold times of 21 ms to 25 ms, soliton lines became especially difficult to see. This was in part to the continuation of the decay of the centermost solitons. This decay led to the observation of both fragmentation of the center line as well as the formation of some point-like defects which strongly resembled vortex cores. These effects can be seen in Figure 3.10.

For hold times of 30 ms to 38 ms, solitons were no longer observable in the center of the merging BECs. Instead, fragments of what were solitons and vortex-like defects had been left in their place. For the entirety of this window, solitons continued to move outward from the center showing some curvature, but largely maintaining their structure. By hold times of 30 ms, a bright center strip about 4 times the width of a soliton appeared in the merged BEC as seen in Figures 3.11. In this bright center strip, snaking and possible vortex formation became even more

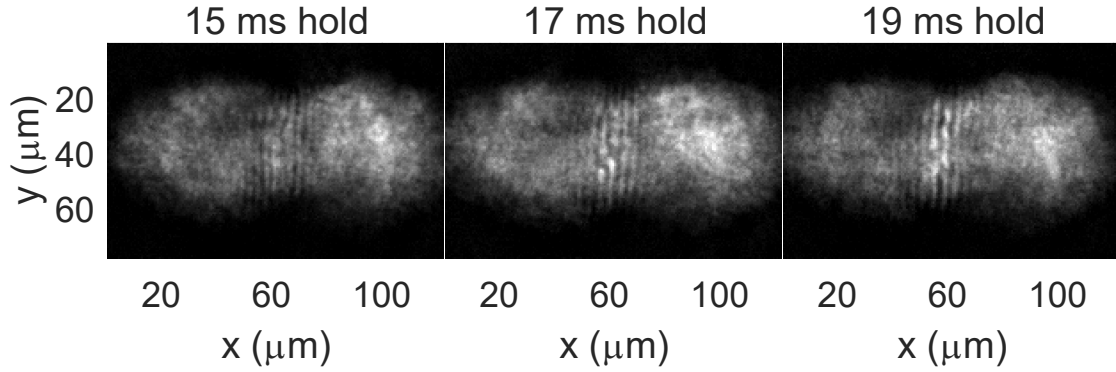


Figure 3.9: *In situ* vertical images of the BEC after 15 ms, 17 ms and 19 ms hold times following a 13 ms barrier ramp off time. Hold times of 15 ms captured the first evidence of curvature of the lines which is evidence of the soliton-like behaviour of snaking. Along with additional curvature of the lines, density nonuniformities in the lines at by 19 ms holds showed more evidence of the soliton decay to vortices via the snake instability.

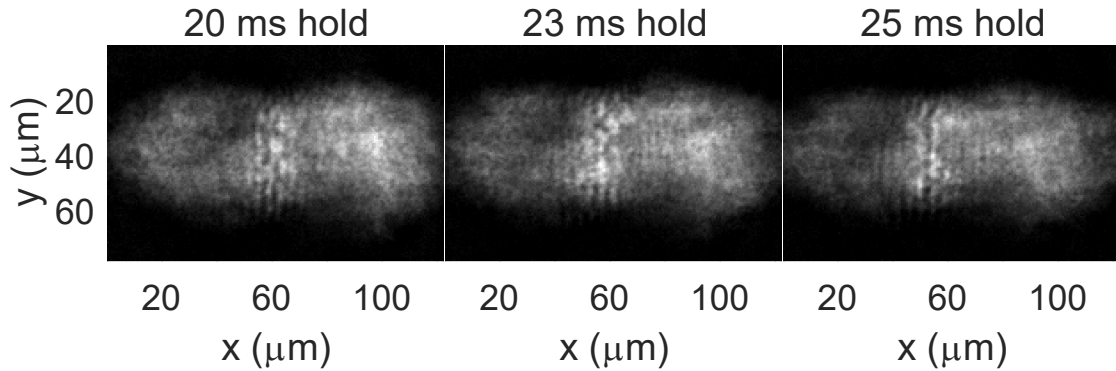


Figure 3.10: *In situ* vertical images of the BEC after 20 ms, 23 ms and 25 ms hold times following a 13 ms barrier ramp off time. In this timing window, decay of the soliton lines through the snake instability left point-like defects resembling vortex cores along with fragments of the lines scattered about the center of the BEC.

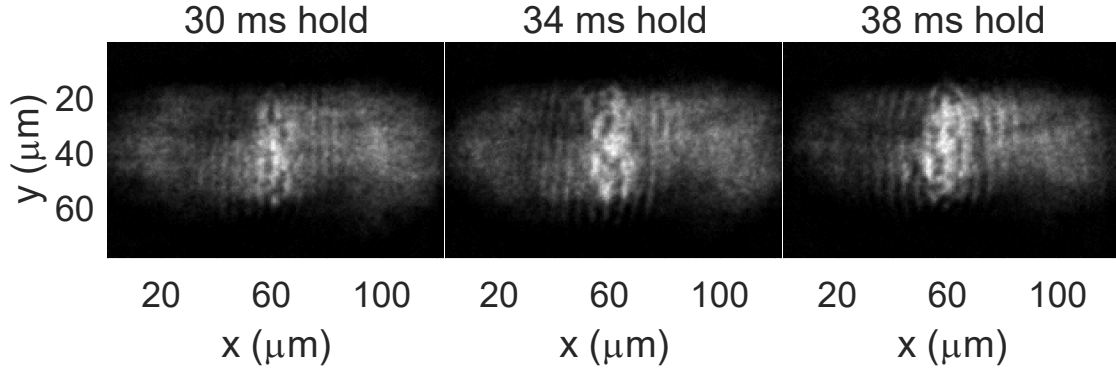


Figure 3.11: *In situ* vertical images of the BEC after 30 ms, 34 ms and 38 ms hold times following a 13 ms barrier ramp off time. In this window of hold times, a bright center at the merging center of the BECs began to appear. Additionally, defects resembling vortex cores became prevalent in this bright regions for each of the hold times.

visible.

For hold times of 40 ms to 60 ms, the solitons continued their outward movement until they ultimately dissipated into vortices as shown in Figure 3.12. For 40 ms hold times, solitons can still be identified along with what are likely vortex cores around the bright center portion of the merged BEC. After 50 ms and 60 ms hold times, solitons had almost entirely dissipated, particularly on the left half of the BEC. Defects in the left half of the 60 ms hold time trial show what are likely vortices which have formed after the dissipation of the solitons.

While the two different ramp times showed a number of similarities including the general time scales marking the formation, behaviour and decay of the solitons, several aspects of the two data sets showed unique characteristics. For the 13 ms ramp time, the bright center strip in the BEC became prominent from about 30 ms to 50 ms hold times. This feature was especially noteworthy due to the significant evidence of snaking and vortex formation observed within this region. However, this

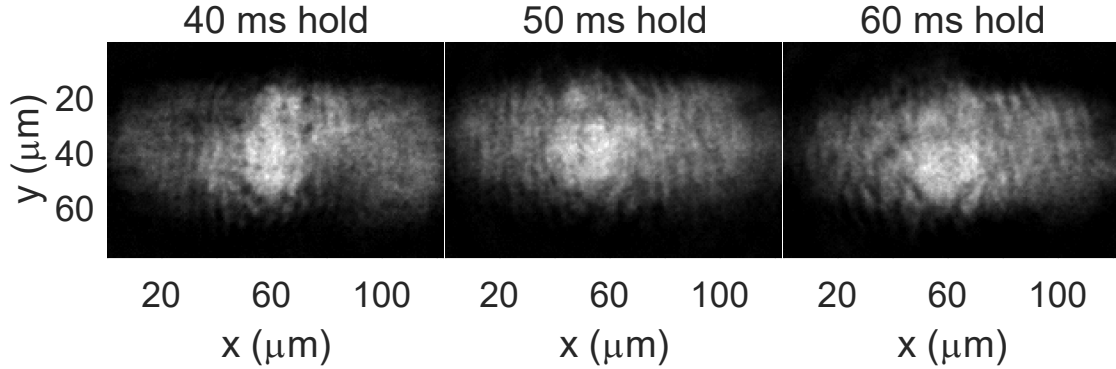


Figure 3.12: *In situ* vertical images of the BEC after 40 ms, 50 ms and 60 ms hold times following a 13 ms barrier ramp off time. In this window of hold times, solitons continue to dissipate often leaving behind circular defects in the BEC which are likely vortices.

feature was not nearly as defined for many of the images of the 40 ms ramp experiment. Additionally, the number of fringe lines produced for the two experiments varied greatly with each other over the initial merging of the BECs. The average number of fringes counted in the initial window of the 13 ms ramp experiment was about 7 while the average number for the 40 ms experiment was only about 4 over each respective data set.

### 3.5 Experimental results for long time scales

Following this initial set of timings was a longer timing window in which much of the additional energy in the BEC was damped out while vortices formed from the decayed solitons became more clearly resolved. This timing window was generally examined from 100 to 2200 ms hold times for each of the 13 and 40 ms ramp time experiments. These 13 and 40 ms data sets can be seen in Figures 3.13 and 3.14, respectively.

In each of these sets, the BEC began in a turbulent state containing excess en-



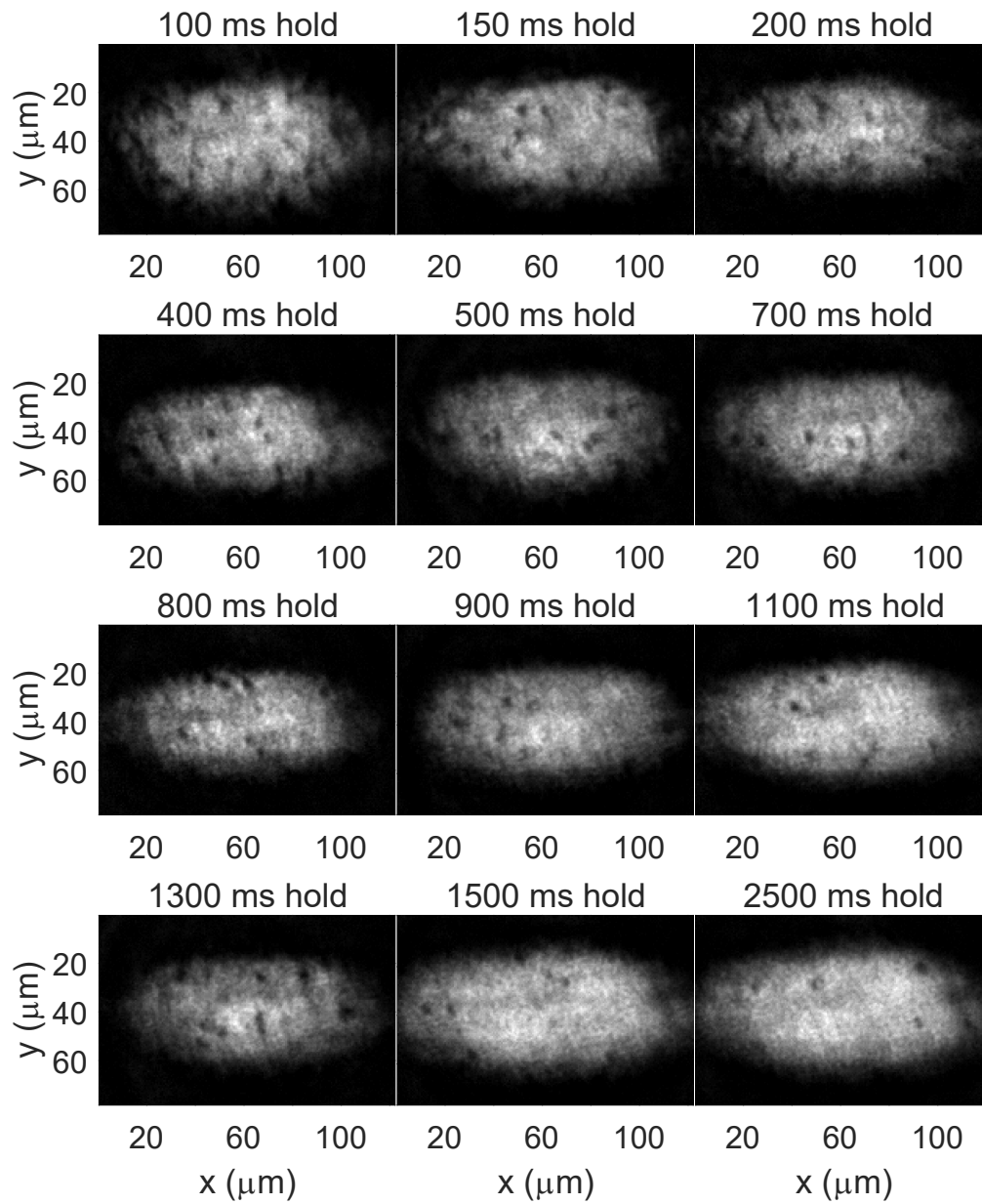


Figure 3.13: *In situ* vertical images of the BEC after hold times of 100 ms to 2500 ms after a barrier ramp off time of 13 ms. Images show turbulent BECs with numerous vortices for hold times of 100 ms to 200 ms. Generally, vortex number steadily declines as hold time increases from this initial state.

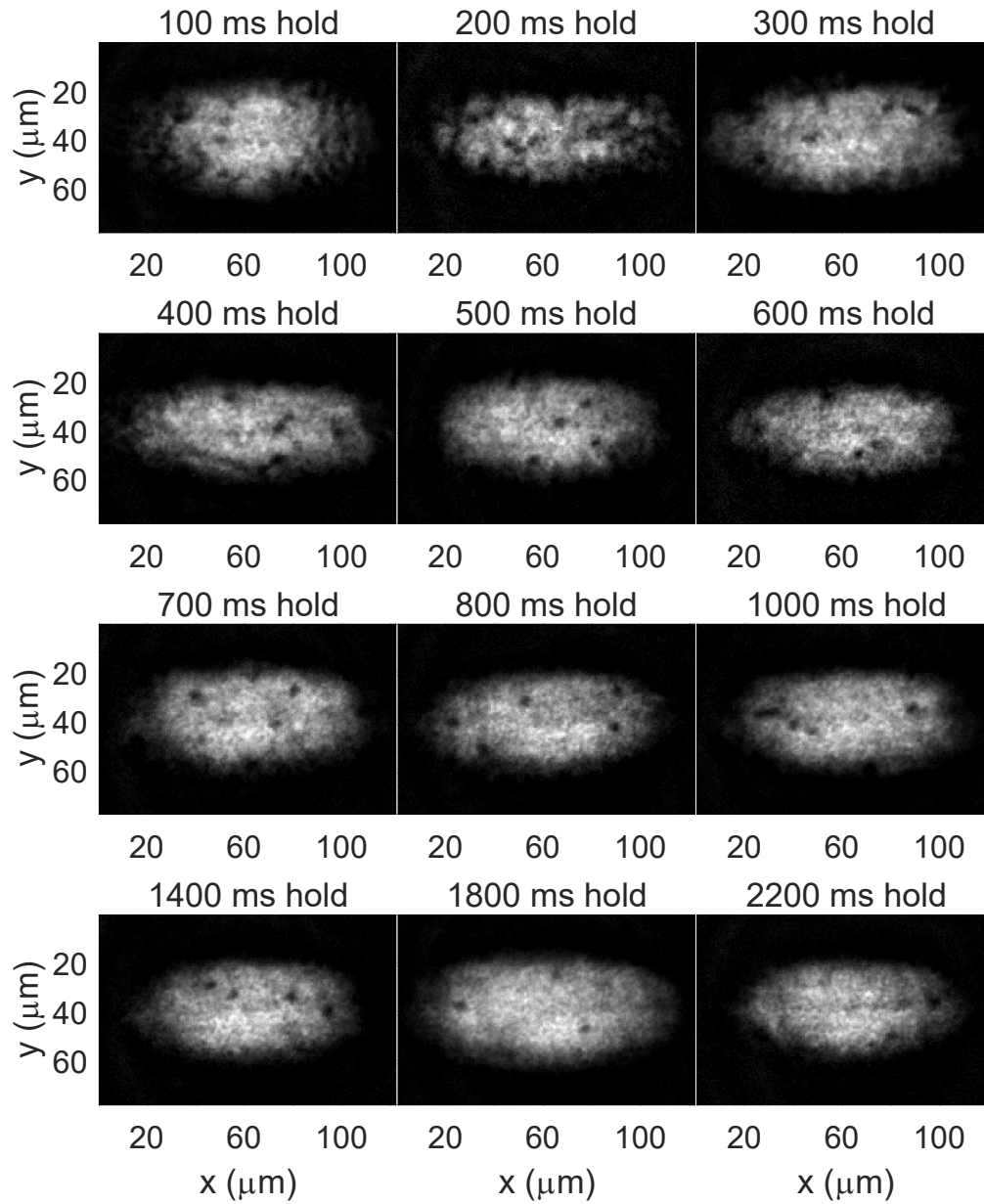


Figure 3.14: *In situ* vertical images of the BEC after hold times of 100 ms to 2200 ms after a barrier ramp off time of 40 ms. Images show turbulent BECs with numerous vortices for hold times of 100 ms to 200 ms. Vortex number steadily declines as hold time increases from this initial state.

ergy not in the form of vortices. This can largely be seen for hold times between 100 and 400 ms where the BEC shape was asymmetric and deviated from the expected Thomas-Fermi profile of the ground-state BEC in the harmonic trap. These aspects of the shape largely correspond to the excitation of breathing modes in the system. With the presence of these excitations as well as density fluctuation (acoustic energy), vortices became more difficult to reliably identify and count. However, the number of vortices that are identifiable in some of these images, such as the 100 ms hold time image of Figure 3.13 and the 200 ms hold time image of Figure 3.14, show that the decay of the solitons initially imparted a significant number of vortices into the condensate. This provides evidence towards the efficacy in using soliton decay to generate significant 2D turbulent BEC states.

Around the 400 ms hold time mark, asymmetries in the BEC profile and thermal background atoms became less evident. Because the trap was held near its evaporation point, it was expected that energetic thermal atoms would evaporate from the trap as the cloud came to an equilibrium after the merger. This then left a BEC with a large enough condensate fraction for clear vortex detection. As mentioned before, the vortices stirred up from the decayed solitons were also likely misaligned to the orientation to the 2D plane of the BEC. By around 400 ms hold times, these misaligned vortex lines damped to stable lower energy states as vortices oriented perpendicular to the 2D imaging plane.

Hold times from 400 ms onward showed a general trend of vortex dissipation. This was another expected result as freely evolving vortices will annihilate when two oppositely charged vortices come into contact with each other or when a vortex gets too close to the edge of the BEC. Because of the vortex-antivortex annihilation mechanism, the more densely vortices of a random distribution populate a BEC, the more quickly they will annihilate each other. Additionally, this annihilation mechanism is dependent on their proximity to each other relative to the BEC healing length. Larger healing lengths for given vortex-antivortex separations lead to faster

annihilation rates.

Another observation regarding vortex numbers in these experiments was the increase of vortices counted for the 13 ms ramp compared to the 40 ms ramp. This was again an expected result because the vortices formed as a result of soliton decay and the average number of lines formed for the 13 ms ramp experiment (7.2 lines) was almost double that of the 40 ms ramp (4.0 lines). For the 13 ms ramp, an average of 7.8 vortices were identified per trial as described below. However, only an average of 5.3 vortices were identified per trial in the 40 ms ramp experiment.

In order to count these vortices as reliably as possible, vortex numbers were only counted for trials with hold times between 300 ms and 500 ms. This window was chosen for two main reasons. First, vortices were very difficult to identify for shorter hold times in both experimental data sets likely for the reasons states above. Waiting until the 300 ms hold time threshold allowed for a more consistent and reliable vortex counting procedure. Finally, trials beyond the 500 ms hold time threshold were not used for this comparison because of the likelihood of more significant vortex loss for long hold times. For this reason, these two averages for vortices produced from the solitons are likely significant underestimates of the actual number of vortices produced. However, these numbers do help give an idea for the number of vortices initially produced as well as help identify the direct correlation between the number of soliton lines formed and the number of vortices produced upon their decay.

### **3.6 Single-shot measurements of vortex-handedness**

During experimental runs, it became evident that soliton decay could happen more rapidly for cases when vortices were spontaneously formed during evaporation in either of the two initial BECs. Vortices interacting with the system in this way can be seen in Figure 3.15. In this pair of images, the 45 ms barrier ramp off time was identical. In Figure 3.15a, the lines look similarly straight when compared to the trials of the 40 ms ramp time discussed in Section 3.3. However, in Figure 3.15b,

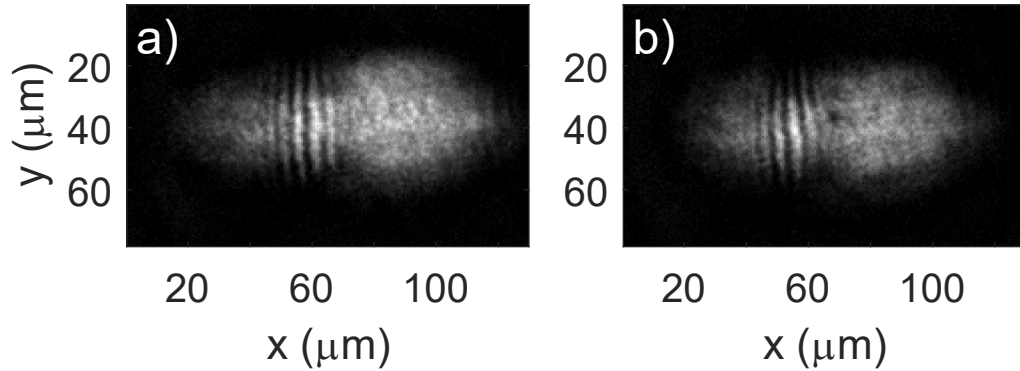


Figure 3.15: *In situ* vertical images of soliton lines with, a), and without, b), a vortex core in proximity. Soliton lines in a) are straight and showing very little curvature at this hold time (about 5 ms). However, the solitons in b) show curvature similar to simulation studies in [13] and shown in Figure 3.16.

a single vortex is clearly visible near the rightmost soliton. Because of the phase gradient around this vortex core, a curvature is also clearly evident in the rightmost soliton line when compared to the image of Figure 3.15a.

However, these images also opened up the possibility of making vortex circular direction measurements using the solitons generated from merging the two condensates. Because of the  $2\pi$  phase gradient around a charge 1 vortex and the  $\pi$  phase shift across a dark-soliton, the interaction of these two defects results in the soliton phase being non-uniformly offset when in close proximity to the vortex. The result of this offset is that the soliton should bend in the direction of rotation of the vortex it is near. Thus, to further investigate this phenomena, vortices needed to be formed near but independent of the soliton lines. To accomplish this, evaporation sequences were purposely shortened to greatly increase the likelihood of vortices spontaneously forming in either BEC as described in [8]. After many trials, several examples of this expected vortex-soliton interaction were seen.

Figure 3.17 shows examples of the leftmost solitons being bent in either direction when in proximity to a vortex core. For 3.17a, the counterclockwise bending means

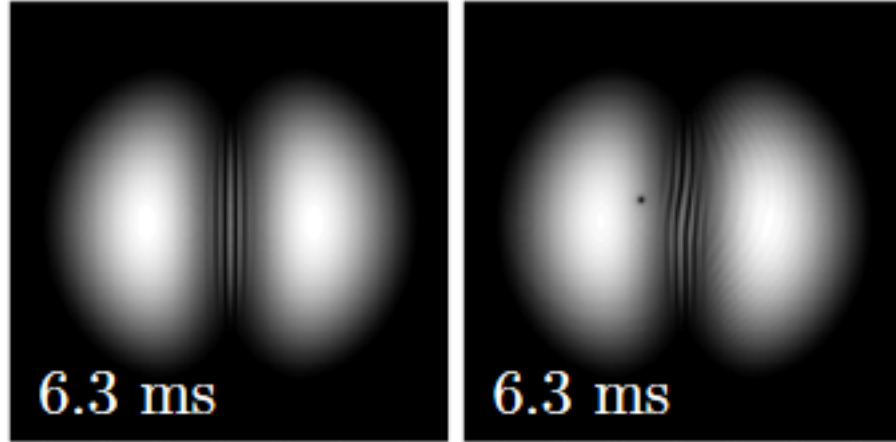


Figure 3.16: Simulations showing dynamically similar soliton line bending in the presence of a vortex at a comparable hold time to the images from Figure 3.15. Simulation results taken from Kali Wilson, PhD Dissertation, Figure 9.11 [13].

the fluid around the vortex is also flowing in the counterclockwise direction which means, by the right hand rule, the circulation is pointing out of the page. For 3.17b, the clockwise bending means the vortex circulation is pointing into the page.

Finally, Figure 3.18 shows two examples of vortices formed in similar ways showing almost no interaction with the soliton lines. Figure 3.18a shows an image of vortices present in the BEC with soliton lines. It is expected in this situation that the vortices are simply too far away from the lines to have significant bending. In Figure 3.18b, two vortices very near the solitons in the right half of the BEC can be seen with almost no bending of the soliton lines. The likely cause of this is that these vortices are a vortex dipole pair. When close enough to each other, the net phase gradient surrounding the pair is zero, thus resulting in no observable bending of the soliton lines.

While the effect of this phenomenon was not quantitatively examined in the study of cascading effects in decay of a soliton train, it interestingly demonstrates a method of measuring the handedness of a vortex with a single image, something that

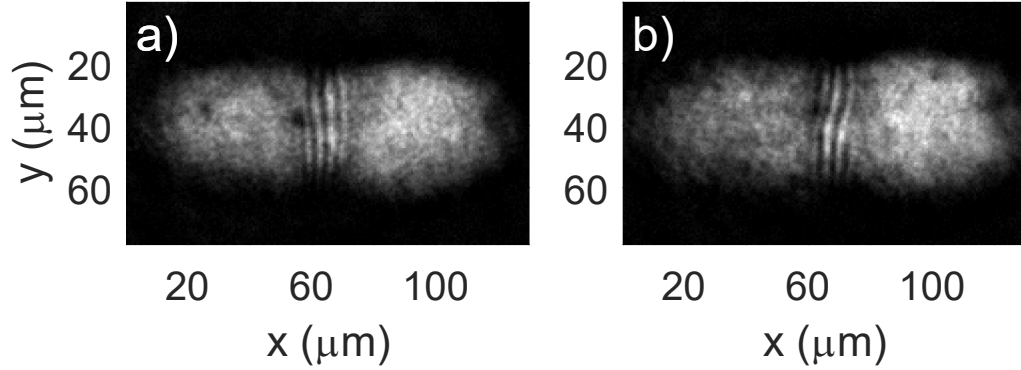


Figure 3.17: *In situ* images of vortices formed spontaneously in the left BEC before merging interacting and bending soliton lines during the BEC merging step with bending direction measuring the handedness of the vortex.

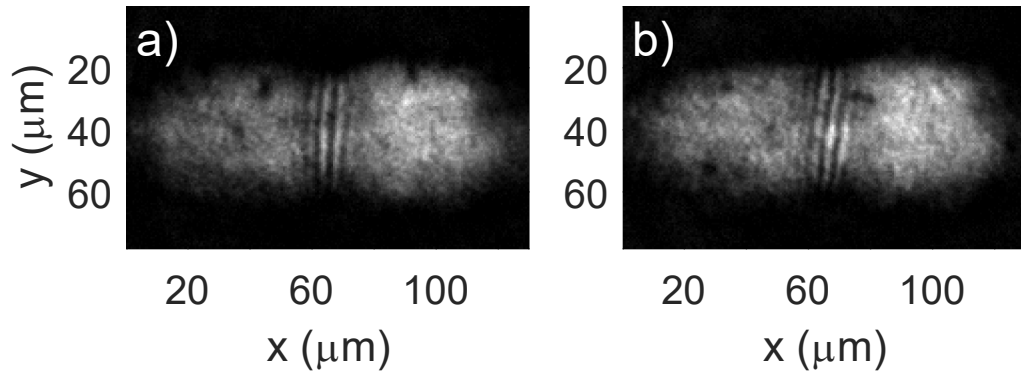


Figure 3.18: *In situ* images of little to no bending of solitons with spontaneously formed vortices present in the BECs. a) Image of vortices too distant from the soliton lines to significantly bend the lines. b) Image of what is likely a vortex pair of opposite circulations which effectively cancel each other's bending of the solitons.

has been historically difficult to accomplish. The bending of solitons or dark fringes could thereby be incorporated into vortex circulation detection such as examined in Section 5.3 in a different context.

### 3.7 Conclusion

This set of experiments allowed for the creation of a 1D array of solitons, the observation of the dynamics of the solitons from formation to decay, and a study of the vorticity stirred up upon the decay of the solitons. First, the experiments showed the formation of a 1D array of soliton lines from an atomic interference pattern formed from two self-coherent merging BECs. This merging was performed for two different durations of merging times that allowed for further investigation of the soliton formation and for the effect of soliton number on the decay of the array of solitons. This aspect of the decay of the array was important for the collection of experimental data which could be compared to the simulation study from [21] which suggested a nonlinear cascading effect to be a prominent feature in the decay of the soliton array.

In addition to providing a rigorous sampling of the soliton dynamics, these experiments also provided evidence of vortex-soliton interaction which could be useful for circulation measurements of vortices in the future. They also provided further evidence of the efficacy for efficiently generating turbulent BECs through the collision of BECs. This demonstration more generally opens up a means of studying turbulence generation in colliding air or other fluid masses from a quantum-mechanical foundation.

Finally, with the ability to image *in situ* vortices and solitons, the data set had a number of trials which dramatically captured the curling of a soliton during its decay into vortices via the snake instability as again illustrated in the BEC image of Figure 3.19. Unfortunately, even with the ability to perform *in situ* imaging, the imaging procedure is only capable of single-shot imaging due to its destructive pumping stage



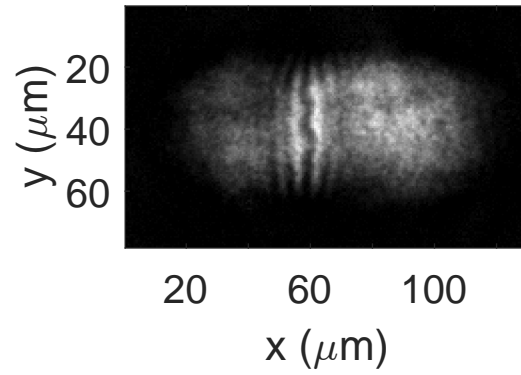


Figure 3.19: Center soliton with particularly dramatic snaking.

required for high resolution imaging. Ideally, multi-shot *in situ* imaging of the same BEC would provide more complete access to the dynamics of the decay of a soliton train.

## Chapter 4

### Forced Damping of a Superfluid Gas with a 1D Optical Lattice

#### 4.1 Introduction

Many techniques have been developed in the efforts to generate turbulent flows in a BEC. Spontaneous vortex production [8], the merging of distinct BECs [7], BEC flow around a barrier [25] and many other techniques have been studied in the context of vortex production, and are linked to turbulence generation mechanisms. However, while many efforts have been oriented towards generating consistently turbulent quantum fluids, little effort has been put into techniques guaranteeing a vortex-free BEC and more specifically, removing vortices from a turbulent BEC. In addition, some recently proposed vortex dynamics experiments, such as investigating Snell's law for a vortex dipole [26], require precisely known BEC initial conditions prior to the introduction of vortices deterministically, particularly when single-shot imaging and deterministic dynamics are required.

In classical fluid dynamics a fundamental characteristic of turbulence is energy transport through characteristic length scales, to eventually be dissipated. If energy is not continually input into the system, viscous forces quickly remove excess energy from the fluid, transitioning the turbulent flow back into laminar flow. For Bose-Einstein condensates, a component of the gas exists as a thermal background which can provide a dampening source to the system. Minimizing this thermal component is often an essential aspect in probing the purely superfluid dynamics of topological defects in BECs. However, as the atomic sample gets colder and purer, the dampening force associated with the thermal component weakens resulting in exceedingly long hold times before a BEC is dampened to a laminar flow ground

state. These long hold times are often undesirable as experimental heating and loss mechanisms found in any BEC machine will degrade the BEC quality. To solve this problem, we have demonstrated the efficacy of a new technique to quickly, efficiently and consistently dampen BECs into vortex-free states with the use of a 1D optical lattice. We refer to this new technique described in this chapter as a “vortex comb” that efficiently “combs” vortices out of the BEC.

Vortex dissipation in a 2D BEC often occurs through one of two mechanisms, annihilation upon contact with an equal and oppositely charged vortex or loss near the edge of a BEC [27, 28, 29]. In the case of the vortex comb, the optical lattice segments the BEC in such a way that any given location of the BEC will be near an edge. Restricting fluid flow in this way leads to vortex annihilation for each vortex that was initially trapped in the BEC. The creation of the vortex comb is somewhat similar to a superconductor vortex broom that was recently demonstrated in which a laser was swept over the superconductor to move vortices out of a target area of the superconductor [30].

## 4.2 Experimental set-up

The 1D optical lattice used in this experiment was created by splitting a blue-detuned laser with a 50/50 non-polarizing beam splitter and interfering the beam with itself at the BEC. The beam source for the lattice was a Verdi V-6 532 nm 6.5 W laser. This laser functions primarily as the “plug” for the magnetic quadrupole trap which enabled efficient RF-cooling by limiting Majorana losses due to spin flip events near the center of the magnetic trap. However, implementing an AOM in its beam path as shown in Figure 4.1 allowed for up to 1.5 W of 532 nm light to be deflected and picked-off for the purpose of creating this optical lattice. The zero-order light through the AOM was reshaped and aligned to continue functioning as the optical plug. The deflected first order light out of the AOM was found to have some divergence in its vertical profile and a weaker horizontal divergence. To

correct this, a 1D cylindrical lens telescope reshaped the vertical waist and degree of divergence to be equivalent to the horizontal profile of the beam. Then, a 1:1 telescope was implemented to correct the small, symmetric divergence of the beam and ensure collimated interfering beams at the science cell.

Initially, the beam-steering PZTs set the 0<sup>th</sup> order plug beam to the center of the magnetic quadrupole trap for optimal performance during RF-evaporation. As linear ramps moved the magnetic field away from the optical trapping beam, a step which transferred the coldest atoms in the cloud from the quadrupole trap to the optical dipole trap, the PZT voltages were also linearly ramped to keep the plug beam at the center of the quadrupole trap as it moved. Once transfer to the optical dipole trap was complete, a shutter was used to ensure that the displaced plug beam did not contribute to the proceeding BEC evaporation steps. However, to implement the optical lattice, the flip mirror shutter needed to be reopened. To ensure that the 0<sup>th</sup> order light from the AOM did not alter the trapping potentials at the BEC while using the optical lattice, the PZTs aligned the zero-order light into a pick-off mirror that dumped the light well before entering the science cell as seen in Figure 4.1a. The deflection efficiency of the AOM was also optimized at this beam angle allowing for up to 1.5 W of light to be deflected into the 1<sup>st</sup> order mode of the AOM for creation of the optical lattice.

To create interference at the BEC as depicted in Figure 4.1, the reflected arm of the beam splitter was aligned directly onto the atomic cloud. The second arm (transmitted arm) was reflected by a mirror towards the atomic cloud after a short distance beyond the beam splitter. The beams overlapped and interfered at the atom cloud with equal powers and polarizations at about a 9-degree angle.

### 4.3 Lattice Properties

The periodicity of the resulting interference fringes was about 3.4  $\mu\text{m}$  and was measured using three different methods. The first method was to image the lattice

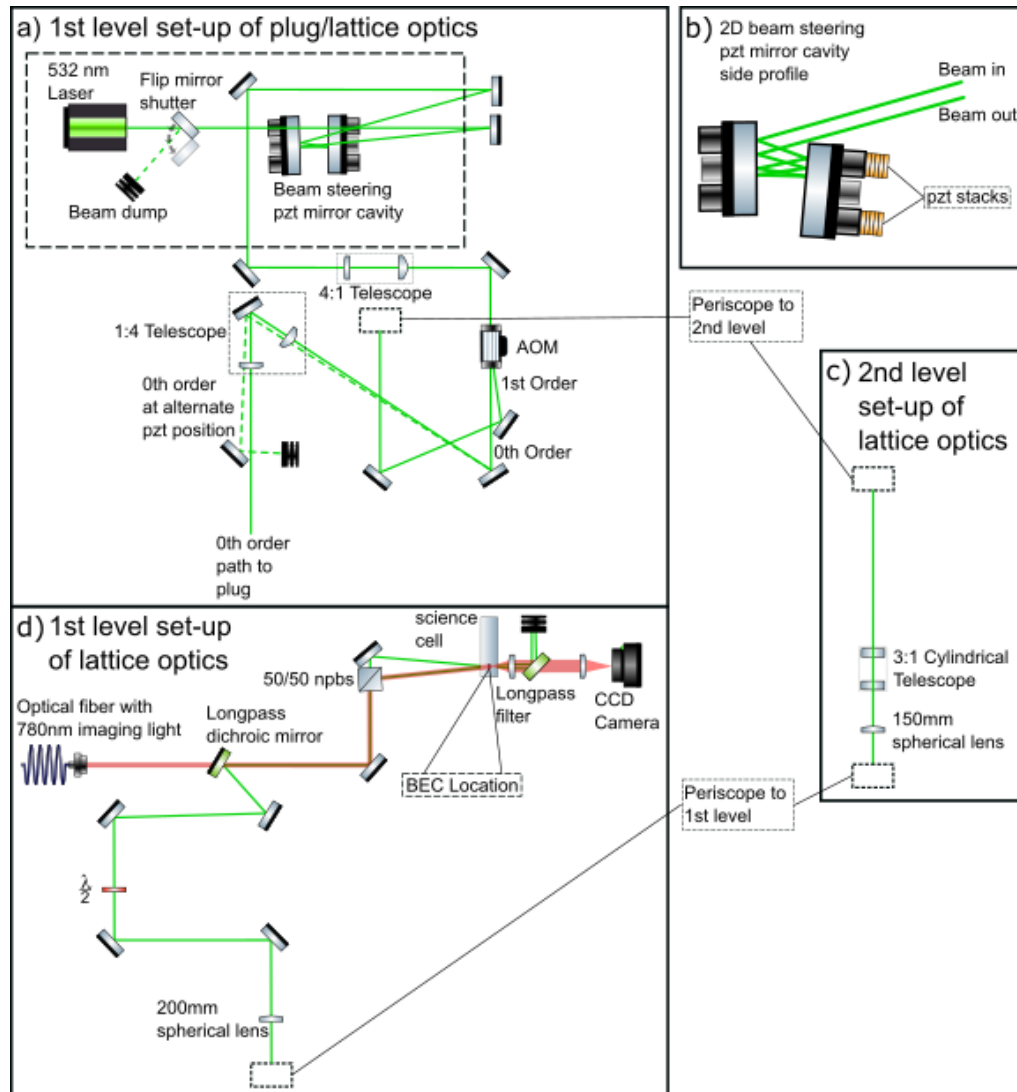


Figure 4.1: a) Design of initial optical set-up to control beam direction and separate plug and lattice beams. b) Side profile of Piezo-electric transducer (PZT) controlled mirror mount reflective cavity. c) Second level of the set-up to transport the beam across the optical table and reshape and re-collimate the beam. d) Final section of optical set-up to set optimal beam polarization for greatest lattice fringe interference contrast and produce optical lattice. BEC side-profile imaging beam combined with lattice beam at dichroic mirror.

directly onto the side-profile CCD camera by simply removing the imaging system filter in part d) of Figure 4.1. The result can be seen in Figure 4.2 and revealed a periodicity of  $3.51 \mu\text{m}$ . The second method was to measure the period of peaks formed due to the atomic response to the optical lattice. This response is clearly visible, especially at suitably high optical powers in the optical lattice, as seen in Figure 4.3. These fringes in these images contained a periodicity of  $3.41 \mu\text{m}$ . Finally, a third measurement of the expected periodicity was calculated by first measuring the beam angle of the interfering beams relative to each other at the atomic sample. With an angle of 9.41-degrees and a wavelength of 532nm, the calculated fringe spacing was  $3.25 \mu\text{m}$ .

The interfering beam diameters of 0.85 mm were wide relative to the typical BEC x and y-direction Thomas-Fermi radii of  $80 \mu\text{m}$  and  $30 \mu\text{m}$ , respectively. Beams of this size were strategically chosen so that the intensity of the lattice would be nearly uniform across the BEC. This ensured approximately equal peak potentials over the lattice across the BEC while also avoiding an additional, vertical anti-trapping potential. The second purpose for this beam size was to ensure a large dynamic range of accessible intensities for the lattice. This beam diameter, with the laser operating at maximum power according to the AOM efficiency of the set-up found in part a of Figure 4.1, allowed for local lattice peak potentials of about 50 times the chemical potential of the BEC. Additionally, because the optical path length and number of optics for each of the two arms of the optical lattice were minimized, no significant vibrations in the fringe positions were measured below 15 Hz, the frequency limit set by the frame rate of the side-profile CCD camera.

The effects of the lattice on the BEC across this range of lattice intensities was observed directly through imaging the BEC perpendicular to the plane of the lattice as seen in Figure 4.3. The contrast of the periodic barriers across the BEC varied directly with the intensity of the optical lattice as seen in Table 4.1. As expected, almost no interaction was measured at low powers. As optical power in

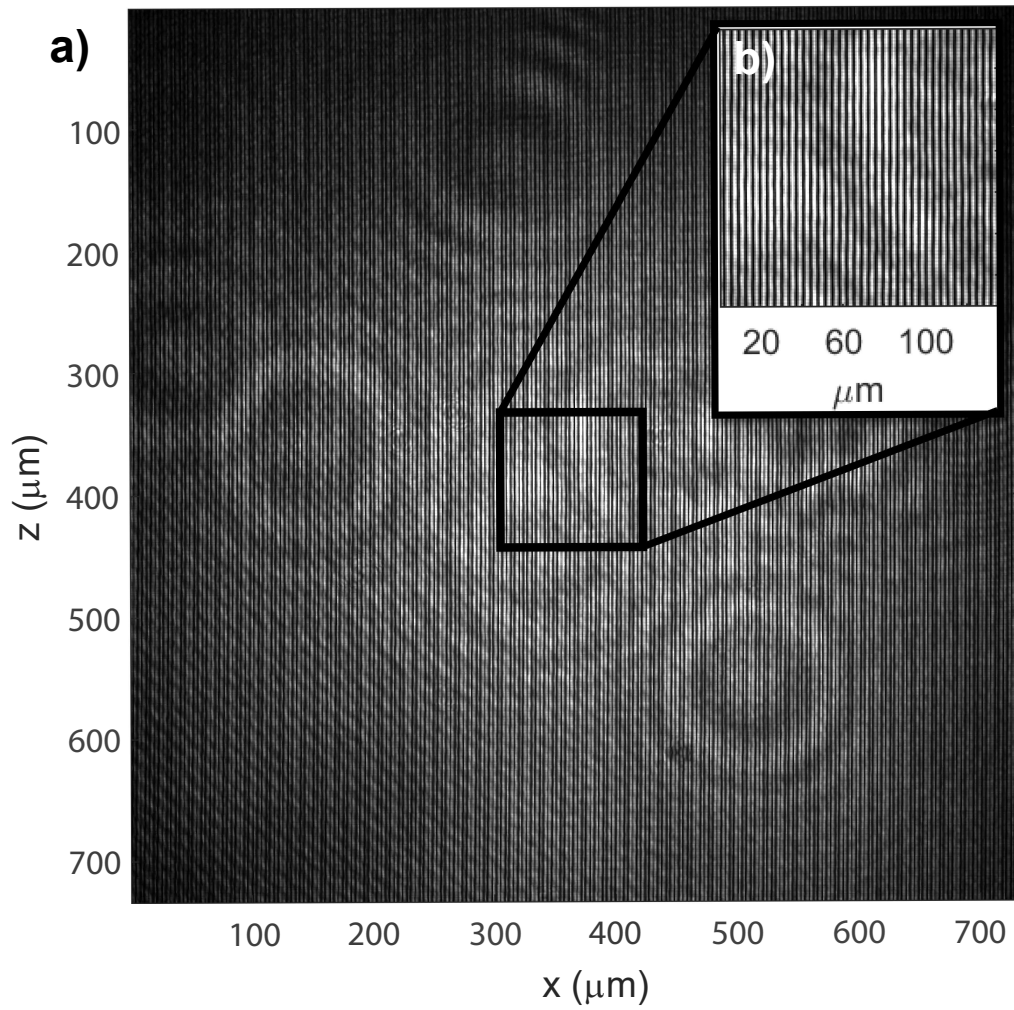


Figure 4.2: a) Side-profile image of optical lattice interference pattern at focal plane of atomic cloud. b) Zoomed in image of lattice at location of BEC (no atoms present in image).

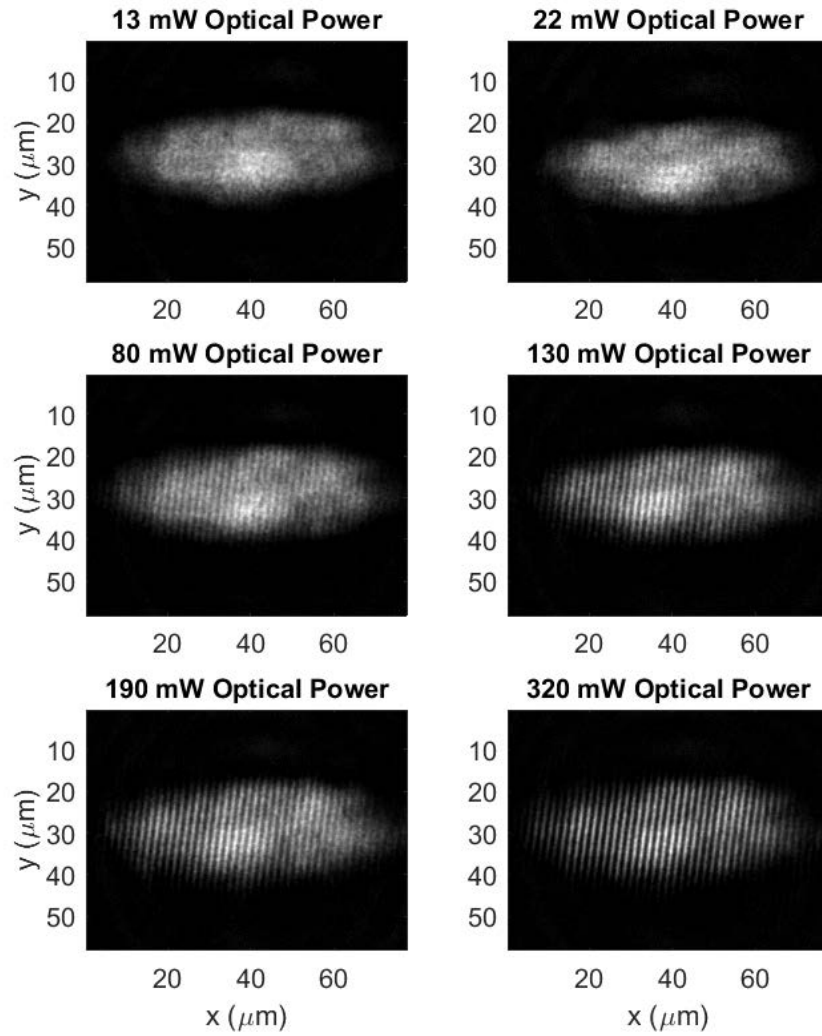


Figure 4.3: BEC imaged vertically *in situ* interacting with optical lattice at various optical powers; contrast of periodic fringes caused by the blue-detuned lattice improves as total optical power in the lattice increases. Calculated contrasts can be found in Table 4.1.



Optical Power (mW)	Contrast
0	0.00
13	0.04
22	0.06
80	0.12
130	0.23
190	0.30
320	0.55
1400	0.80

Table 4.1: Contrast of the lines formed in the BEC due to the optical lattice at varying powers.

the lattice increased, contrast improved dramatically as well. However, even at very high powers such as 1400 mW with peak potential amplitudes of about 50 times the chemical potential of the BEC, contrast remained imperfect. The exact source was not detected, some potential reasons include imperfections in the imaging system (e.g., out of focus, non-uniform imaging beam), unwanted optical diffraction and the presence of a significant thermal component in the BEC.

#### 4.4 Experimental procedure: Collecting baseline data

Because the presence of the optical lattice effectively acts as a comb to remove circulation and curl, and vortices, in order to dampen the turbulent cloud into the BEC ground state, we refer to the lattice as a “vortex comb.” To test the feasibility of this dampening method, we initially produced a turbulent BEC. The BEC was composed of about  $10^6$  atoms of  $^{87}\text{Rb}$  and was prepared in a trap with frequencies of  $(\omega_x, \omega_y, \omega_z) = 2\pi \times (2.8, 8.5, 38.5)$  Hz. A blue-detuned laser was focused near the center of the BEC with a beam waist of  $10 \mu\text{m}$ , forming a barrier in the BEC with

a peak potential of about  $\mu$ , where  $\mu$  is the BEC chemical potential. The BEC was then forced to flow in 4 small elliptical movements relative to the stationary barrier over 800 ms. The barrier was finally adiabatically removed over 0.5 s.

This “stirring” of the BEC produced a typical number of about 18 vortices when measured immediately after the removal of the barrier. Due to vortex-antivortex annihilation over time as the vortices propagated throughout the BEC, an average number of about 7 vortices remained clearly visible after a 4-second hold and imaging the BEC with some expansion. Data taken 2 s and 8 s after the removal of the barrier showed the expected trend that the rate of dampening of vortices decreased as the density of vortices within the BEC decreased. Results of the vortex number versus hold time can be found in Table 4.2.

Hold time (s)	Average # of vortices
0	18*
2	8
4	7
8	6

Table 4.2: Table of the average number of vortices counted after varying hold times upon completing the “stirring” and barrier removal steps to generate vortices. 18 vortices represents a typical number of vortices counted for the 5 images taken at this hold time.

A significant takeaway of these results was that vortices persisted in the BEC in this set-up over long hold times that were also associated with significant atom loss. Therefore, dampening through long hold times was not a viable strategy for reliably attaining a ground state BEC free of vortices. Example images typical for each of the conditions tested are found in Figure 4.4.

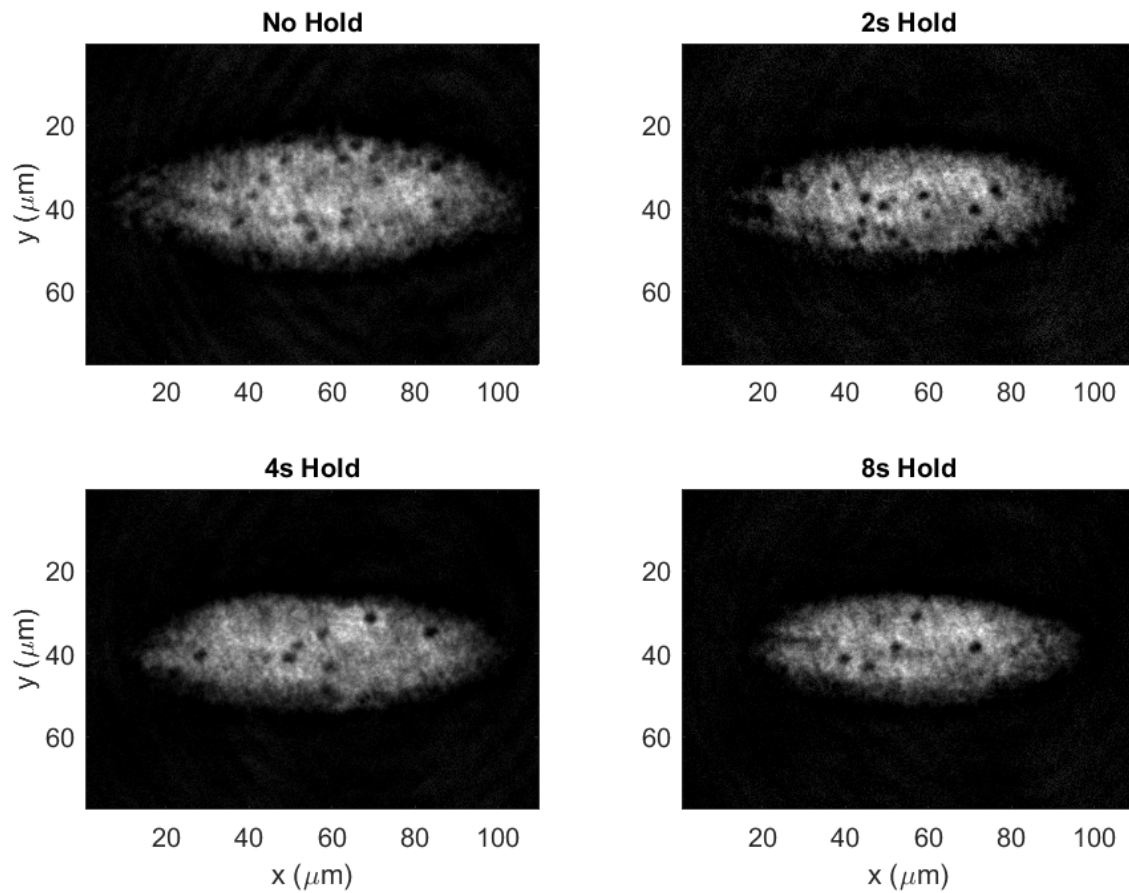


Figure 4.4: BECs representative of typical vortex counts for each of the hold times tested imaged after some expansion for more reliable vortex detection. Averages (or typical values) of the number of vortices seen over a number of trials can be seen in Table 4.2.

#### 4.5 Experimental procedure: Testing the vortex comb

To test the effectiveness of the vortex comb, we ran a set of experiments in which we actively used the 1D optical lattice to dampen a turbulent BEC. For this experiment, the effectiveness of the vortex comb was quantified by the average number of vortices in the BEC relative to the non-actively dampened, 4 s hold time base data set described in Section 4.4 and represented by the “No Lattice” label as follows.

The interaction of the lattice with the BEC was controlled over a 4-s period immediately following the removal of the vortex-inducing barrier from the BEC, in place of the 4-s hold time described above. The lattice was linearly ramped up to some maximum intensity over the first 2 s of the step before being linearly ramped off over the final 2 s of the step. Once the lattice was ramped off, the BEC was imaged with some expansion for the purpose of counting the vortices still in the BEC. Data were then collected for between ten and twenty trials for each peak lattice potential tested. Calculated peak potentials tested in this way varied from about 0.6 – 15 times the chemical potential or 13 – 320 mW of power in the lattice. For each trial, the number of vortices were counted as described in Section 4.6.

Figure 4.5 shows the fraction of trials of a given optical lattice power with a given number of vortices present. Figure 4.6 shows an example of two BECs imaged at the same moment of the experiment 4s after the stirring barrier had been removed. Figure 4.6a shows the BEC after the experimental procedure with no optical lattice sweep and therefore populated with a number of vortices. Figure 4.6b shows the BEC after the experimental procedure with the 130 mW optical lattice sweep which has removed all the vortices from the BEC.

As expected from the results of simulation data, with high enough optical intensities in the optical lattice, vortex number was consistently reduced to zero. This was the case for every trial of both the 340 mW and 190 mW experimental conditions. As we reduced the beam intensity, the fraction of vortices removed also

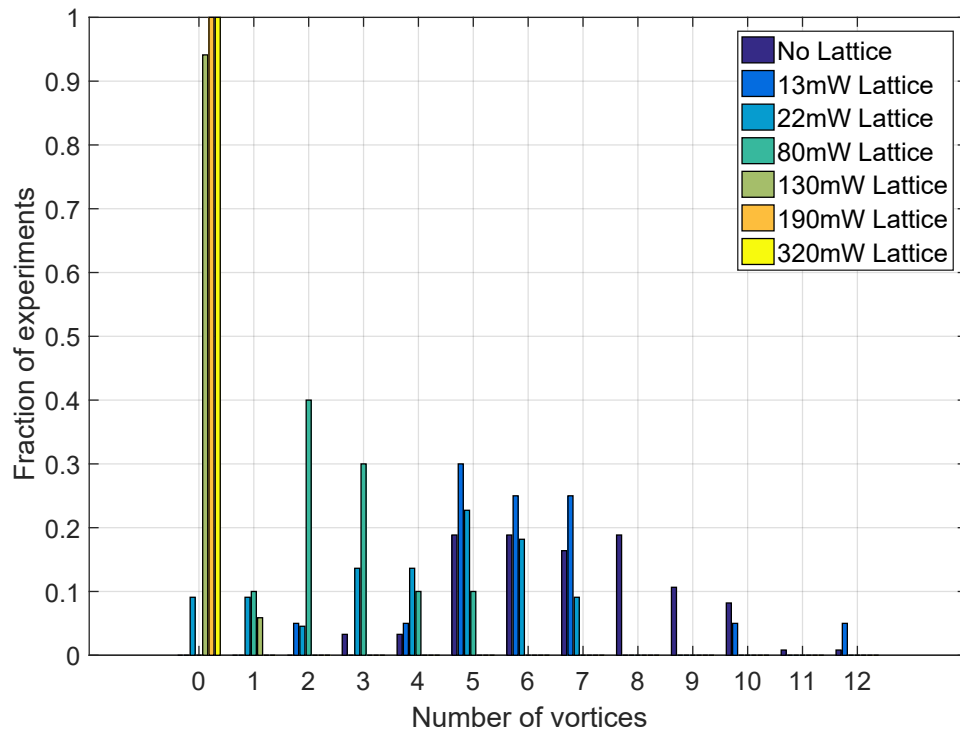


Figure 4.5: The number of vortices observed in each experimental trial were recorded and compiled. Data sets were collected for the cases of optical lattice powers of 13 mW, 22 mW, 80 mW, 130 mW, 190 mW, and 320 mW as well as a case for no lattice. The fraction of trials in a data set with an observed vortex number was plotted for each case.

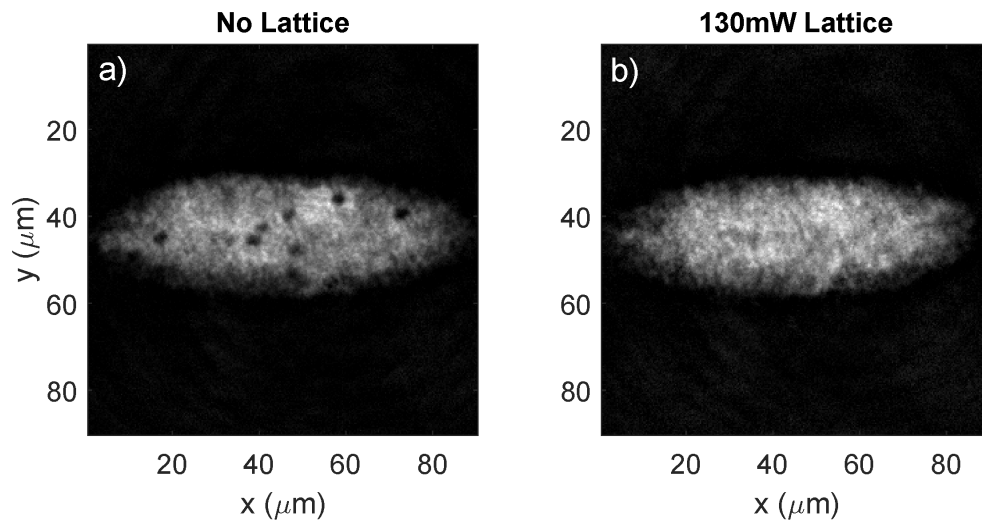


Figure 4.6: Example images of the BEC at the same time after stirring, with and without the vortex comb step. a) BEC image with clear vortices present after some expansion after 4 s hold as discussed previously. b) BEC image with no clear vortices present after some expansion after 4 s optical lattice ramp to maximum optical power of 130 mW.

Optical Power (mW)	Average # of vortices
No Lattice	6.93
13	6.06
22	4.00
80	2.21
130	0.06
190	0.00
320	0.00

Table 4.3: Average number of vortices counted per trial for each optical power data set.

decreased. For the 130 mW condition, a small number of the trials revealed a single vortex surviving the lattice “comb” process. Further reducing the power in the lattice resulted in average vortex numbers and vortex number variations which began to approach the non-dampened base condition with vortex number averages that can be seen in Table 4.3. For lattice potentials well below the chemical potential (13 mW) the lattice had little effect on the number of vortices observed after combing. As lattice potentials increased to roughly 8 times the chemical potential (190 mW), the number of vortices removed steadily increased until all vortices were consistently removed from the BEC. This removal of the vortices marked the transition of the BEC from a turbulent state back to a laminar state.

In addition to investigating the dependence of number of vortices removed on power in the optical lattice, we also investigated the effect of optical lattice ramp time in regards to vortex removal from the BEC. To test this, optical lattice ramp times of 2 s and 8 s were tested alongside the 4 s ramp discussed previously. Baseline data for the 2 s and 8 s hold times with no optical lattice were collected and are listed in Table 4.2. Data sets were also collected using the vortex comb procedure

with an optical power of 130 mW at the comparable 2 s and 8 s ramp times. The results of these two additional optical ramp times revealed some correlation between ramp time and the number of vortices removed. The data in Figure 4.7 show that shorter interaction times (2 s ramps) were less likely to successfully remove all of the vortices when compared to longer interaction times (8 s ramps) at identical optical lattice powers.

Comparing Figures 4.5 and 4.7, it is clear that optical power much more dramatically affected the removal of vortices than did length of interaction time. For example, decreasing the interaction time of the optical lattice with the BEC by one-half still removed all the vortices from the BEC more than half of the time. Comparatively, decreasing the optical power by less than one-half (from 130 mW to 80 mW) resulted in an average number of vortices of 2.21 and had no results in which no vortices remained in the BEC after the combing process.

#### 4.6 Experimental procedure: Counting the data

Several steps were taken to make the data as consistent and reliable as possible. First, images were taken after some expansion. With *in situ* imaging, vortices were often visible; but, if vortices were not perfectly aligned perpendicular to the imaging system, their visibility began to degrade. Expanded vortices had large enough cores to offset most issues with vortex direction misalignment. Expansion imaging also enabled shot-to-shot correction of camera focus position as magnetic drift caused the vertical trapping center to drift slowly over the course of a day. Expansion quadrupole field strength could be slightly altered to keep the cloud in focus without needing to move the camera over the course of the day. Finally, only vortices far from the edges of the BEC were counted. Vortices near the edges became less defined and more difficult to identify. Thus, a window was used in the imaging processing to limit vortex counting to within 0.7 times the Thomas-Fermi radii in expansion. Examples of the window and vortex counting procedure are shown in Figure 4.8.



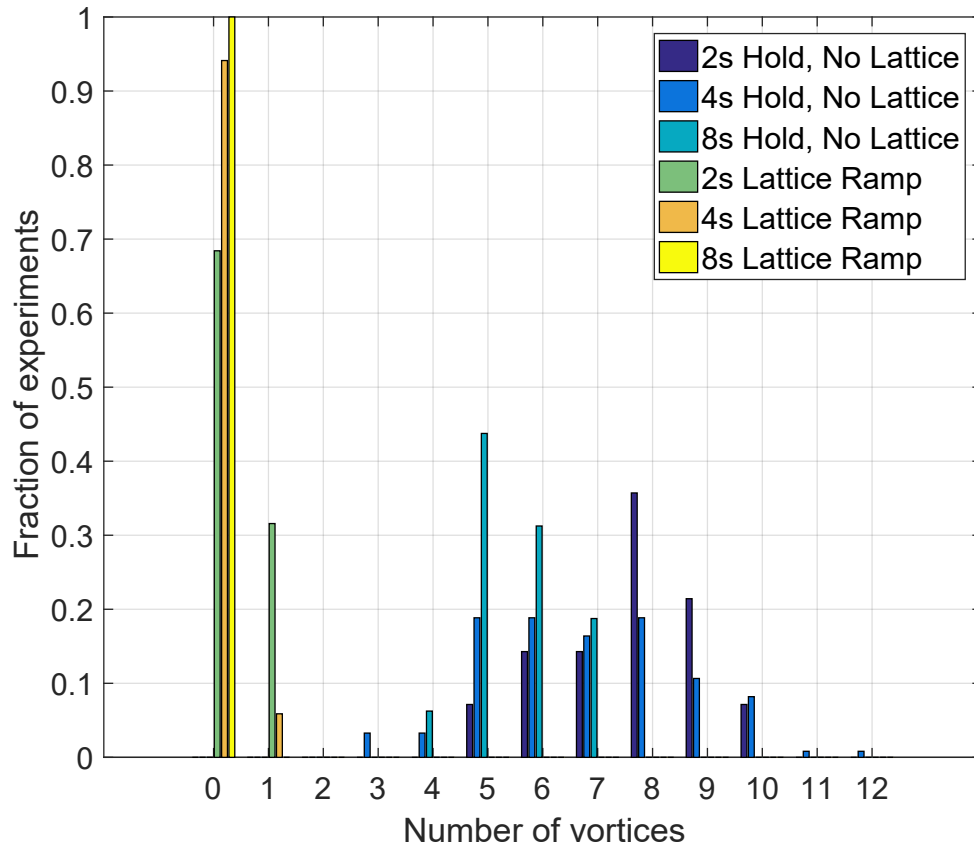


Figure 4.7: The number of vortices observed in each experimental trial were recorded and compiled. Data sets were collected for the cases of optical lattice ramp times of 2 s, 4 s, and 8 s both without an optical lattice and with an optical lattice ramp with a peak power of 130 mW. The fraction of trials in a data set with an exact observed vortex number was plotted for each case.

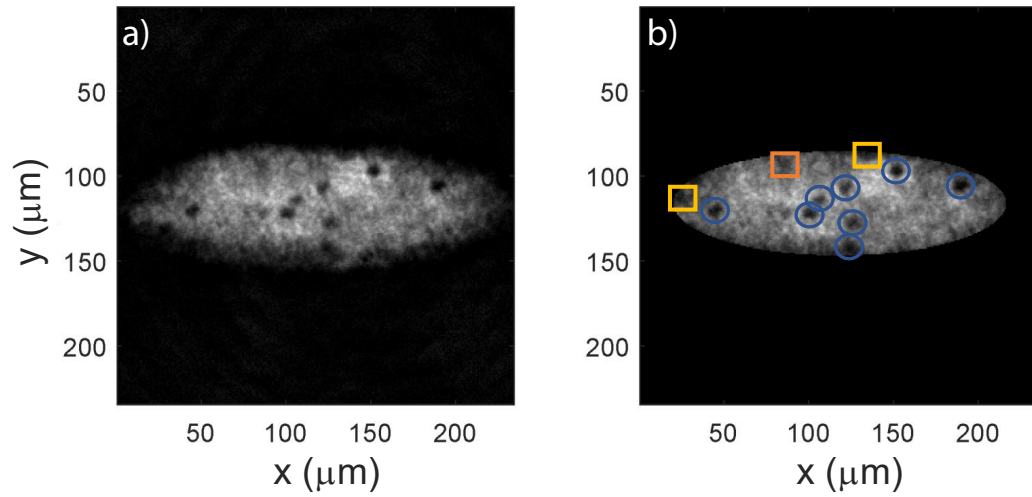


Figure 4.8: a) Vortices seen in expansion with no lattice vortex sweep. b) Example of vortices counted for data collection purposes. Blue circles represent vortices identified with reasonable certainty. Yellow boxes identify potential vortices very near the edges of the BEC, but that have lost some definition. Orange boxes represent density dip profiles that are similar in shape to a vortex but could not be distinguished from non-vortex density variations or imperfections in the imaging system. This image was identified as a BEC containing 8 vortices with 2 uncertain vortices.

If a defect in the BEC was difficult to identify as a vortex while using these conditions, the vortex in question would be recorded separately as an uncertain vortex. After processing all the vortex data, the ratio of the uncertain vortices and the total number of vortices counted was 0.15. Thus, vortices could be reliably identified with a probability of approximately 0.85.

Several hundred images were used to create the “No Lattice” data set. Between 10 and 20 images were used to analyze the effects of the optical lattice at each of the powers shown in both Table 4.3 and Figure 4.5. Fitting the data with known probability density distributions shows reasonable agreement with Poisson statistics.

#### 4.7 Conclusion

The results of this study show the efficacy of this vortex comb technique to quickly and consistently generate laminar flow BECs with well-defined ground state phase profiles. For hold times of 8 s, typical atom losses were about a factor of two. While dampening due to the thermal component of the BEC might eventually remove the vortices from the cloud, hold times of 8 s were not nearly long enough to reach such a laminar state. Additionally, losing half of the atoms over 8s holds was detrimental to successfully performing turbulence studies.

Thus, the 4 s optical lattice ramp at between 190 mW and 320 mW represented a combination of interaction time and power that resulted in atom number losses of only about 20% while reliably removing all vortices and not causing any noticeable excitation of the BEC due to the lattice ramps. Atom number losses in this optical power range were indistinguishable from losses over identical time sequences without the optical lattice. This suggests that the presence of the optical lattice at these powers does not contribute significantly to atom number losses. Significant atom losses due to the lattice were eventually seen for the 4 s ramp at powers around 1.4 W.

Future experiments may find that some combination of slightly faster ramp times

and slightly greater optical lattice powers may form a more optimized BEC with regards to managing atom losses and heating through the implementation of the vortex comb procedure. Even without such optimization, the vortex comb technique is an effective method for ensuring that a BEC is free of unwanted vortices at the beginning of an experiment.

## Chapter 5

### Various Vortex Generation and Measurement Studies: Preliminary Results

This chapter describes four preliminary experiments conducted recently in BEC Lab II. Results for each experiment are presented along with some of the challenges needing to be overcome for further investigation. The first two experiments described probed different techniques for deterministic or controllable injection of vortices into a BEC. These experiments are referred to as the “BEC poking experiment” and the “magnetic field threading experiment.” The third experiment of this chapter discusses the first steps towards the realization of single-shot vortex measurements in a BEC using a novel atom optic Shack-Hartman wavefront sensor [18]. Finally, the fourth experiment describes progress towards *in situ* observations of vortex creation and annihilation near the 2D limit of a BEC due to the Berezinskii–Kosterlitz–Thouless transition [31].

#### 5.1 Vortex cluster/dipole creation via two-pulse poking procedure

Controlled vortex generation is a vital component to the conducting of 2D turbulence experiments including further studies of vortex clustering dynamics, or other vortex dynamics experiments including the investigation of Snell’s law for vortices in a BEC [26]. Preliminary simulation studies performed in our group have shown the possibility of utilizing two lasers focused on the BEC in a short, two-pulse configuration in order to generate one or more vortex dipole pairs [15]. In this method, localized potentials in a BEC force counter-directional superfluid flow at the small, local perturbation which results in the dipolar bulk fluid flow required to form a vortex dipole.

In theory, this is a particularly advantageous method of vortex dipole generation due to its short interaction time with the BEC, the small amount of energy injected into the BEC to create the vortices, and the small region of the BEC that must be “poked” by the lasers in order to generate the vortices. Each of these aspects aid the creation of new vortices while limiting the disruption of existing vortices and their dynamics due to the injection of new vortices using the two-pulse method.

To experimentally study this technique, two lasers were added to the BEC Lab II apparatus to provide each of the necessary pulses. The first slower pulse was provided by a 660-nm laser focused at the plane of the 2D BEC with a  $1/e^2$  beam radius of  $r = 10.3 \mu\text{m}$ . The second faster pulse was provided by a 850-nm laser that was only slightly displaced from the 660-nm position and was focused near the plane of the BEC with a  $1/e^2$  beam radius of  $r = 11.2 \mu\text{m}$ . The center-to-center separation of the two beams was chosen to be  $8.4 \mu\text{m}$ . Because the 660-nm laser pulse provided a repulsive barrier as a blue-detuned beam, the pulse was termed the “blue pulse” for this experiment. Similarly, the pulse from the 850-nm laser was called the “red pulse.”

In the experiments, the total time of the two-pulse procedure was about 40 ms. Over this 40 ms, the two lasers were ramped on and off following a half-sinusoidal wavefunction. The peak powers of the red and blue pulses were measured to be  $18 \mu\text{W}$  and  $8 \mu\text{W}$  respectively. These powers corresponded to potential depths of about  $0.2\mu$ . While several different pulse timings were implemented, the most successful injection of vortices into the condensate were observed when using a blue pulse with a 35-ms period and a red pulse with a 20-ms period that was also delayed by 5 ms from the start time of the blue pulse. These wavefunctions and the locations of the beams on the BEC are shown in Figures 5.1 and 5.2. The linear portions of the ramp are 2 ms fast ramps between the zero voltage input and the input voltage required to reach the lasing thresholds of the diode lasers. These fast ramps contribute almost no energy into the BEC.

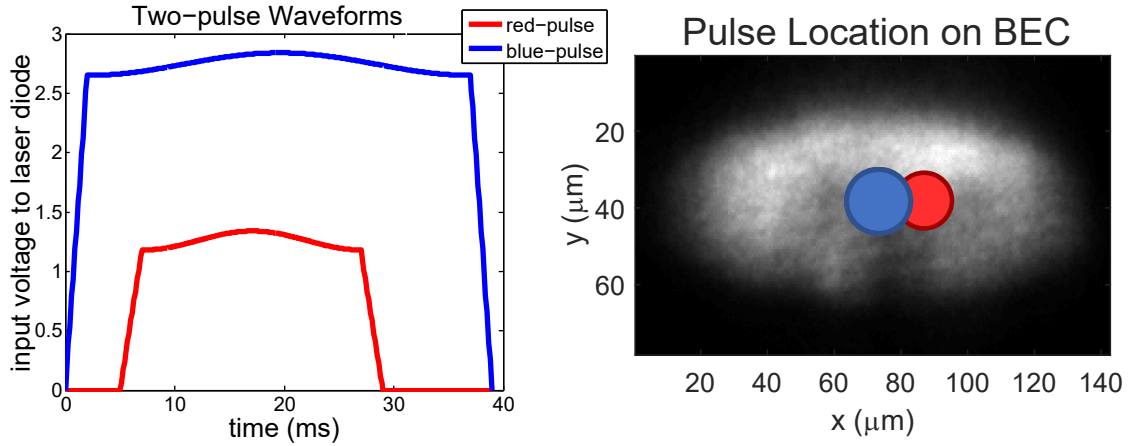


Figure 5.1: Pulse waveforms and ideal pulse locations on the BEC. The blue pulse is roughly centered on the BEC with the red pulse displaced to the right by  $8.4 \mu\text{m}$ . The voltages for each pulse have linear 2-ms fast ramps between off and the lasing threshold. Between these ramps are the 20-ms and 35-ms sinusoidal pulses for the red and blue pulses respectively with the red pulse being delayed from the blue pulse by 5 ms. Peak voltages for the red and blue pulses were 1.34 V and 2.84 V which were calculated to be 0.13 and 0.18 times the chemical potential.

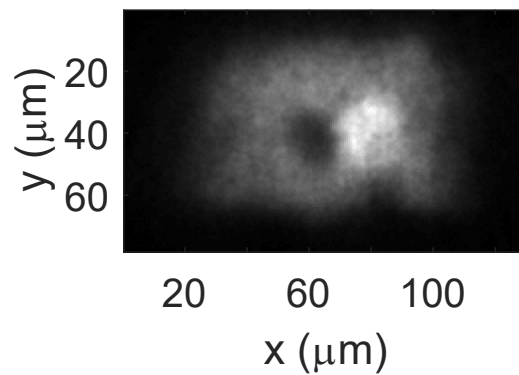


Figure 5.2: *In situ* image of the effect and locations of the red and blue-detuned lasers on the BEC at maximum intensity in steady state. The darker regions is evidence of the repulsive barrier of the blue laser while the brighter circle to the right of the darker circle is the result of the attractive potential of the red laser.

The expected physical process from observing 2D BEC simulations exhibited several key elements in the dynamics of the two-pulse process [15]. First, the blue pulse was slow enough, of low enough intensity and had a small enough profile so that it injected very little energy into the system on its own. The purpose of the blue pulse was not to generate vortices on its own, but to provide a local hole in the BEC density profile and to provide a barrier shielding the fluid flow to its left from the attractive red pulse to its right. Once the red and blue lasers had finished ramping off, superfluid flow in the BEC crashed into void left by the blue laser pulse from both sides. With well-chosen laser beam pulse parameters, the result of this fluid flow was highly dipolar and quickly formed a stable vortex dipole pair.

The results of this experiment were very surprising and can be seen in Figure 5.3. Particularly, the creation of a like-sign vortex cluster in a specific region was unexpected. The vortices in these images could be identified as like-sign vortex clusters because of the obvious signs of orbiting around each other while also precessing around the edge of the BEC together. A vortex dipole pair, on the other hand, has a very different dynamical motion in which the vortices follow non-crossing paths in which each precess about half the BEC as the distance between the vortices oscillates as seen in Figure 1.3. While the original intent of this experiment was to create vortex dipole pairs, the controllable creation of vortex clusters provided an intriguing possibility enabling other 2D turbulence studies. Sadly, these images were all taken in one day and future efforts to replicate these clusters were much less consistent.

In addition to the data set above, some experiments resulted in different arrangements of vortices. In 5.4a, a cluster of three vortices was formed due to the two-pulse procedure. Similarly, a larger cluster of four vortices is visible in another trial of the experiment as seen in Figure 5.4b. A more varied trial can be seen in Figure 5.4c where four vortices are present in the BEC but have significant spacing between them all. This could be an example of two sets of vortex dipoles pairs, but



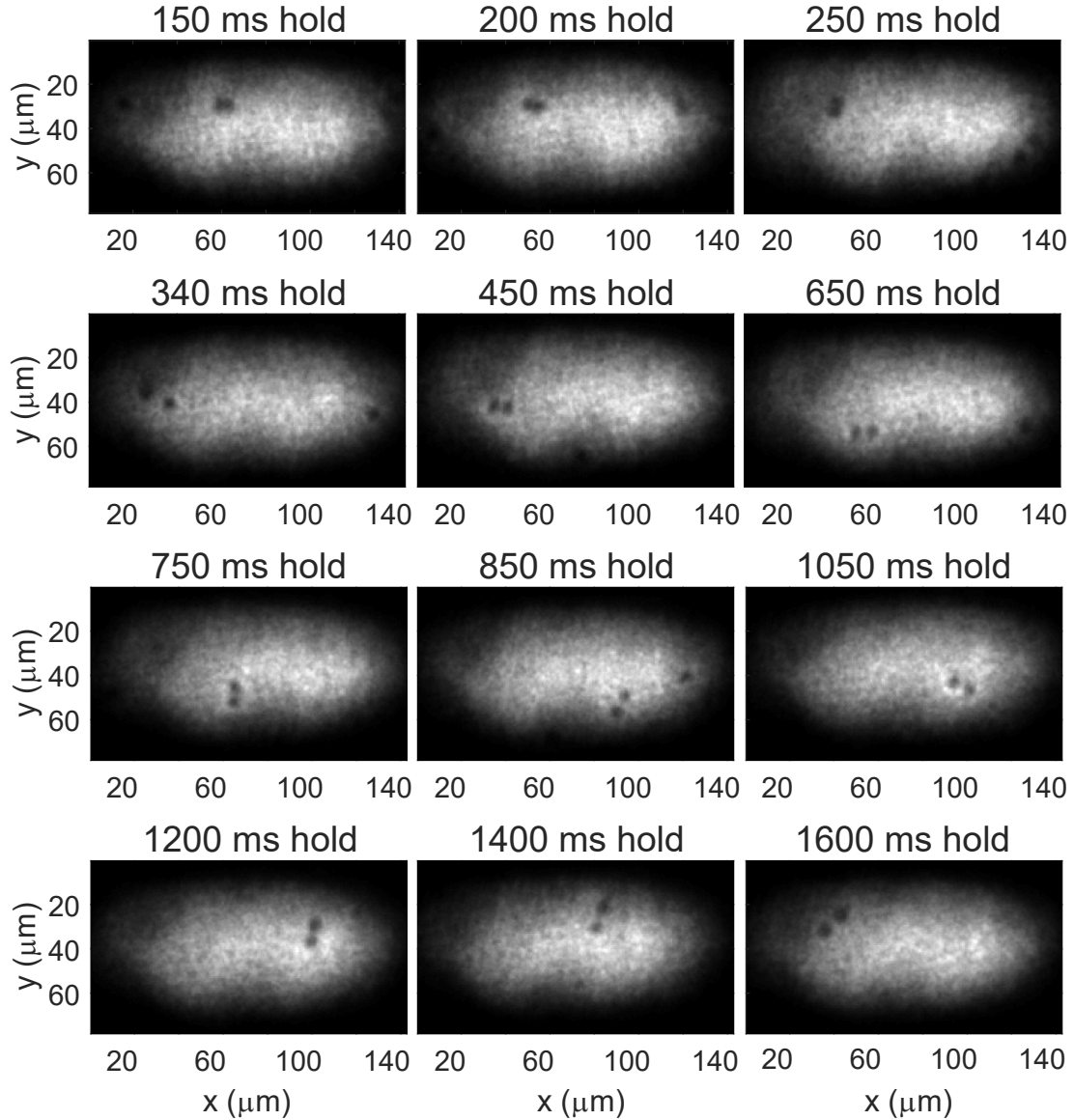


Figure 5.3: Expansion images of a vortex cluster created near the upper middle portion of the BEC shortly after the two-pulse procedure. For longer hold times, the cluster shows the vortices orbiting each other while also precessing counter-clockwise around the BEC over roughly 1.5 seconds maintaining a consistent distance from the BEC edge. Some images, such as for 200 and 340 ms hold times, show evidence of one or more vortices opposite of the cluster in question.

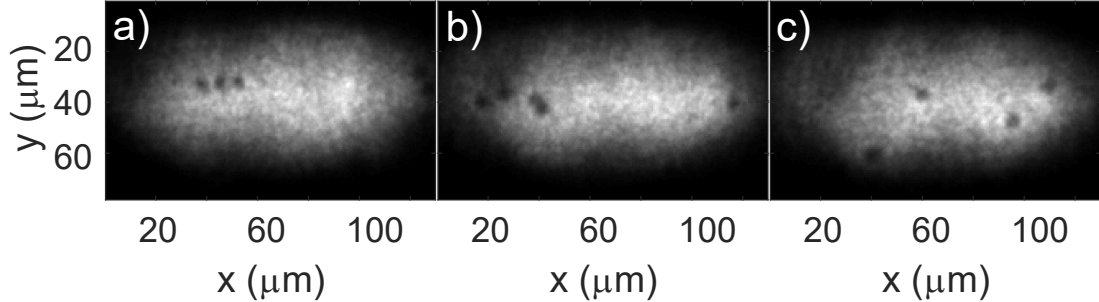


Figure 5.4: a) Image of a three-vortex cluster formed after the two-pulse procedure. b) Image of a four-vortex cluster with another vortex opposite of the cluster in the BEC. c) Image of four vortices spread across the BEC with little evidence available to determine the spin of any of the vortices.

further experimentation would be needed to understand the dynamics of this vortex arrangement.

In order to better understand why the experiment netted such unexpected results, more effort was exerted into identifying the location of the two beams. Eventually, it was discovered that the lasers were unintentionally misaligned from their intended positions as seen in roughly in Figure 5.5. Instead of being near each other, the blue and red beams were displaced above and below the y-axis center of the BEC. This was found to be the result of the focus position of the laser in the imaging system being different than the imaging plane of the BEC due to their significant differences in wavelengths: 660 nm, 780 nm and 850 nm. The result was then that the interaction region with the BEC of each laser differed from the position of the laser focus on the camera.

Taking this into account, attempts were made without much success to recreate the displaced laser pulse procedure in simulations in an attempt to understand the vortex cluster formation process. Additionally, more attempts were made in purposely misaligning the laser beams from the BEC center to recreate the vortex

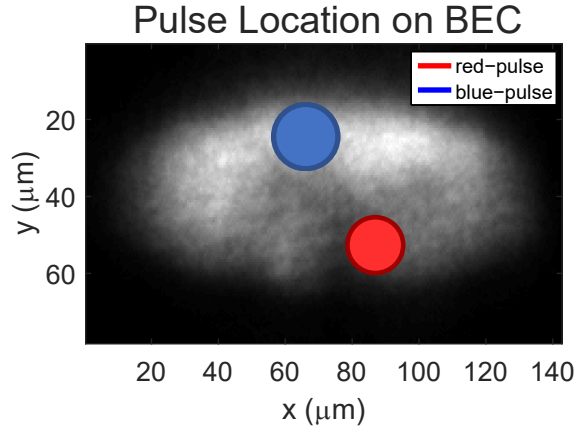


Figure 5.5: Estimated positions of misaligned pulses on the BEC after alignment of pulses imaged directly on the camera instead of alignment through BEC interaction.

clusters from Figure 5.3. These efforts also proved fruitless.

Finally, attempts were made for generating vortex dipole pairs as originally intended by using the direct laser interaction on the BEC to align the laser beams into the optimal beam positions. This laser interaction on the BEC can be seen in Figure 5.2. Unfortunately, having a small BEC with low atom numbers and having prevalent slosh in the BEC made the relative positions of these beams on the BEC extremely inconsistent. Because of this, it was hoped that this experiment could be attempted again in the future when issues like low atom number, slosh, and *in situ* vortex imaging had been fixed and optimized.

## 5.2 Vortex dipole pumping through magnetic field cycling

Recent theoretical work has investigated engineering topological defects with relation to the internal spin structures found in ultracold atomic gases in order to generate vortices within those gases [32]. Additionally, experimental work has demonstrated the creation of quantum knots using magnetic-field phase-imprinting in a 3D

BEC [33]. Simulations extending this principle into 2D BECs have shown magnetic field manipulations can similarly “pump” many vortices into a 2D BEC [34].

Inspired by these efforts, a set of preliminary experiments were run probing the possibility of vortex dipole creation in a 2D BEC. We created a topological defect in the condensate where the internal spin direction of the atoms was quickly forced to flip directions through a center point in the condensate before being returned to the original trapping scheme. This could be performed by applying a vertical magnetic bias field forcing the magnetic field to perform a pumping cycle as illustrated in Figure 5.6. As described in [34], a single pumping cycle will add angular momentum into the BEC resulting in vortex nucleation. Additionally, for the case of a potential barrier poking a hole through the center of the BEC, fluid flow circles this hole with each pumping cycle adding to the charge of the vortex. Upon ending the pumping and removing the barrier, the highly charged vortex quickly decays into many singly charged vortices [34].

To accomplish this experimentally, a BEC of about  $10^6$  atoms was trapped in a hybrid magnetic and optical trap with trapping frequencies estimated to be  $(\omega_x, \omega_y, \omega_z) = 2\pi \times (7.7, 16, 130)$  Hz. Trapping strengths in the y- and z-directions were dominated by optical forces while trapping in the x-direction was dominated by magnetic forces. The BEC was originally prepared in a 6 G/cm field with the center of the magnetic field displaced vertically below the condensate by about  $200 \mu\text{m}$ .

To limit unnecessary movement of the condensate due to movement of the magnetic field, the vertical bias field holding the zero point of the magnetic field away from the atoms was moved down to the  $200 \mu\text{m}$  mark while the atoms still had a significant thermal component. This thermal component helped to efficiently dampen slosh before the BEC underwent a final evaporation step to approach a pure condensate.

This position of the zero point of the magnetic field relative to the BEC helped to avoid problems occurring with excessively tight trapping geometries. As the zero

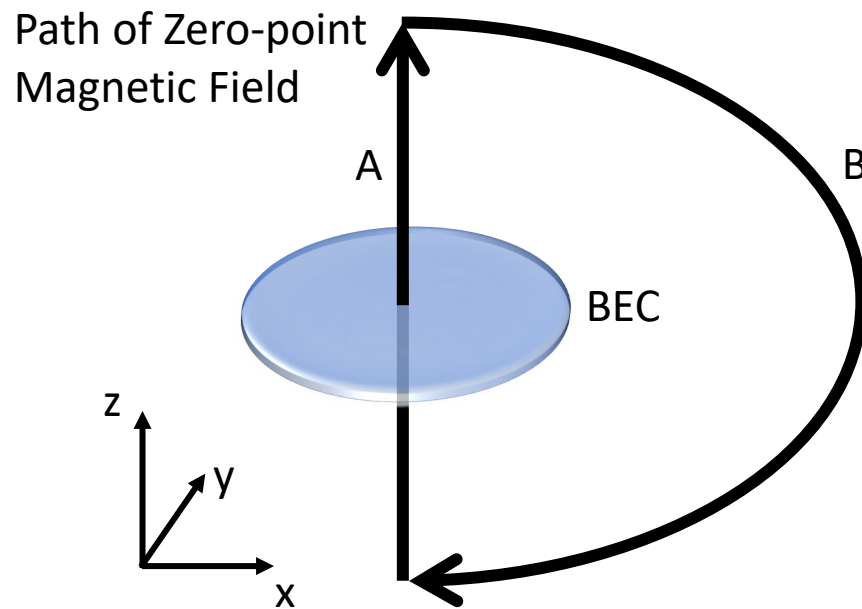


Figure 5.6: Path of the zero-point of the magnetic field over one “pump” cycle. In path A, the magnetic field zero-point moves upward through the center of the condensate. In path B, the magnetic field zero-point moves around the condensate back to its original position. This idea was numerically explored in Reference [34].

point of the magnetic field approached the BEC, the radial trapping frequencies increased which also increased the density of the atoms. Higher density BECs result in increased 3-body recombination losses. Additionally, if the zero point was held too closely to the BEC, Majorana losses due to spin flips would also become an issue. A distance of  $200 \mu\text{m}$  separation of the zero point magnetic field and the BEC was found to avoid both these issues.

Once a BEC came to equilibrium at the desired position, the magnetic threading procedure could begin. In this procedure, the magnetic field zero position would be quickly and linearly brought through the center of the condensate to a point roughly  $200 \mu\text{m}$  above the condensate, path A from Figure 5.6. After completing this ramp over 5.6 ms, the zero point would be returned to its original position over 0.25 ms with fast horizontal bias ramps ensuring that the zero point traveled around, away from the condensate rather than through it again, path B from 5.6. Figure 5.7 shows two images of BECs immediately after the magnetic zero point had passed through the condensate except with an additional 20 ms hold time when the magnetic field zero point was very close to the condensate. The hole in the condensate is likely due to the Majorana losses associated with the presence of the magnetic field zero point overlapping with the high density condensate. This hole allowed for the alignment of the magnetic threading through the center of the condensate.

Fast ramps were essential in this process to avoid excessive movement of the atoms due to the shifting magnetic fields and excessive losses from spin flips as the magnetic field zero passed through the condensate, as clearly shown in Figure 5.7. Because the Larmor precession response of the magnetic dipole moments is faster than the physical movement of the atoms, the magnetic field could be ramped at these very fast time scales while still accomplishing the pumping needed to stir up vortices.

As seen in Figure 5.8, vortices were formed as a result of this procedure. The BECs in Figure 5.8 were the result of the procedure from above being applied 3

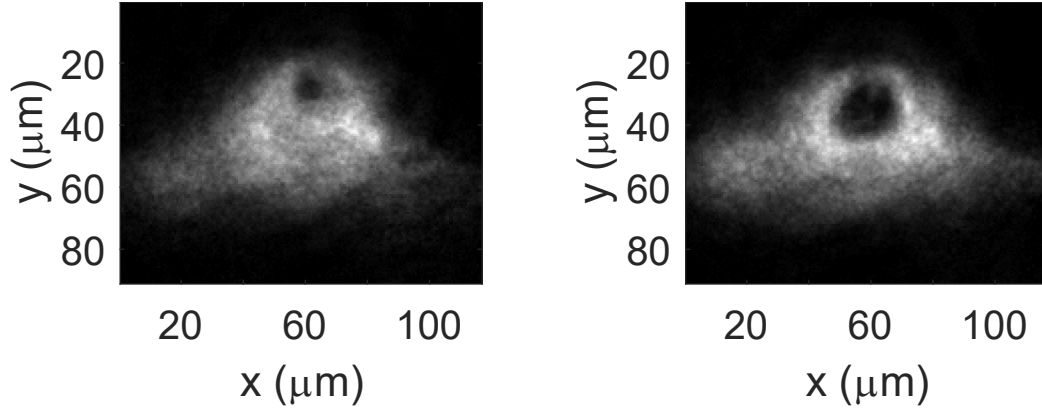


Figure 5.7: BECs imaged after the zero point of the magnetic field was ramped very near the BEC and held there for 20 ms. The hole likely represents atom loss due to Majorana losses at the magnetic field zero point. This method proved a viable method for aligning the magnetic threading process through the center of the condensate. The right image has a slightly larger horizontal magnetic field bias providing better alignment of the zero-magnetic field position to the center of the BEC.

times in succession with a 1 second hold before being imaged in expansion.

Several variations of this pumping were explored in order to minimize the energy imparted into the BEC not associated with vortex formation. One such variation was to use more and faster threading cycles. Limiting the interaction time of the magnetic zero point with the condensate in this way seemed to help control heating and losses from this pumping scheme. However, generally more magnetic bias cycles meant that the BEC was held in an effectively tighter trap for longer time durations. As seen in Figure 5.9, this led to the excitation of breathing modes in the direction of the BEC dominated by the magnetic trapping. For attempts using many pump cycles or the inclusion of a barrier plug at the magnetic threading location on the BEC, this breathing would result in significant heating and atom loss.

Major roadblocks for further investigation into this pumping scheme were losses due to Majorana losses during the threading cycle and atom losses due to heat-

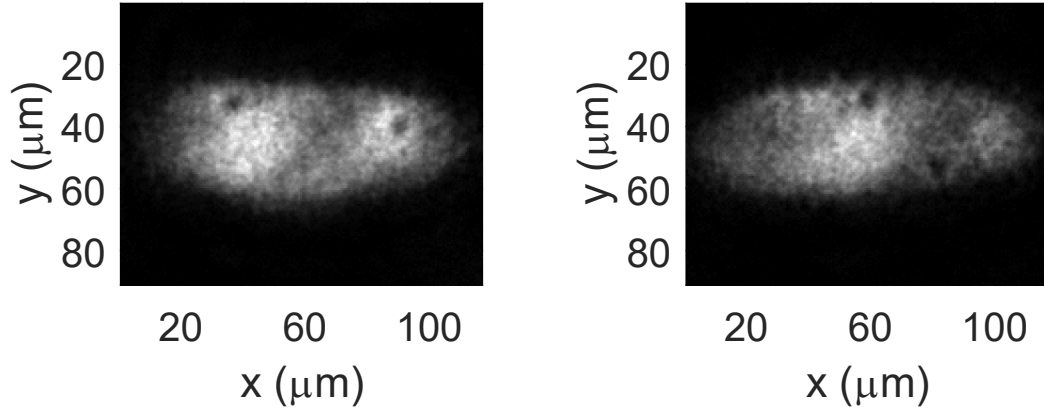


Figure 5.8: BECs with vortices imaged after 3 applications of a 5.85-ms magnetic threading cycle procedure. Both BECs were allowed to evolve for 1 second before being imaged in expansion.

ing of the BEC from excited breathing modes. Additionally, losses from excited breathing modes were exasperated when using a plug beam which was implemented to reduce Majorana losses. Future experiments to correct this will likely need an all-optical trap. An all-optical trap would allow weaker magnetic fields to be used while not sacrificing radial confinement of the BEC. Weaker magnetic fields along with trapping frequencies dominated by optical forces would reduce the excitation of the breathing modes associated with the varying magnetic field strengths during the pumping cycles. Without breathing excitations, a plug beam should be able to poke a hole in the BEC through which the magnetic zero point can be threaded without excessive heating. Using a plug beam in this way should alleviate losses from Majorana losses theoretically allowing many magnetic pumping cycles without heating or atom loss which would in turn efficiently excite many vortex dipole pairs.



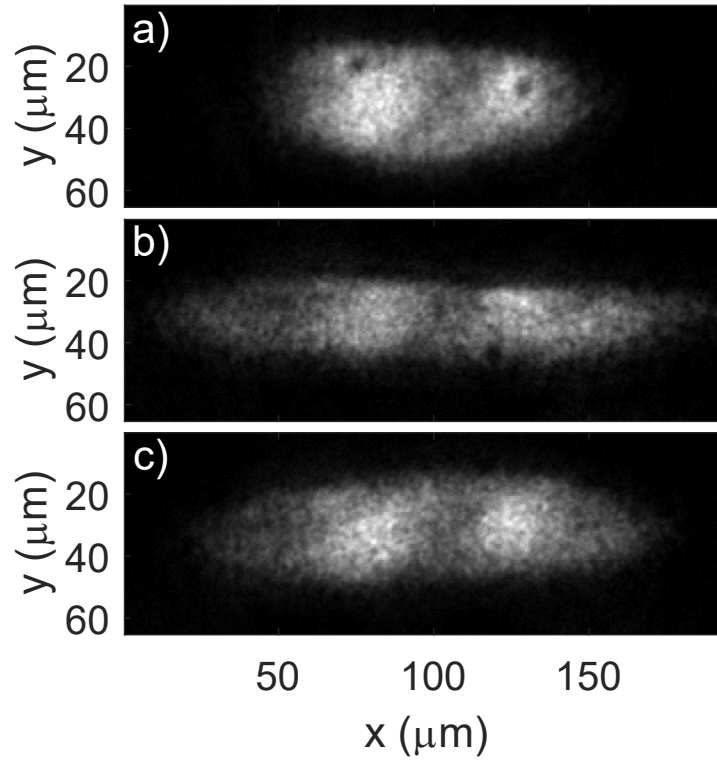


Figure 5.9: BECs with vortices imaged after 3 applications of a 5.85 ms magnetic threading cycle procedure. Images a), b) and c) show the BEC evolution after the magnetic threading cycling with hold times of 1, 1.5, and 2 seconds respectively. The Thomas-Fermi radii of these BECs were  $66 \mu\text{m}$ ,  $107 \mu\text{m}$  and  $88 \mu\text{m}$ . This expansion and contraction of the BEC over time in the magnetically trapped direction of the BEC is likely evidence of a breathing mode excitation due to the sudden increase and decrease of the magnetic trapping strength associated with a magnetic field threading application.

### 5.3 Single-shot vortex measurements with 1D Shack-Hartmann wavefront sensor

Progress was made toward the demonstration of the 1D atom-optic Shack-Hartmann wavefront sensor proposed by Nerenberg in [18].

Traditionally in optics, Shack-Hartmann wavefront sensors have utilized a microlens array to measure the wavefront shape and intensity profiles of beams. In the atom-optic analog to this measurement scheme, optical lattices are used in place of the microlens array in order to make measurements on the wavefront of a quantized matter wave, in our case a BEC. While this new scheme may have many potential uses beyond turbulence studies in BECs, the ability of this atom-optic Shack-Hartmann wavefront sensor to make a complete single-shot measurement of the phase information of a 2D BEC would provide a new and powerful tool for vortex measurements in future 2D quantum turbulence studies. In his dissertation, Nerenberg provides procedures using either a 1D or 2D optical lattice for vortex detection and measurement [18]. Using the optical lattice and reliable vortex generation method described in Chapter 4, experiments were conducted testing the efficacy of a 1D atom-optic Shack-Hartmann wavefront sensor.

The measurement of a vortex using this scheme relies on local phases being imparted to the BEC by a short pulse of the optical lattice. Using a 1D lattice, the interaction of the lattice lines with the BEC will create a diffraction pattern after the BEC is allowed to freely evolve. This is due to the momentum kick provided by the blue-detuned lattice pulse during which atoms are pushed away from the high intensity lattice sites.

For BEC dynamics, it is understood that fluid flow and the phase of the condensate are directly related. Thus, the introduction of a new phase gradient at each lattice site provides a type of measuring stick across the BEC. If no other phase gradient is near the position of the lattice pulse, a short time after that pulse a dark

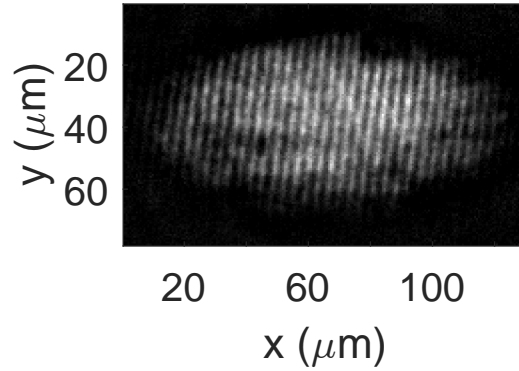


Figure 5.10: The lines in this BEC were imaged after the following procedure: 7 ms expansion, 220  $\mu\text{s}$  lattice pulse at 0.66 V, another 1 ms expansion, and then the Faraday imaging procedure. The pulse at this computer output voltage corresponds to about 350 mW, about a maximum potential amplitude of  $15\mu$ .

line will appear where the lattice lines were most intense as seen in Figure 5.10. This effect is different than the vortex comb interaction of Chapter 4 where atoms were held between lattice sites. Instead, the lattice never approached intensities capable of creating distinct BEC sights at equilibrium and the short pulse ensured that the lattice had been off for some time before the image was taken.

Because each of these lines are then the product of a phase gradient, the result of such a line being superimposed over a vortex should result in the breaking of the line due to the opposite phase gradient on either side vortex core. Simulations in [18] showed that for pulses of 220  $\mu\text{s}$  with max amplitude lattice sights corresponding to potential depths of  $1\mu$ , this expected breaking of the diffraction lines could be observable.

In Figure 5.11, a number of images are shown corresponding to the results of experimental trials run near these simulated parameters with the exception of a stronger lattice amplitude at about  $15\mu$  and with variable post-pulse expansion times. Unfortunately, there was no clearly observable breaking of the lines as was

hoped. However, several of the images, such as the 1.00 ms and 1.21 ms expansion images from Figures 5.11, showed some bending of the lines when in proximity to a vortex core similar to the bending of the soliton lines from Section 3.6. A comparison of these bending lines is shown directly in Figure 5.12.

Further investigation of this technique will likely need to ensure that the pulse duration is closely following the computer output from the timing software. While lattice timings over long times scales such as those used for the vortex comb experiment of Chapter 4 were accurate, the timing accuracy of very short pulses through the optical system of Figure 4.1 were never verified. Additionally, the vortex comb technique proved to be very reliable over a large window of amplitudes of the lattice potential. It is possible that either daily or weekly drifts in the lattice power were present. This in turn would feasibly result in the stated lattice powers tested above to be inaccurate. For future work on this scheme, additional effort should be made to ensure the accuracy of the lattice pulse timing and intensity.

#### 5.4 BKT transition near 2D limit of BEC

Progress was made toward *in situ* imaging of vortex-antivortex dipole pairs created via the Berezinskii–Kosterlitz–Thouless (BKT) transition near the 2D limit of a BEC [31, 35, 36, 37]. The experiment was conducted by construction of a new blue-detuned optical dark trap that provided a stronger vertical trapping scheme to efficiently approach the 2D limit of a BEC from an initial 3D trapping geometry. Details including the optical set-ups, atom loading, beam profiles, and other specifications of this dark trap can be found in Section 2.2.

The approximate initial trapping strengths of this new dark-trap set-up were  $(\omega_x, \omega_y, \omega_z) = 2\pi \times (6.8, 6.8, 230)$  Hz. Additionally, horizontal trapping strengths could be further decreased by adding a vertical magnetic bias to the quadrupole magnetic field. This additional bias field could ramp the atoms from 3.5 G up to about 8.1 G greatly reducing radial trapping strengths. The following three

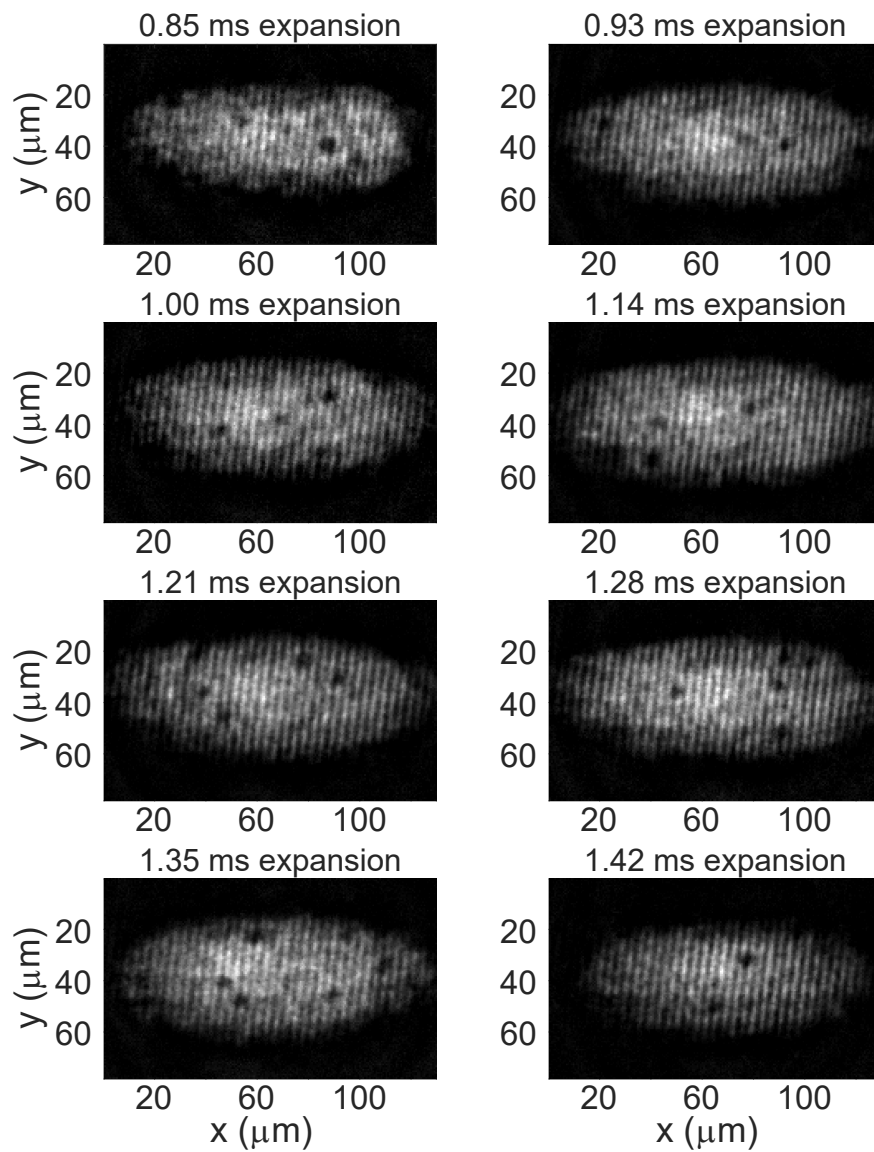


Figure 5.11: Trials were conducted using the 7 ms pre-pulse expansion time followed by a  $220 \mu\text{s}$  lattice pulse in the presence of vortices. Atoms were then allowed to expand for the times labeling each image before imaging the condensate.

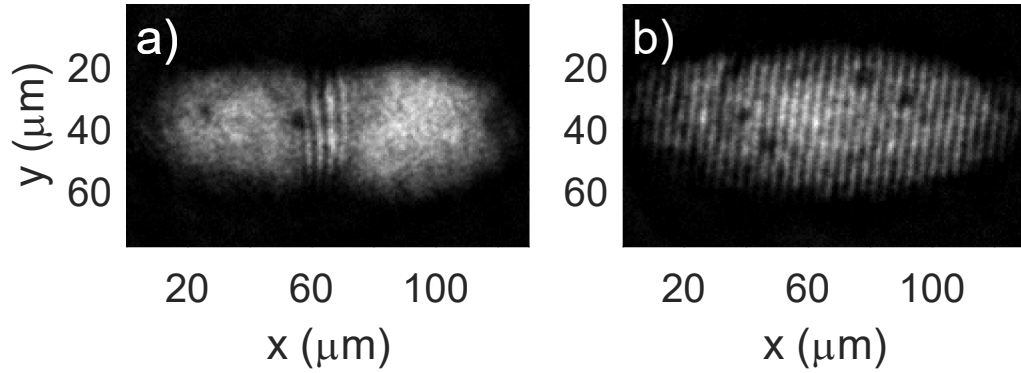


Figure 5.12: Images of lines in a BEC showing some curvature when in proximity to a vortex core. a) Soliton lines generated via a merging procedure described in detail in Chapter 3. b) Diffraction lines generated through pulsing a 1D optical lattice over the BEC.

preliminary experiments were performed on BECs of  $\sim 4 \times 10^5$  atoms in this dark trap.

These three different preliminary experiments were conducted in an effort to determine if *in situ* imaging could be used to explore the BKT transition of a trapped BEC near the 2D limit. All three methods represent a different strategy to “freeze” the condensate’s vertical energy to the ground state of the harmonic optical dipole trap and to decrease the condensate density to the limit where the energy of a vortex dipole pair approached the energy of a thermal excitation in the 2D trapping potential.

The first method, with arguably the best results, relied on ramping up a vertical, magnetic bias field in order to adiabatically decrease the radial trapping frequencies at the condensate. This single step achieves both conditions for a BKT transition as stated above. First, as the radial trapping frequencies are lowered while keeping a constant vertical trapping frequency, the condensate’s density will decrease as the gas expands to the appropriate Thomas-Fermi radii associated with its new trapping frequencies. Expanding the cloud in this way also slightly decreases the

vertical thickness of the cloud without increasing atom density, this flattening of the cloud brings it closer to a 2D geometry and decreases the energy per unit length associated with a vortex line dipole pair which is given by

$$\epsilon_{line} = \frac{2\pi\hbar^2 n}{m} \ln\left(\frac{R}{d}\right). \quad (5.4.1)$$

In this equation,  $n$  is the local density of the condensate in the absence of the vortex cores,  $m$  is the mass per atom,  $R$  is the distance of the vortex dipole from the boundary of the condensate, and  $d$  is the separation of the vortex-antivortex pair from each other. Assuming a Thomas-Fermi radius in the vertical direction of  $r_{TFz}$  and integrating over this vertical dimension of the BEC results in a total dipole energy of

$$\epsilon_{dipole} = \frac{8\pi\hbar^2 n r_{TFz}}{3m} \ln\left(\frac{R}{d}\right). \quad (5.4.2)$$

Vortex dipole pairs created from the BKT transition are thus expected to be observed when  $\epsilon_{dipole} \approx \hbar\omega_z$ .

Two sets of experimental runs were processed differing only by magnetic bias ramp times. In both variations, the atoms were transferred to the 532-nm optical dipole trap as described in Section 2.2. After this, the BECs were imaged with some expansion after being ramped to one of three different vertical magnetic field bias values, as *in situ* imaging was not sufficient to resolve vortices. These three points of interest held the atoms at magnetic fields of approximately 3.5 G, 5.4 G or 6.7 G in the 27 G/cm trap. Radial trapping frequencies of the associated fields were approximately,  $2\pi \times 6.8$  Hz,  $2\pi \times 5.0$  Hz and  $2\pi \times 3.5$  Hz, respectively. In the experiments, magnetic fields were ramped from 0 to the target magnetic field bias in times of  $t_0$  or  $3t_0$  with  $t_0$  being the period of the radial trapping frequency. As can be seen in Figure 5.13, the number of vortices observed varied for differing ramp times at identical trapping strengths as more vortices observed corresponded to the faster ramp,  $t_0$ , condition. Expansion times varied between 5 ms and 7 ms for optimal vortex detection depending on initial atomic cloud density.

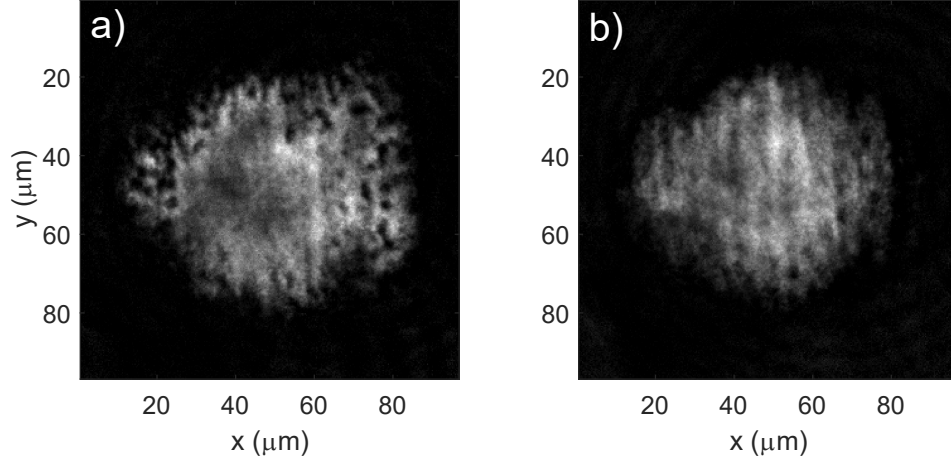


Figure 5.13: a) Fast  $t = t_0$  ramp to  $\omega_r = 2\pi \times 3.5$  Hz trap at 6.7 G showing clear vortex formation around edges of BEC. b) Slower  $t = 3t_0$  ramp to  $\omega_r = 2\pi \times 3.5$  Hz trap at 6.7 G showing some vortex formation but with much less clarity.

Comparing the two ramp times, vortices were more clearly visible under fast ramp conditions. This could possibly be due to a larger thermal component present in the image which could appear and obscure vortices for longer experimental run times. However, side profile imaging after some expansion provided inconclusive results as to the significance of the thermal component associated with the two ramp times. Another possible reason for poor vortex image quality could be drifting of the vertical position of the BEC due to drifting of the trapping beam position or drifting of the quadrupole field strength. Over short time scales, the trapping beam was shown to drift from its center position by  $\pm 1.5 \mu\text{m}$ . Additionally, shot-to-shot magnetic drifts of the quadrupole field of about 1% have been identified which could also shift the center of the vertical trapping position. More data will need to be taken to identify the likely cause of this poor vortex imaging for slow magnetic ramp conditions.

Near the 2D limit, it was expected to observe the formation of vortex-antivortex



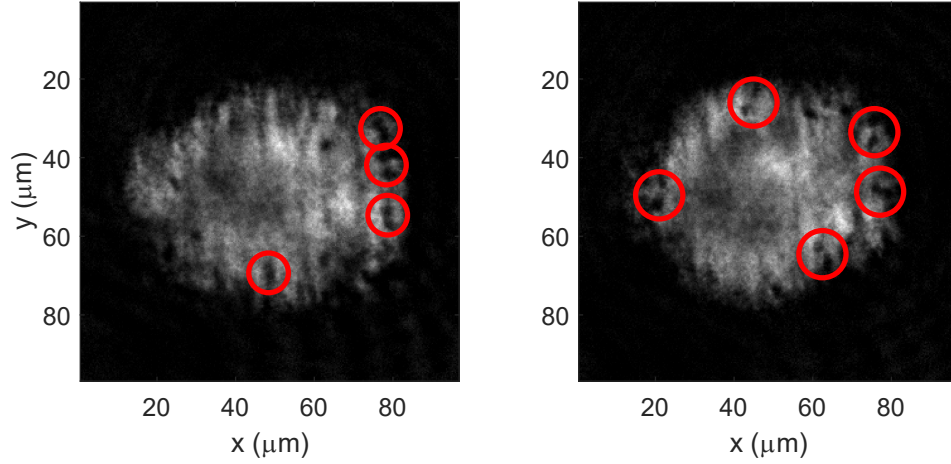


Figure 5.14: Two images of BECs after a fast ramp to the  $\omega_r = 2\pi \times 5.0$  Hz trap at 5.4 G. Red circles highlight potential vortex dipole pairs near the BEC edge where vortex dipole pairs formed due to the BKT mechanism would be expected to appear first.

dipole pairs. With these trapping and ramping conditions, the edges of the BEC would approach the 2D limit before the center of the BEC. Thus, dipole pairs created through a BKT transition mechanism should first appear around the edges of the BEC. Figure 5.14 shows two BECs with vortices generated from a fast ramp to the 5.4 G position. Red circles highlight pairs of vortices that are possible vortex dipole pairs. The energy of a dipole pair of vortices with  $\sim 5 \mu\text{m}$  separation and  $\sim 10 \mu\text{m}$  distance from the Thomas-Fermi radius edge is  $\epsilon_{dipole} \approx 0.37\hbar\omega_r$  using equation 5.4.2 from above where  $\omega_r = 2\pi \times 5.0$  Hz (separation and distance values correspond to general values measured from the vortices from Figure 5.14). This means a thermal excitation has more than enough energy to produce the possible vortex dipole pairs shown in Figure 5.14.

Also, there is a general advancement of vortices towards the center, denser portion of the condensate as radial trapping frequencies were relaxed and the cloud

approached the 2D limit as shown in Figure 5.15. While it became much more difficult to identify potential vortex dipoles in these more 2D condensates, vortices were found both in greater number and closer to the center of the condensate as the aspect ratio of the trap became more 2D. Both items provide evidence that the vortices imaged could potentially have been the product of the expected production and annihilation of vortex-antivortex pairs near the BKT transition.

One major issue encountered through this experiment was structure on the 532 nm trapping laser. As seen in the *in situ* image in Figure 5.16a, structure on the edges of the BEC was visible even in the initial 3.5 G trapping configuration and only became more significant as the cloud became more 2D as shown in Figure 5.16b. The image in Figure 5.16b was taken with the BEC in the 6.7 G configuration.

While expanding the BECs for imaging managed to largely wash out this structure when looking for vortices under these conditions, the structure began to degrade image quality for BECs held in further weakened traps beyond the 6.7 G trapping configuration. Figure 5.17 shows vertical lines in a BEC imaged with expansion that was originally held in a 8.1 G trapping configuration. These lines obscured vortices from being reliably identified which then placed a limit on the extent to which we could decrease the radial trapping strengths of our system. Additionally, as the weaker trapping configurations caused the structure to become more significant, any slosh in the BEC would cause catastrophic heating of the BEC and significant atom loss. More discussion of the structure on the beam can be found in Section 2.2. Also unfortunately, these weaker traps were needed for *in situ* vortex detection.

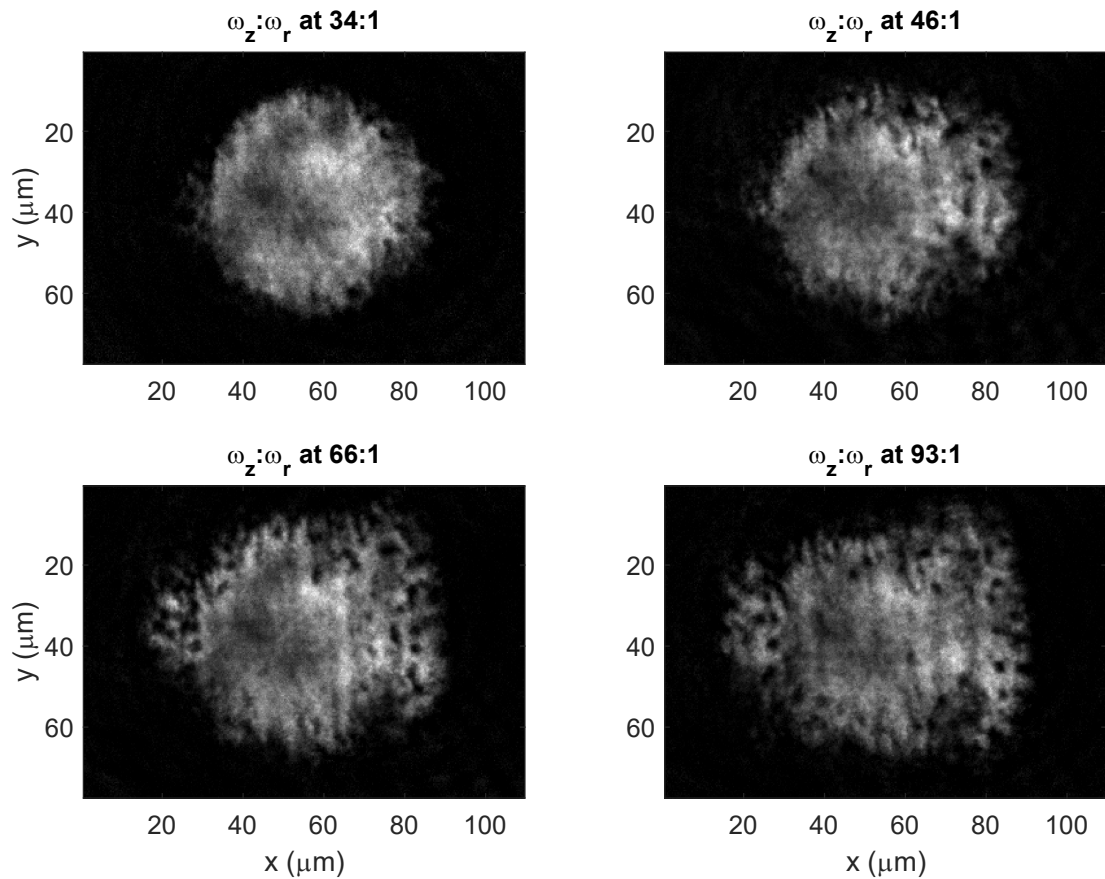


Figure 5.15: BECs imaged in expansion after trapping parameters were ramped quickly to more 2D configurations. The 34:1, 46:1 and 66:1 aspect ratios of trapping strengths correspond to the 3.5 G, 5.4 G and 6.7 G trapping configurations, respectively. The 93:1 aspect ratio configuration was reached through a fast ramp to the 6.7 G condition which was followed by a 0.1 s linear 40% power increase in the trapping beam.

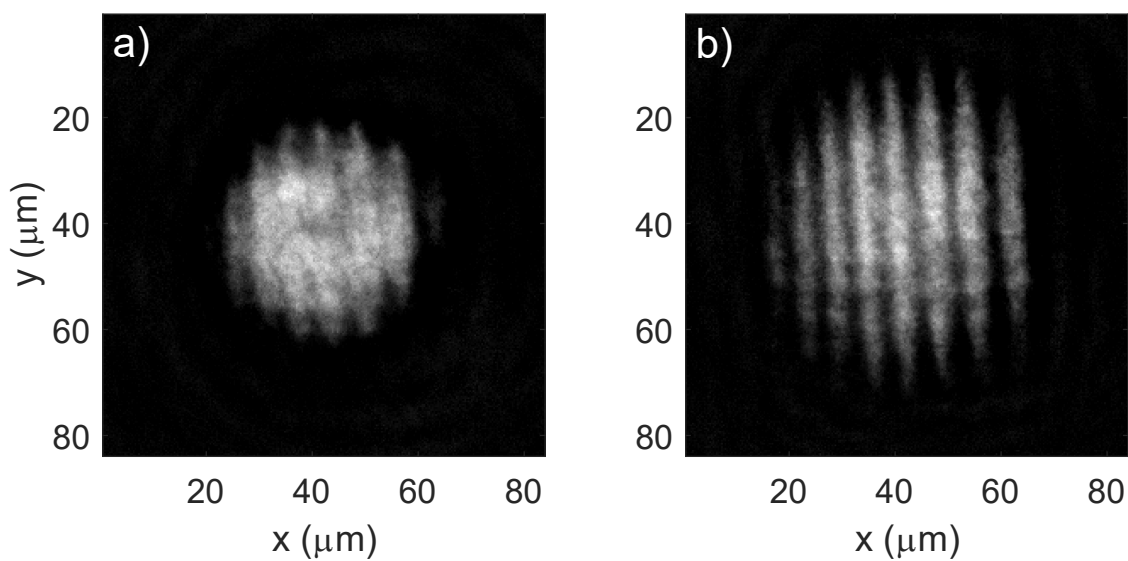


Figure 5.16: a) *In situ* BEC image immediately after transfer to the dark trap in the 3.5 G trapping configuration. Some signs of structure can be seen in the periodic density dips around the edges of the condensate. b) *In situ* BEC image after ramping the BEC to the 6.7 G trapping configuration. Lines through the BEC due to trapping beam structure have become much more significant as the weakened radial trapping frequencies have decreased the chemical potential of the BEC.

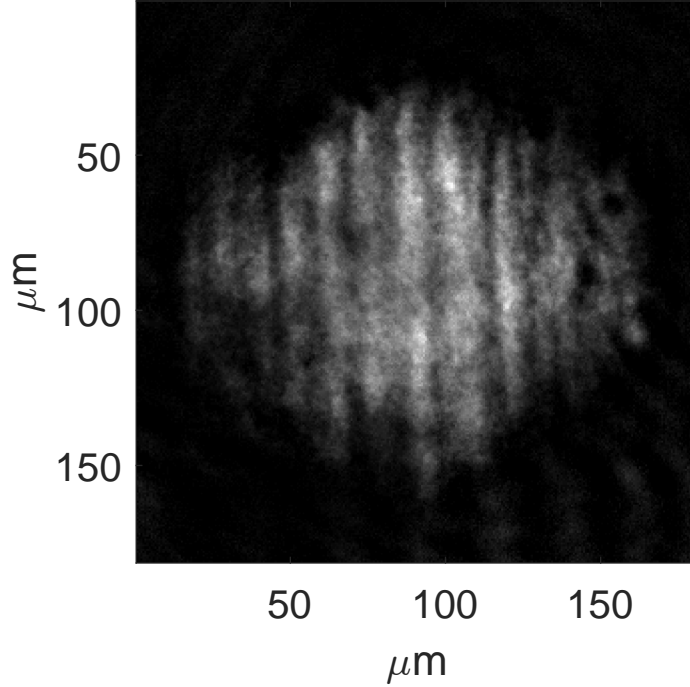


Figure 5.17: BECs imaged in expansion after being ramped to the 8.1 G trapping configuration. Structure on the beam has left visible lines on the cloud even after being allowed to freely expand for 6 ms. Vortices may be present in the BEC, but cannot be detected reliably due to the lines.

In an attempt to confirm that vortices produced in the previous images were due to the BKT transition and not atom cloud movement over optical structure, another experiment was performed to minimize any movement of the BEC while approaching the BKT limit. To accomplish this, the density of the atom cloud was reduced, without ramping any fields, until the cloud approached the critical number associated with the BKT transition,

$$N_{crit} = 724 \sqrt{\frac{2\pi\omega_z^3}{\omega_r^4}}. \quad (5.4.3)$$

This critical number can be compared to the previous BKT transition expression

of  $\epsilon_{dipole} \sim \hbar\omega_z$  by noticing that both expressions predict the BKT transition to occur when the density and vertical thickness of the cloud are decreased to the 2D limit. We achieved both these goals by simply holding the atoms in the 532nm optical trap and allowing background gas collisions to decrease atom number in the BEC without significantly heating the condensate. In the initial trap at 3.5 G,  $N_{crit}$  was calculated to be approximately  $6 \times 10^4$  atoms. Because it was possible to ramp slowly to the 5.4 G position without significant heating, the atoms were once again brought to the 5.4G trapping configuration over a very slow ramp time of  $10t_0$ . The new critical number for this trap was  $1 \times 10^5$  atoms.

After hold-plus-ramp times of between 1 and 10 seconds, the number of atoms in the BEC was reduced by almost 90%. At the initial conditions described previously, the initial atom number of  $\sim 4 \times 10^5$  atoms was approximately  $4N_{crit}$ . Vortices were not regularly observed in expansion images at this starting point. After losing roughly 75% of its atoms, the BEC number was approximately equal to  $N_{crit}$  which corresponded to a hold time of about 7 seconds as shown in Figure 5.18. While vortices can be observed in the images of Figure 5.18, the vortices are very difficult to pair into vortex dipole pairs for further investigation. This breaking apart of dipole pairs was also seen for long hold times in the simulation study by Simula *et al.* in [35]. Their study also found that the probability of vortex dipole observations is dependent on the temperature of the system. Better temperature control in this experiment may then be needed to provide a better comparison to the magnetic relaxation experiment.

A final experiment to observe vortex production near the BKT limit was attempted by decreasing the density of the BEC through addition of a circular, uniform blue-detuned mask of half the width of the Thomas-Fermi radius to create local region of decreased radial trapping frequencies and decreased atomic density. Because the poking beam was not perfectly uniform, it was difficult to find a poking beam power that created a region large enough and capable of creating and

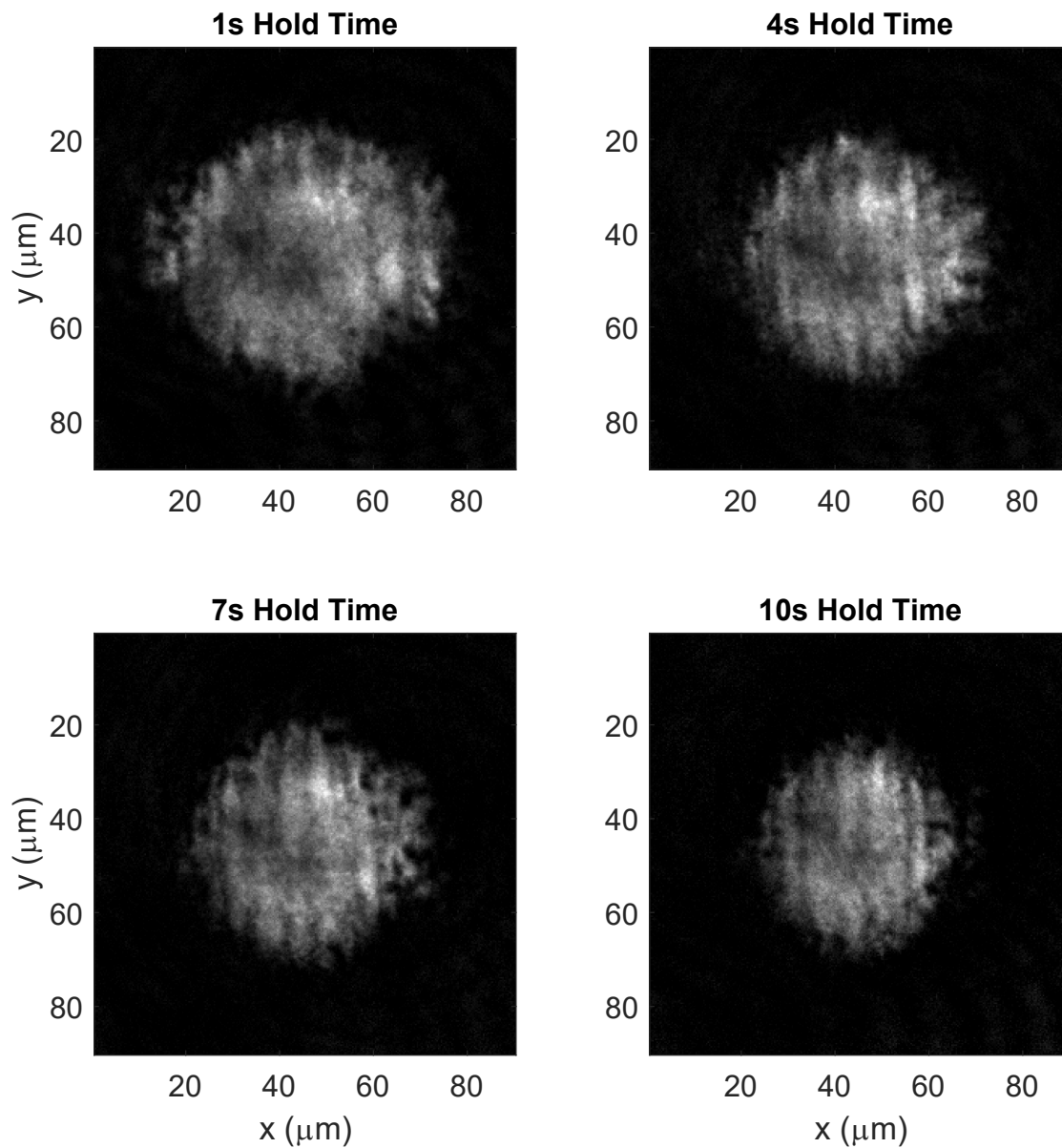


Figure 5.18: BECs imaged in expansion after being ramped to the 8.1 G trapping configuration. Structure on the beam has left visible lines on the cloud even after being allowed to freely expand for 6 ms. Vortices may be present in the BEC, but cannot be detected reliably due to the lines.

observing vortices without entirely poking a hole through the condensate. If there was a small hole poked through the condensate, it was difficult to distinguish that hole from a vortex core in short expansion times. Additionally, for longer expansion times, the jump from trapped to expansion parameters provides a significant source of energy as sound waves could be seen in the BEC once the poking laser was removed for expansion. Another issue yet was when vortices were observed, it was ambiguous if they had been produced due to slosh over the barrier or from a BKT transition mechanism.

Although *in situ* vortex detection was not achieved, technical improvements to the stability and quality of our trapping parameters should allow for future *in situ* imaging of BKT vortices. With further improvements to multi-shot imaging, the observation of *in situ* vortex-pair production could also be achievable.



## Chapter 6

### Apparatus Hardware Upgrades

#### 6.1 Magnetic bias polarity flipping electronics

Our BEC machine largely utilizes an optical dipole/magnetic quadrupole combination trap. However, in the first steps of RF-evaporation, only the magnetic quadrupole trap is utilized. Before starting the process of evaporation, we first use a vertical bias field to pick the vertical location of the atomic cloud which will be most advantageous for avoiding unwanted diffraction due to defects on the science cell. This is necessary due to the peeling of the AR-coating on the outside of the science cell which in turn causes significant imaging artifacts in our side-profile imaging system as well as unwanted beam structure on optical lattices and traps input through the same science cell window. Evidence of this unwanted diffraction is seen in the thick, dark lines and artifacts across the background images as seen in Figure 6.1. By simply shifting the vertical position of the atomic cloud, we can choose a window of the science cell where these unwanted effects are much less significant.

By choosing to move the vertical bias field for the initial position and because the bias field is not perfectly aligned with the quadrupole field, it is necessary for the apparatus to utilize two more magnetic field bias coils in each of the transverse directions to allow for the corrections necessary to keep the magnetic field center fixed in the transverse direction as it varies in the vertical direction. If this is not accomplished, losses and heating will degrade the quality of the BEC. Examples of this are losses due to misalignment of the plug beam during transfer to the red optical dipole trap leading to excessive Majorana losses. Additionally, significant

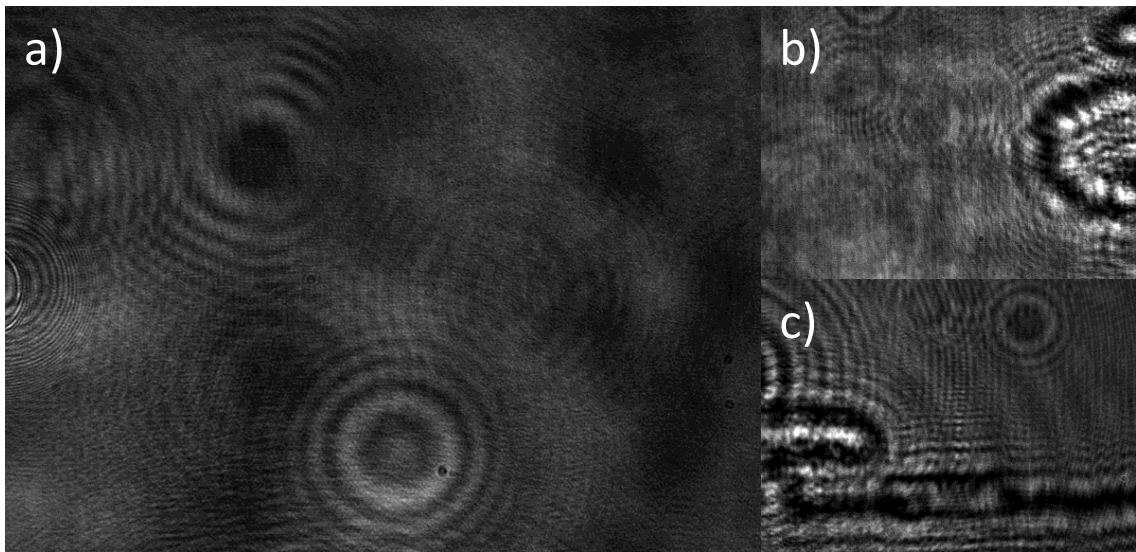


Figure 6.1: a) Background of side-profile camera aligned to the current atom location relative to the science cell with no atoms present. Some diffraction due to dust present. b)-c) Backgrounds of side-profile camera aligned to old atom locations relative to the science cell. Significant imaging artifacts due to AR-coating issues seen on rightmost side of b) and along the bottom and left side of c).

heating and non-optimal evaporation due to slosh of the BEC can occur without this correction at later times in the sequence when the vertical bias field must be altered to decrease the magnetic trapping frequency on the BEC.

In our current set-up, the vertical bias coil is ramped up to a near maximum value to set the atom trapping location at an acceptable window in relation to the science cell defects. Additionally, the East-West and North-South bias coils are necessary for placement of the cloud to remain in focus of the imaging system and near the center of the camera, respectively. After the completion of the RF-evaporation in the quadrupole trap, the 1064-nm optical dipole trap is ramped on near the center of the magnetic quadrupole trap. To complete the transfer of the atoms, the vertical bias coil is ramped off which removes the atoms that were too hot to be trapped by the optical potential and also reduces the magnetically dominated trapping frequency. To reduce unwanted atomic slosh and keep the atoms on the camera and in focus, the bias transverse bias coils also needed to be altered during this step to account for the imperfect alignment of the vertical bias coil.

However, because it was desirable to attain the smallest trapping frequencies possible for the purpose of imaging *in situ* vortices and solitons, the magnetic quadrupole field center needed to be further distanced from the atomic sample. To accomplish this a computer-controlled electronic circuit was built to flip the direction of the current being sent through the vertical bias magnet which would allow the bias field to be ramped in either direction. This set-up could then achieve vertical magnetic bias fields of about 13 G which resulted in magnetically dominated trapping frequencies as small as 2.8 Hz in the North-South direction.

Logic	Switch A	Switch B
0	Off	On
1	On	Off

Table 6.1: Truth table for ADG436 Dual SPDT Switch used for current-flipping electronic circuit in bias magnetic coil systems.

As expected, this increased range of attainable the vertical bias fields required an additional current direction flip electronic circuit to be built for the North-South magnetic bias circuit. The East-West bias field did not require a third circuit for the evaporation and trapping schemes used since building the first such circuit.

The circuit was built using the ADG436 Dual SPDT Switch. The switch circuit functions as described in Table 6.1. A single TTL input either sets the switch in its A or B position. By flipping the leads of the magnetic bias coil for the SA and SB leads which are each in series with the magnetic coil, the leads can be set such that the S1A is connected to the “-” lead and S2A is connected to the “+” lead from the power supply. Oppositely, the S1B and S2B leads are respectively connected to the “+” and “-” power supply outputs. The result is a TTL-controlled switch that flips the current direction of the bias coil. A schematic of the current direction flip circuit can be found in Figure 6.2.

**IMPORTANT OPERATIONAL WARNING:** Because these switches are physical switches, they are quite slow compared to other switches in the system. To use them without causing unwanted current spikes, damaging the power supplies, or triggering the power supplies into a fault condition, the output current should always be zero before a direction switch is applied. We have found that a buffer time of about 10 ms of a 0 G output before and after the TTL direction flip signal is useful for avoiding fault conditions with the power supply.

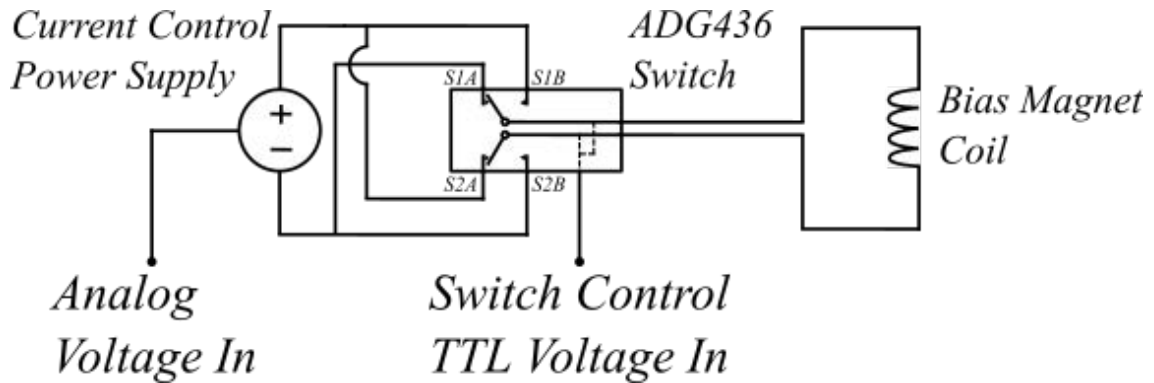


Figure 6.2: Circuit diagram of the bias coil circuit with the ADG436 switch to control current direction through the magnetic coil

## 6.2 Reconfiguration of analog computer output source power

The BEC apparatus in BEC Lab II is controlled through a timing sequence software on the main lab computer. To do this, the computer acts as a server to which two National Instrument DAQ cards connect. These NI cards supply the 32 analog and 32 digital controllers required to control the many parameters needed to create a BEC and run an experiment on it. To power these analog and digital outputs, a home-built power supply had been built with both  $\pm 5$  V and  $\pm 15$  V outputs.

As more hardware was added to the apparatus, the experiment demanded the usage of more of the analog and digital outputs for the additional instruments. While the experiment never stopped working entirely, it became evident that the power output in the 1064-nm beam was not consistent through an experimental run at each time step on the timing software program even if the program had set the power at a consistent output voltage via the power stabilization circuit. Debugging the power stabilization circuit showed no signs of the problem.

Eventually, a test was run to find if the output analog voltage matched the value set in the timing software. An analog output was monitored and compared to its set



Figure 6.3: Home-built  $\pm 15$  V and  $\pm 5$  V power supply relegated to low current uses only.

value for several time steps. We found that the analog output voltage was drooping. By changing the power supply of the analog output voltages from the homemade power supply to a commercial power supply, the output analog voltage no longer varied step-to-step and was closer to the set computer voltage.

It was determined that the additional equipment on the experiment had begun to demand more current than the home-built power supply could provide. Now, the home-built power supply seen in Figure 6.3 is only used to power a handful of electronics and some offline equipment which we know do not demand much current. Two different DC power supplies set to  $\pm 15$  V work together to power the 32 analog output board.

**IMPORTANT SHUT DOWN PROCEDURE:** The power supplies powering the analog output voltage board are pictured in Figure 6.4 and should generally be left on unless the experiment is to be entirely shut off for long periods of time. In that case, these two power supplies should not be shut off until after the timing computer



Figure 6.4: Commercial DC power supplies providing the  $\pm 15$  V needed to power the 32 channel analog voltage output board from the computer. These power supplies output the necessary current to keep the computer output control voltages from drooping throughout an experimental run.

and NI chassis are already power down.

## Chapter 7

### Conclusion

In this dissertation I have shared the results of a number of experiments recently performed in BEC Lab II, several of which have been direct extensions of the work of past students of the BEC Labs I and II. Experiments such as the BEC merging soliton study have documented the decay dynamics of an array of solitons in a BEC to compliment further numerical studies probing the instability of such soliton arrays. Additionally, having demonstrated the effectiveness of the vortex comb, this new vortex sweeping procedure is expected to have long lasting implications for creating vortex-free BECs required for future quantum turbulence studies to be conducted in BEC Lab II.

Beyond these two experiments, the various preliminary experiments and new technical procedures described in this dissertation will aid future researchers working in BEC Lab II. Future investigations such as the rigorous demonstration of observing vortex formation and annihilation at the BKT transition or the low interaction injection of the vortex clusters or dipoles into a BEC remain incomplete. In addition new proposed experiments such as the Snell's Law for vortices in a BEC experiment might be of significant interest to future research endeavors. In each of these studies, the realization of multi-shot *in situ* imaging of a BEC will be vital to attaining a full description of the system dynamics. However, regardless of the future directions of BEC lab II, the apparatus has shown the capability of conducting high-quality quantum turbulence experiments in a flexible test bed suitable for a variety of promising future experiments.



## Bibliography

- [1] S. N. Bose, “Plancks Gesetz und Lichtquantenhypothese,” *Zeitschrift für Physik*, vol. 26, pp. 178–181, 1924.
- [2] A. Einstein, “Quantum Theory of the Monatomic Ideal Gas,” *Sitzungsberichte der Preussischen Akademie der Wissenschaften, Physikalisch-mathematische Klasse*, pp. 261–267, 1925.
- [3] M. H. Anderson, J. R. Ensher, M. R. Matthews, C. E. Wieman, and E. A. Cornell, “Observation of Bose-Einstein condensation in a dilute atomic vapor,” *Science*, vol. 269, no. 5221, pp. 198–201, 1995.
- [4] J. F. Allen and A. Misener, “Flow of liquid helium II,” *Nature*, vol. 141, no. 3558, pp. 75–75, 1938.
- [5] C. J. Pethick and H. Smith, *Bose–Einstein condensation in dilute gases*. Cambridge University Press, 2008.
- [6] L. Onsager, “Statistical hydrodynamics,” *Il Nuovo Cimento*, vol. 6, Supplement 2, p. 279, Mar 1949.
- [7] D. R. Scherer, C. N. Weiler, T. W. Neely, and B. P. Anderson, “Vortex formation by merging of multiple trapped Bose–Einstein condensates,” *Phys. Rev. Lett.*, vol. 98, no. 11, p. 110402, 2007.
- [8] C. N. Weiler, T. W. Neely, D. R. Scherer, A. S. Bradley, M. J. Davis, and B. P. Anderson, “Spontaneous vortices in the formation of Bose–Einstein condensates,” *Nature*, vol. 455, no. 7215, pp. 948–951, 2008.

- [9] T. W. Kibble, “Topology of cosmic domains and strings,” *J. Phys. A: Math. Gen.*, vol. 9, no. 8, p. 1387, 1976.
- [10] W. H. Zurek, “Cosmological experiments in superfluid helium?,” *Nature*, vol. 317, no. 6037, pp. 505–508, 1985.
- [11] T. W. Neely, E. C. Samson, A. S. Bradley, M. J. Davis, and B. P. Anderson, “Observation of vortex dipoles in an oblate Bose–Einstein condensate,” *Phys. Rev. Lett.*, vol. 104, p. 160401, Apr 2010.
- [12] E. C. C. Samson, *Generating and manipulating quantized vortices in highly oblate Bose–Einstein condensates*. PhD thesis, The University of Arizona, 2012.
- [13] K. E. Wilson, *Developing a toolkit for experimental studies of two-dimensional quantum turbulence in Bose–Einstein condensates*. PhD thesis, The University of Arizona, 2015.
- [14] K. E. Wilson, Z. L. Newman, J. D. Lowney, and B. P. Anderson, “In situ imaging of vortices in Bose–Einstein condensates,” *Phys. Rev. A*, vol. 91, no. 2, p. 023621, 2015.
- [15] J. D. Lowney, *Manipulating and Probing Angular Momentum and Quantized Circulation in Optical Fields and Matter Waves*. PhD thesis, The University of Arizona, 2016.
- [16] Z. L. Newman, *A new apparatus for studies of quantized vortex dynamics in dilute-gas Bose–Einstein condensates*. PhD thesis, The University of Arizona, 2016.
- [17] J. A. Myers, *Hybrid Optical-Magnetic Traps for Studies of 2D Quantum Turbulence in Bose–Einstein Condensates*. PhD thesis, The University of Arizona, 2017.

- [18] S. Nerenberg, *Methods of Generation and Detection of Vorticity in Atomic Bose–Einstein Condensates*. PhD thesis, The University of Arizona, 2020.
- [19] G. Swartzlander Jr. and C. Law, “Optical vortex solitons observed in Kerr nonlinear media,” *Phys. Rev. Lett.*, vol. 69, no. 17, p. 2503, 1992.
- [20] D. Frantzeskakis, “Dark solitons in atomic Bose–Einstein condensates: from theory to experiments,” *J. Phys. A: Math. Theor.*, vol. 43, no. 21, p. 213001, 2010.
- [21] P. Kevrekidis, W. Wang, G. Theocharis, D. Frantzeskakis, R. Carretero-González, and B. Anderson, “Dynamics of interacting dark soliton stripes,” *Phys. Rev. A*, vol. 100, no. 3, p. 033607, 2019.
- [22] T. Kusumura, M. Tsubota, and H. Takeuchi, “Formation of quantum turbulence from dark solitons in atomic Bose–Einstein condensates,” in *J. Phys. Conf. Ser.*, vol. 400, p. 012038, IOP Publishing, 2012.
- [23] G. Theocharis, D. Frantzeskakis, P. Kevrekidis, B. A. Malomed, and Y. S. Kivshar, “Ring dark solitons and vortex necklaces in Bose–Einstein condensates,” *Phys. Rev. Lett.*, vol. 90, no. 12, p. 120403, 2003.
- [24] G.-B. Jo, J.-H. Choi, C. A. Christensen, Y.-R. Lee, T. Pasquini, W. Ketterle, and D. E. Pritchard, “Matter-wave interferometry with phase fluctuating Bose–Einstein condensates,” *Phys. Rev. Lett.*, vol. 99, no. 24, p. 240406, 2007.
- [25] W. J. Kwon, S. W. Seo, and Y.-i. Shin, “Periodic shedding of vortex dipoles from a moving penetrable obstacle in a Bose–Einstein condensate,” *Phys. Rev. A*, vol. 92, no. 3, p. 033613, 2015.
- [26] M. M. Cawte, X. Yu, B. P. Anderson, and A. S. Bradley, “Snell’s law for a vortex dipole in a Bose–Einstein condensate,” *SciPost Phys.*, vol. 6, p. 32, 2019.

- [27] P. Haljan, B. P. Anderson, I. Coddington, and E. A. Cornell, “Use of surface-wave spectroscopy to characterize tilt modes of a vortex in a Bose–Einstein condensate,” *Phys. Rev. Lett.*, vol. 86, no. 14, p. 2922, 2001.
- [28] S. Prabhakar, R. Singh, S. Gautam, and D. Angom, “Annihilation of vortex dipoles in an oblate Bose–Einstein condensate,” *J. Phys. B: At. Mol. Opt. Phys.*, vol. 46, no. 12, p. 125302, 2013.
- [29] S. Rooney, T. Neely, B. P. Anderson, and A. Bradley, “Persistent-current formation in a high-temperature Bose–Einstein condensate: An experimental test for classical-field theory,” *Phys. Rev. A*, vol. 88, no. 6, p. 063620, 2013.
- [30] I. S. Veshchunov, W. Magrini, S. Mironov, A. Godin, J.-B. Trebbia, A. I. Buzdin, P. Tamarat, and B. Lounis, “Optical manipulation of single flux quanta,” *Nature Communications*, vol. 7, no. 1, pp. 1–7, 2016.
- [31] Z. Hadzibabic, P. Krüger, M. Cheneau, B. Battelier, and J. Dalibard, “Berezinskii–Kosterlitz–Thouless crossover in a trapped atomic gas,” *Nature*, vol. 441, no. 7097, pp. 1118–1121, 2006.
- [32] M. O. Borgh and J. Ruostekoski, “Topological interface engineering and defect crossing in ultracold atomic gases,” *Phys. Rev. Lett.*, vol. 109, p. 015302, Jul 2012.
- [33] T. Ollikainen, A. Blinova, M. Möttönen, and D. S. Hall, “Decay of a quantum knot,” *Phys. Rev. Lett.*, vol. 123, p. 163003, Oct 2019.
- [34] P. Kuopanportti, B. P. Anderson, and M. Möttönen, “Vortex pump for Bose–Einstein condensates utilizing a time-averaged orbiting potential trap,” *Phys. Rev. A*, vol. 87, no. 3, p. 033623, 2013.

- [35] T. P. Simula and P. Blakie, “Thermal activation of vortex-antivortex pairs in quasi-two-dimensional Bose–Einstein condensates,” *Phys. Rev. Lett.*, vol. 96, no. 2, p. 020404, 2006.
- [36] J.-y. Choi, S. W. Seo, and Y.-i. Shin, “Observation of thermally activated vortex pairs in a quasi-2d Bose gas,” *Phys. Rev. Lett.*, vol. 110, no. 17, p. 175302, 2013.
- [37] R. Desbuquois, L. Chomaz, T. Yefsah, J. Léonard, J. Beugnon, C. Weitenberg, and J. Dalibard, “Superfluid behaviour of a two-dimensional Bose gas,” *Nature Physics*, vol. 8, no. 9, pp. 645–648, 2012.